UNIVERSITÉ DE NEUCHÂTEL — INSTITUT DE GÉOLOGIE

FACULTÉ DES SCIENCES — CENTRE D'HYDROGÉOLOGIE

Modeling tracer and particle transport in karst conduit structures

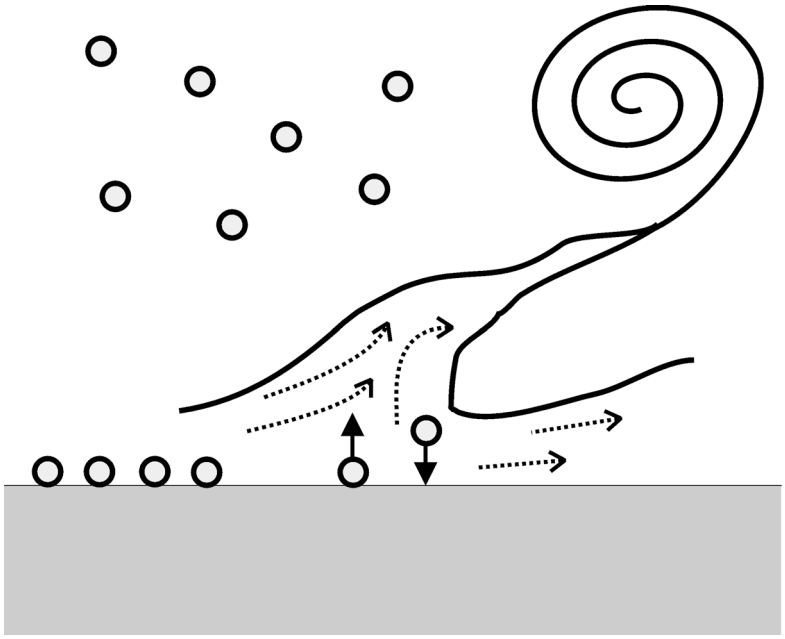

Michael Hauns

Thèse de doctorat soutenue le 31 Mars 1999 devant le jury suivant:

Prof. François Zwahlen	Université de Neuchâtel (Suisse)	Directeur
Prof. Olivier Atteia	Université de Bordeaux (France)	Codirecteur
Dr. Felix Hermann	ETH Zürich (Suisse)	Expert
Prof. William B. White	Pennsylvania State University (USA)	Expert
Prof. Pierre Perrochet	Université de Neuchâtel (Suisse)	Expert

IMPRIMATUR POUR LA THESE

Modeling tracer and particle transport under turbulent flow conditions in karst conduit structures

de M. Michael Claudius Hauns

UNIVERSITE DE NEUCHATEL

FACULTE DES SCIENCES

La Faculté des sciences de l'Université de Neuchâtel sur le rapport des membres du jury,

MM. F. Zwahlen (directeur de thèse), P. Perrochet, O. Atteia (Bordeaux F), F. Hermann (ETH Zürich) et W.B. White (Pennsylvania State Uni. USA)

autorise l'impression de la présente thèse.

Neuchâtel, le 23 novembre 2000

Le doyen:

J.-P. Derendinger

Contents

Abstract

Karst groundwater protection is an important issue in many regions in Switzerland and elsewhere. Karst aquifers expose a duality of low-permeability matrix flow and high-permeability fissures and conduits. Hydrodynamics in karst conduits, representing a high conductivity network, influences both the breakthrough curves of tracer tests and the transport of particles.

Micro tracings in underground rivers show an important tailing in the falling limb of the breakthrough curve. This led to the conclusion that a linear (Darcian) flow model is not adequate to describe hydrodynamics in a karst conduit network. In the present thesis hydrodynamics in a karst conduit is described by solution of the Navier-Stokes equations with the k-ε turbulence closure and the finite volume method.

In order to apply this approach, a detailed conceptual model of karst conduits is required. On this purpose, field investigations were undertaken in Milandre cave, Switzerland. Hydrodynamics in a karst conduit is a torrential drop-pool sequence rather than continous channel flow. Conduit geometry may be classified into some basic types. For the processes we are interested in, larger volumes of stagnant water, e.g. in a pool or conduit enlargement are the most important type of conduit form.

A Computational Fluid Dynamics (CFD) model is used to calculate flow in example-types of Karst conduit geometries on a decametric scale. Generally it works in 3D, and it can handle free surfaces with a multiphase approach. This is necessary for simulation of supercritical flow. When the surface is flat and a priori known (subcritical or tranquil flow), a rigid lid approximation is used. This brings the advantage that the scalar transport equation for the dye tracer may be solved on a static velocity field in less CPU time. With the available computing equipment, the resolution is such that the large eddies are resolved, while the vortex street between eddy and main flow is not resolved. The versatility of the visualisation platform ZoomIn, currently in development at the informatics department of Neuchatel University, allowed us to depict the complex flow patterns in the studied structures.

A new BTC fitting and interpretation method is developed. It is based on an analytical solution of the transport equation and allows the quantification of the tailing.

A scaled laboratory model of a pool was built to perform micro-tracing tests under well-defined conditions. It confirms the field observation that retarding in a micro tracing experiment is closely related to the presence of pools. Comparison to the numerical results reveals some differences which may be due to the limited resolution of turbulent phenomena mentioned above.

A transfer function approach may be used to extend the results of local scale tracer tests to mesoscale structures. Transfer functions from a single structure are concatenated. This allows to synthesize breakthrough curves of geometries that are too large for a single numerical simulation, to couple different structures and to see the shape of a breakthrough curve far away from a pool.

Sedimentation of small particles is calculated with a bottom shear stress approach. The sedimentation rate of particles of a given size passing a pool depends on the distribution of the critical bottom shear stress. The shear stress distribution can be derived from the numerical model.

Both comparison of tracer transport and particle deposition model to field experiments show encouraging results.

Résumé

La protection des eaux souterraines dans le Karst est un sujet important en Suisse et ailleurs. Les aquifères karstiques montrent une dualité entre les écoulements dans les blocs à faible perméabilité, et les écoulements dans des fissures et conduits à forte perméabilité.

Des micro-traçages en rivière souterraine ont démontré un retard important sur la partie descendante des courbes de restitution. Ceci amène à la conclusion que des modèles d'écoulements linéaires (type Darcy) ne sont pas appropriés pour décrire les conditions hydrodynamiques dans un réseau karstique.

Ainsi, dans cette thèse, l'hydrodynamique d'un conduit karstique est décrite sur la base des équations de Navier-Stokes. Le modèle de turbulence k-ε et une discrétisation en volumes finis sont utilisés.

Cette approche nécessite un modèle conceptuel détaillé du réseau karstique. Des études de terrain dans la grotte de Milandre (Ajoie, Suisse) ont été réalisées. Il ressort que les conditions d'écoulement dans les conduits karstiques sont de type torrentiel (cascade-bassin) plutôt que de type écoulement laminaire. Les géométries peuvent être classées en quelques exemple-types, en fonction de leur comportement hydraulique.

Les formes avec un volume d'eau stagnante important sont d'un intérêt majeur pour les processus physiques examinés ici.

Un modèle numérique de dynamique des fluides est utilisé pour calculer l'écoulement dans les exemple-types de conduits karstiques sur une échelle décamétrique. C'est une approche 3D capable de traiter des surfaces libres grâce a un modèle multiphase. Ceci est nécessaire pour la simulation des écoulements supercritiques. Quand la surface de l'eau est plate et connue a priori, un modèle « rigid lid » est utilisé, avec l'avantage de pouvoir simuler le transport des traceurs sur un champ d'écoulement constant, cela représentant un gain de temps substantiel. Avec la résolution spatiale qui a pu être réalisée dans cette étude, les grands et petits contre-courants sont visibles, mais pas les tourbillons entre les contre-courants et l'écoulement principal.

Le système de visualisation ZoomIn, qui a été mis au point par l'Institut d'Informatique de l'Université de Neuchâtel, permet la visualisation des écoulements complexes.

Basé sur une solution analytique de l'équation d'advection-diffusion, une nouvelle méthode d'ajustage des courbes de restitution, qui permet de quantifier le retard, a été développée.

Un modèle de laboratoire à l'échelle 1:5 représentant un bassin de conduit karstique a été construit afin de faire des essais de tracage. La relation entre la présence d'eau stagnante et le retard observé au niveau des courbes de restitution a pu être confirmée. Des différences par rapport au modèle numérique subsistent, dues à la résolution limitée des phénomènes de turbulence.

La concaténation des fonctions de transfert permet l'extrapolation des résultats obtenus à l'échelle décamétrique sur une mésoéchelle de quelques centaines de mètres.

La sédimentation des petites particules est calculée en utilisant le cisaillement au fond. Le taux de sédimentation dans un bassin dépend de la distribution spatiale du cisaillement qui peut être calculé avec le modèle d'écoulement numérique.

La comparaison des résultats du modèle numérique avec les essais de terrain montre des résultats encourageants autant pour le transport de traceurs que pour la sédimentation des particules.

Zusammenfassung

Der Schutz der Grundwasservorkommen in Karstgebieten ist ein wichtiges Thema in vielen Regionen der Schweiz und in anderen Ländern. Karstaquifere haben Grundwasserfluss einerseits in der wenig durchlässigen Gesteinsmatrix, andererseits in hochdurchlässigen Klüften und Höhlen. Der Abfluss in diesem hochdurchlässigen Leitungsnetz beeinflusst sowohl die Durchgangskurven von Experimenten mit löslichen Tracern als auch das Sedimentationsverhalten suspendierter Partikel.

Kleinskalige Tracerversuche in Höhlenflüssen zeigen ein merkliches Tailing im abfallenden Ast der Durchgangskurve. Dies führt zu der Feststellung, dass ein lineares Darcy-Modell nicht geeignet ist zur Beschreibung der Fließprozesse in einem Karstkluftnetzwerk. In der vorliegenden Arbeit werden diese Fließprozesse mit Hilfe der Navier-Stokes-Gleichungen, des k-ε Turbulenzmodells und der Methode der finiten Volumen beschrieben.

Um diesen Ansatz anwenden zu können, wird ein detailliertes konzeptionelles Modell für Karstkluftnetzwerke benötigt. Zu diesem Zweck wurde die Höhle von Milandre (Ajoie, Schweiz) näher untersucht. Die Gerinneform von Höhlenflüssen ist charakterisiert durch einen Wechsel von schiessendem und strömendem Abfluss (drop-pool oder riffle-pool sequence). Die auftretenden Gerinnegeometrien können durch einige Grundtypen (example-types) beschrieben werden. Für die physikalischen Prozesse, die hier untersucht werden, sind Geometrien mit hohem Anteil an stehendem Wasser am interessantesten.

Die Strömung in den Gerinneform-Grundtypen wird mittels eines numerischen Strömungsmodells (CFD-Modell) berechnet. Die Länge der berechneten Geometrien liegt im Meter- bis Dekameterbereich. Das Strömungsmodell ist dreidimensional. Freie Oberflächen und schiessender Abfluss können mittels eines Zweiphasenansatzes für Wasser und Luft berechnet werden. Bei ebener Wasseroberfläche mit a priori bekannter Position, wie sie bei strömendem Abfluss und Geometriegröße im Meterbereich vorliegt, wird die „rigid-lid"-Näherung angewandt. Dies erlaubt die Berechnung des Tracerdurchgangs auf einem zeitlich konstanten Geschwindigkeitsfeld und somit eine große Ersparnis an Rechenaufwand. Mit der erreichten räumlichen Diskretisierung werden Kehrströmungen verschiedener Größe aufgelöst, nicht jedoch die Wirbelstraße zwischen Kehrwasser und Hauptströmung. Die Visualisierungsplattform ZoomIn, die am Institut für Informatik der Universität Neuchâtel entwickelt wurde, erlaubt die graphische Darstellung komplexer Strömungsmuster.

Eine neue Methode zur Anpassung und Interpretation der Tracerdurchgangskurven wurde entwickelt. Diese Methode geht von einer analytischen Lösung der Transportgleichung aus und erlaubt die Quantifizierung des Tailings.

Um Tracerversuche im Gerinne unter Laborbedingungen durchführen zu können, wurde ein Labormodell (durchströmtes Bassin) gebaut. Die durchgeführten Versuche bestätigen die Hypothese, dass das beobachtete Tailing durch Kehrströmungen hervorgerufen wird. Der Vergleich des Labormodells mit dem numerischen Strömungsmodell zeigt einige Unterschiede bei der Form der Tracerwolke, die vermutlich auf die beschränkte Auflösung des Turbulenzmodells zurückzuführen sind.

Mit Hilfe von Transferfunktionen können die Ergebnisse des numerischen Modells zu mesoskaligen Szenarios extrapoliert werden.

Die Sedimentation suspendierter Partikel wird mittels der Scherkräfte am Grund berechnet. Die Sedimentationsraten in einem Becken hängen von der räumlichen Verteilung der Scherkräfte ab, welche im numerischen Strömungsmodell berechnet sind.

Der Vergleich zwischen numerischer Modellierung und Experiment zeigt sowohl für den Tracertransport als auch für die Sedimentation suspendierter Partikel ermutigende Ergebnisse.

The sinkhole of Bied brook in 'La vallee des ponts', colloid transport study area
(Photography by Cyril Delporte)

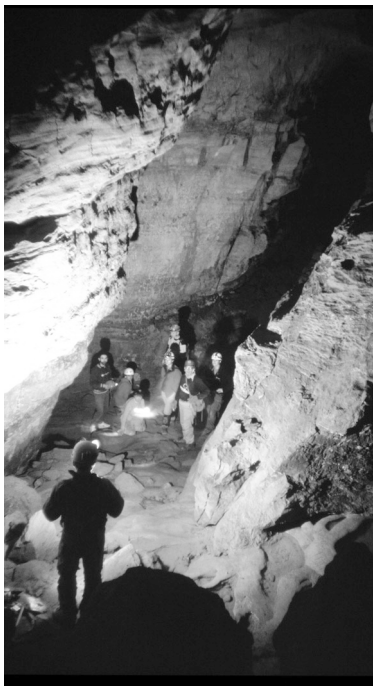

Example of a dry underground-river bed in Butler cave, West-Virginia

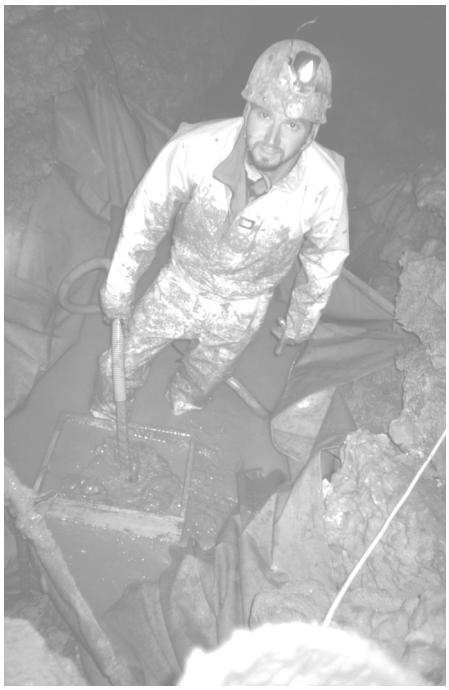

Sediment injection by the author in Milandre cave, Switzerland

1 Introduction

About 20% of the earth's land surface is occupied by karst terrains (GVOZDETSKII 1967). Water supply has been a critical issue in karst since historical times, and increasing urbanization of karst regions will render it even more severe.

In contrast to porous media hydrology, where the underlying equations have been well-studied for a long time, there is no applicable theoretical framework yet for karst. Karst aquifers are characterized by the duality of a fast-transport conduit network, mostly originating from fissure widening by limestone dissolution, and a low permeability rock matrix. Recharge by sinkholes, sinking streams and epikarst soil covers tends to be concentrated, and therefore karst aquifers are not well-protected against accidental spills and permanent contamination (ZWAHLEN 1994, MEIMAN 1991). Small particles may act as contaminant carriers and transport organic (NAPL) and radioactive pollution much more efficiently than pure water would do (MCCARTHY 1989). Transport of colloids in aquifers is mainly limited by deposition (RYAN 1996). Accumulation of small particles also leads to clogging of karst networks. Unclogging by exceptional storms may change the hydraulic characteristics dramatically (LASTENET 1995).

The tracing experiment is one of the most frequent investigation tools in karst hydrogeology. It was used traditionally to study the connection between sinkhole and resurgence in karst basins (MANGIN 1976). Recently there is an increasing use of tracer tests for quantitative characterization of aquifers, i.e. hydraulic properties and predictive scenarios of accidental contaminant spill into an aquifer. Karst aquifers include by definition a network of channels, also called conduits, which range from cm to m in diameter inducing specific hydraulic and transport properties. The most striking feature is the existence of very fast transport passways. In this context, tracer experiments in karst regions are mostly used to determine the catchment basin of a spring and to roughly estimate the position and characteristics of the conduit network. Numerous tracer tests showed dispersion and tailing effects. This is even the case when tracers are transported in conduits that are known to have a simple geometry. By contrast to porous media these characteristics of the breakthrough curves are mostly unexplored or misinterpreted presumably because of the lack of a sound theoretical basis.

1.1 Objectives

The objective of this work is to improve understanding of the physical transport processes of tracers and particles, starting with a deterministic approach on a local scale.

A twofold modeling approach, including numerical and experimental modeling, is applied. This allows to do tests that are not possible in the field in this form. The next step is then extrapolation of these local results to field scale.This leads to the following work plan:

1 Outline of a conceptual model of karst hydrology, with a focus on conduit flow. To achieve this, characteristics of conduit flow will have to be analyzed and classified into specimen. This shall be called a flowform (e.g. tranquil channel flow, pool, hydraulic jump).

1 Implementation of a suitable computational fluid dynamics (CFD) program that allows numerical modeling of these flowforms, and tracer and particle transport therein, with a sufficient precision to study the above described processes, i.e. tracer and particle transport.

- Construction of a scaled laboratory model for transport experiments on a local scale.
- Development of a suitable formalism to describe the shape of tracer breakthrough curves, the dispersion and to quantify the tailing effect.
- Development of a sedimentation-resuspension model for fine particle transport. It has been shown that sedimentation and resuspension are the two important processes where the flowform will influence particle transport, while it has little influence on aggregation processes (ATTEIA 1998).
- Extrapolation from the results on local scale flowforms to the scale of a conduit or a conduit network.

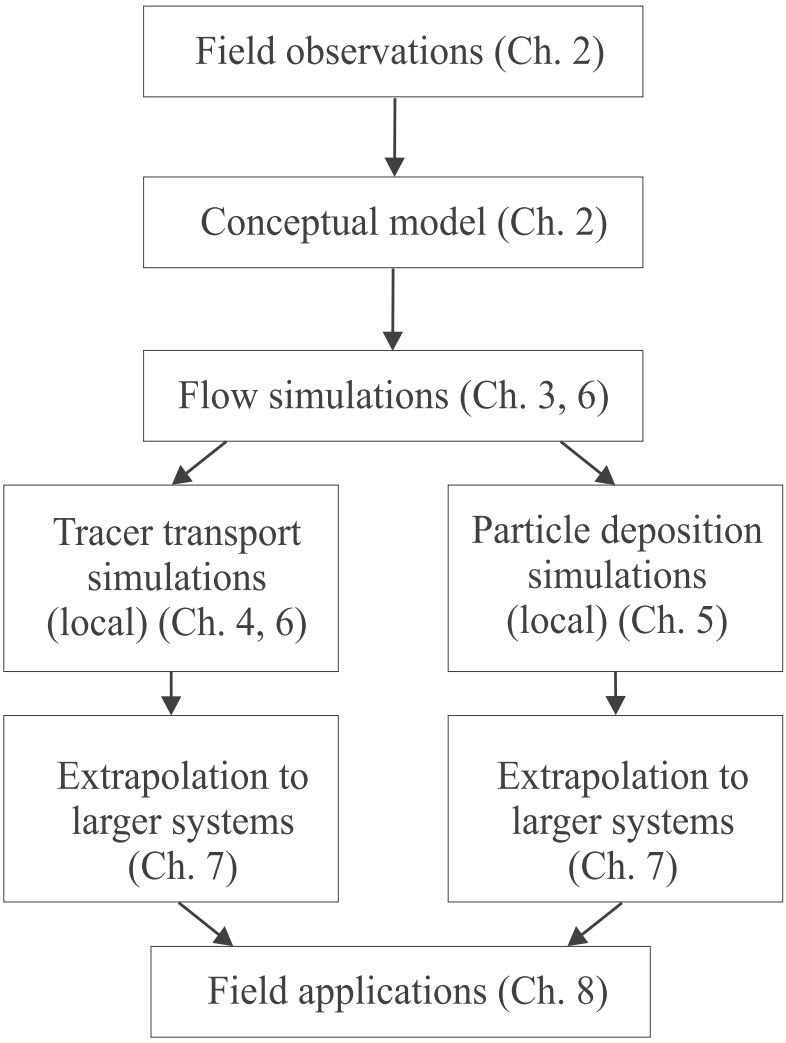

Fig. 1.1 Work plan: the numerical model is based on the flowform analysis – tracer and particle transport are developed from its results

1.2 Geographical context and fieldwork: Colloids and particles in the Noiraigue aquifer

The PACT (physico-chemical aspects of colloidal transport) project has studied details of particulate transport in the Noiraigue aquifer in northwestern Switzerland. Atteia & Kozel (1997) give an extensive description of the test site which shall be summarized here. The studied region is the 60 km^2 „Vallee des Ponts“ area located in the Swiss Jura mountains at an altitude ranging from 1000 to 1300 meters a.m.s.l. (Fig. 1.2). This region receives an average of 1500 mm rainfall yearly. The geological features of the aquifer consist of 500 m thick karstified SW-NE upper jurassic and lower cretaceous limestone syncline bordered by two anticlines, presenting a fault contact with the central valley. The Noiraigue spring is the only outlet of this karstic aquifer and lies at 750 m, flowing at the outcrop of a regional fault. Fine molasse sandstone covers the limestone in the center of the valley over a maximum thickness of 300 m. These tertiary sediments of low permeability are overlaid by thin glacial till and post-glacial marly deposits. Finally, during the last 6000 years peat was formed on these low permeability deposits, covering 20 km^2. The Bied brook, draining the remaining peat areas and the agricultural soils of the valley, ends in a karstic sinkhole situated in the cretaceous rocks. The straight line distance between the Bied brook and the Noiraigue spring is approximately 4 km. Tracer tests showed that the travel time between this main sinkhole and the spring varies from 3 to 14 days according to flow conditions. The other two-thirds of the catchment basin are composed of limestone anticlines covered by thin organic- and Ca-rich soils. The average travel time from these areas to the spring is similar to the travel time from the Bied sinkhole to spring. The karstic network is well developed and presents only one outlet for 60 km^2. This site is particularly suited for colloidal particles studies because the peat and marly quaternary deposit areas deliver significant amounts of colloidal organic matter and clays to the Bied brook. The site is equipped for continuous measurements of waterlevel, temperature, electric conductivity, turbidity, and rainfall on the Bied brook and at the Noiraigue spring. Samples were taken almost weekly for chemical and particle analysis from 1994 to 1998.

1.3 Karst conduit network modeling approach

While flow in porous media is laminar and can be successfully described by linear potential-gradient equations, flow in conduits is mainly in the turbulent regime (Atkinson 1977, Gale 1984, White 1970).

To date, numerical modeling of karst conduits has been mainly done with double-porosity models (Kiraly 1988, Teutsch 1988, Sauter 1992) or with pipe flow models (Jeannin 1996). Both are not able to describe all processes adequately. Therefore a non-linear mathematical approach, i.e. solution of the Navier-Stokes equations with an appropriate turbulence closure should help to understand these processes better. From a number of existing computational fluid dynamics (CFD) software packages, we choose CFX-F3D from AEA Technology. CFX was developed for mechanical and nuclear engineering purposes, but it was also utilized for several environmental applications like fluvial hydraulics (Horat 1996), powder avalanche kinetics (Hermann 1990) and sediment transport (Schleiss 1998). CFX uses the finite volume method on block-structured grids and the k-ε turbulence closure. This approach is useful and

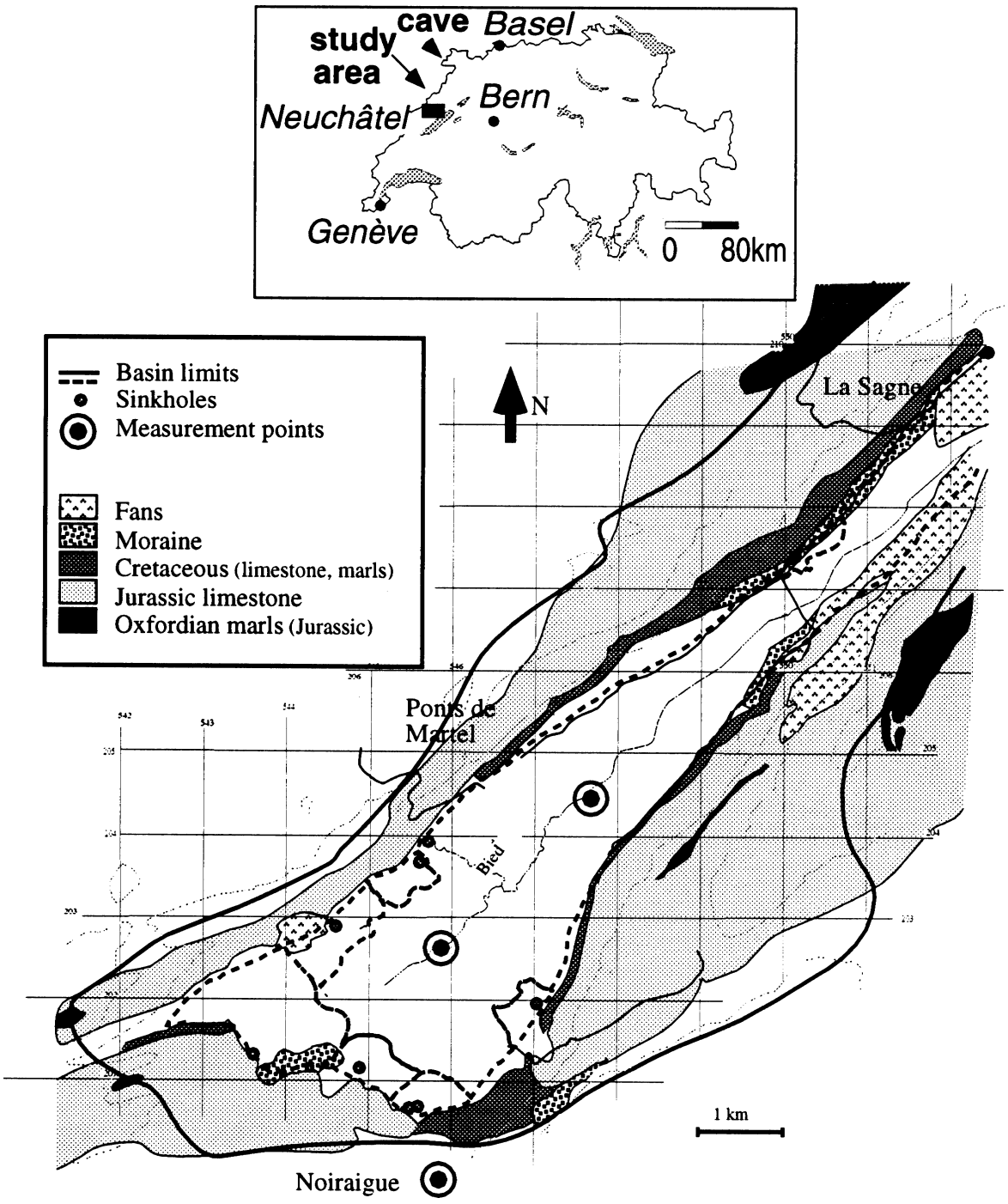

Fig. 1.2 **The Noiraigue aquifer: geographical location and geology** (ATTEIA & KOZEL 1997)

appropriate to model flows on a local, i.e. metric scale, with the objective to resolve local turbulence distribution, eddies and flow reversal and their influence onto tracer and particulate transport. In order to obtain modeling results for a single conduit on a kilometric scale, a transfer function approach is needed. Transfer functions of a particular geometry (channel, pool or rapid) are created by deconvolution of the response to a rectangular input pulse, as calculated by numerical modeling. Then these transfer functions from different flowforms may be put together to describe a conduit passage.

A formalism is needed to characterize the obtained breakthrough curves. A fit with a solution of the advection-diffusion equation (ADE), as used in porous media, allows to quantify dispersion and retarded mass on a tracer breakthrough curve. The simulated conduits show reasonable agreement with experimental micro-tracings in a cave stream.

Colloid and particle sedimentation

The paths of fine particles in a fluid are very complex. The settling velocity is so small that sinking becomes a negligible component of the overall motion of a particle. There is theoretical evidence that in sufficiently turbulent flow the distribution of small particles over the volume is isotropic (CHANG 1997).Therefore, particles will have random encounters with all flow boundaries. Cohesive forces between particles are as large or significantly larger than the gravitational force (BROCKMANN 1984), and particles may stick to walls and ceiling of a conduit as well as to the floor.

Attachment and detachment is expected to be controlled on a microscale by turbulent bursts (CLEAVER 1973, NINO 1996). On the macroscopic scale this is related to the averaged turbulent shear stress on the flow boundary, which can be derived from the numerical model. This allows, on a statistical basis, to predict the influence of a flowform onto the particle size distribution in groundwater.

1.4 Synopses

- Chapter 2: Description of the conceptual model, leading from cave survey data to a classification of flow forms.
- Chapter 3: Numerical and experimental modeling techniques.
- Chapter 4: Outlines of the mathematical approach to curve fitting.
- Chapter 5: Modeling approach for fine particle deposition in conduits.
- Chapter 6: Results of the flow simulations. Interpretation of the breakthrough curves from the numerical simulations are compared with the equations outlined in Chapter 4.
- Chapter 7: Mesoscale scenarios based on the transfer function approach.
- Chapter 8: Comparison the scenarios of the numerical model to field data, and ideas towards possible future applications of this approach.

2 Karst conceptual model

The objective of a conceptual model in this context is to reduce the multifaceted complexity that nature shows in karst underground landscapes, caves and conduit networks to principles that may be dealt with on the still very limited space of a CFD program on a computer. However such a model should as much as possible be consistent with current knowledge of karst geomorphology.

2.1 Karst geography and geology

WHITE (1988) gives a detailed description of karst geography and geology, from which the following is a brief summary.

The distinguishing feature of a Karst landscape is the dominance of chemical dissolution as an erosive force. The four important karst-forming rocks are limestone, dolomite, gypsum and salt. However, due to solution kinetics, karst features do not develop easily in dolomite, while salt and gypsum lead to transient landforms due to their much higher solubility. Thus limestone karst may be expected to expose the most interesting features but lead to a non-transient landscape considering a human time scale. Other geologic factors that constitute the hydrogeologic setting are the thickness of soluble rock, its stratigraphic characteristics and tectonic setting, eventually together with adjacent layers of impermeable or insoluble rock. Karst landscapes are composed by arrangement of a number of dominant landforms: Doline Karst, Cockpit Karst, Cone and Tower Karst, Fluviokarst, Pavement Karst, Polje Karst, Labyrinth Karst and Cave Karst. The bedrock may be exposed like in Ireland's burren and often in alpine karst regions or hidden under a thick soil cover, like the karstlands of the temperate United States.

2.1.1 Caves and conduits: karst underground landscape

The underground drainage system in karst develops a conduit system along paths where the limestone is more easily dissolved. Conduits range from about a centimeter in diameter, the smallest size suitable for water flow under pipe or free surface flow conditions (DREYBRODT 1988), up to more than a 100 meters when the stability of the surrounding rock allows this. However, most of the time breakdown will limit the formation of very large openings. Caves are fragments of conduits that happen to be large enough for human exploration. Taking length as a metric for cave size, the number of existing caves should grow as a power function towards smaller sizes (CURL 1986). A similar result might be found using another parameter like conduit section (JEANNIN 1996, MARECHAL 1994). Similarity of phenomena on different geometric scales is expected.

There are single-conduit, dendritic and maze caves, the latter can be subdivided into network, anastomotic and spongework pattern caves. Passages can be straight linear, angular or sinuous. Linear passages occur where a major joint or fracture controls the flow path, angular passages may occur when the hydraulic gradient is diagonal to the regional joint set. Sinuous passages are expected in flat and horizontal bedding, creating alike the meandering in surface rivers

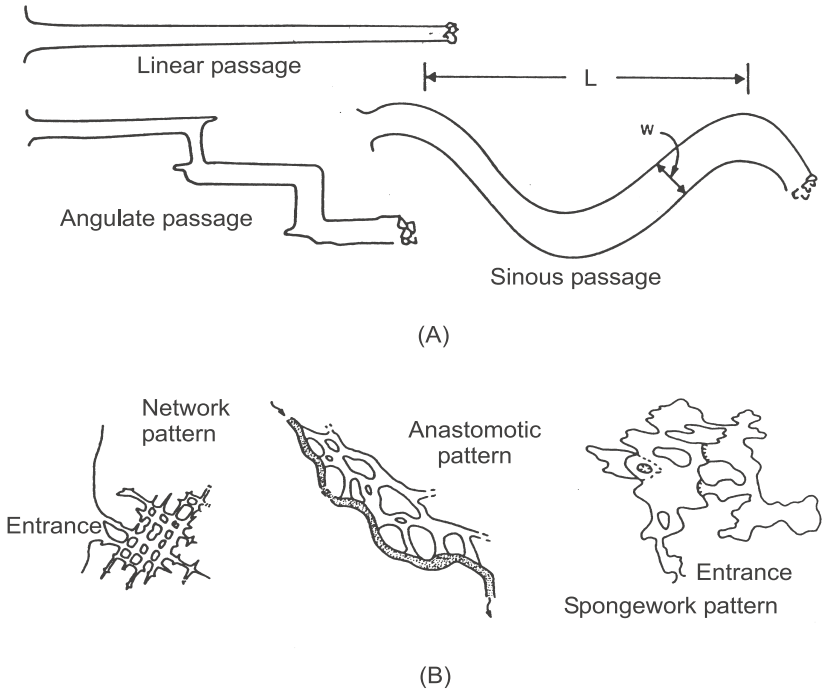

Fig. 2.1 Sketch maps of cave shapes (WHITE 1988)

(A) Sketch maps showing the ground plans of single-conduit passages with linear, angulate and sinuous patterns
(B) Sketch maps showing the ground plans of maze-type cave passages with network, anastomotic, and spongework patterns

(see Fig. 2.1). On a mapped cave, passage orientation may be represented on a rosette, e.g. in order to compare it to a geological map.

From a hydraulic point of view, linear caves may be related to one sinking stream, dendritic caves to an underground drainage system including tributary streams while maze caves, where every possible joint has developed into a passage, have a hydraulic behavior similar to a swamp. PALMER (1991) compared a large number of cave morphologies. Nearly all but the simplest caves were found to be of the branchwork or maze type, with four major subdivisions among different types of maze caves. 57% of the surveyed caves, representing 65% of the surveyed cave length, were found to be branchwork caves. Remember that in a branchwork conduit system only the main passage may be large enough for exploration, hiding much of the tributaries to the human eye. In an earlier paper PALMER (1975) reported on tendencies during cave development which may decide whether a branchwork or a maze cave will develop. High gradient caves or alpine caves occur as an alternative drainage from high-altitude catchment areas to the valleys below and tend to be composed as a sequence of vertical or nearly vertical components - shafts and chimneys - and nearly horizontal passages, thus a step-stair like profile. This is not restricted to alpine karst terrains. Many caves in moderate-relief terrain and the streams therein exhibit a similar profile, even if they may not reach the impressing shaft heights of alpine systems. Later it will be seen that the resulting

drop-pool character of the stream leads to important hydraulic properties of the latter. However, long passages of a conduit may have a very small gradient. In Mammoth cave conduit gradients were found to be as low as 10^{-7} in large canyons in the main cave level (WHITE 1989).

Multiple levels of conduit systems develop when the general water level in a region drops considerably over geological times, forcing the underground drainage system to create a new, deeper level. Examples for this are the Mammoth cave system, Kentucky, USA, and the Sieben Hengste system in central Switzerland. This provides unique opportunities to the non-diving explorer to observe a former drainage system.

Passage cross sections are of high interest to the modeling scientist. Cross sections may be formed under hydraulic control or structural control. The first tend to give smooth, streamlined circular or ellipsoidal forms while the latter produce triangular and rectangular shapes depending on the combination of bedding and joint orientation (see Fig. 2.1). A conduit under pipe-flow condition would probably maintain an elliptical form, while free-surface flow leads to downcutting towards a canyon shape. The shape of larger passages may become considerably more complicated when breakdown occurs. A place where the cave widens or heightens above the average passage dimension is called a room. For the case of a water-filled cave or conduit we call this a pool, and, as shall be seen later, pools may strongly influence the flow patterns and tracer plume passage.

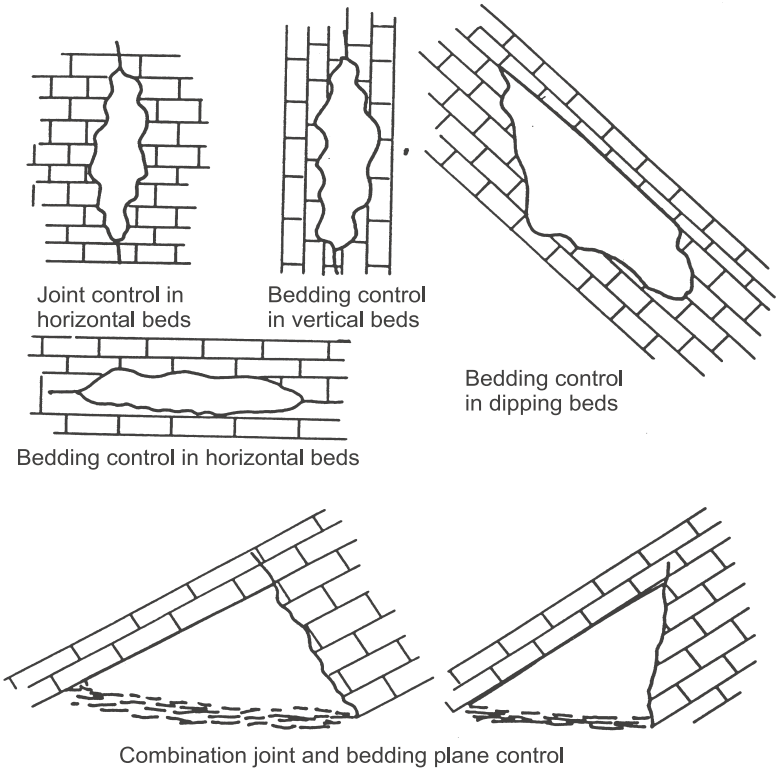

Fig. 2.2 Cross sections of passages resulting from structural control of limestone dissolution (WHITE 1988)

2.1.2 Rock surface features in solutional channels

Like the solutional features on surface exposed karst, whose description has been omitted above, solutional attack will produce a second order geometry (when considering the overall geometry of a cave as described so far of first-order). SLABE (1995) gives a comprehensive overview of these surface shapes that he calls 'rocky relief'. Ceiling channels, floor slots, incised meanders and bedding/joint plane anastomases develop during periods of reduced flow compared to the flow level that created the passage. Rills, grooves, echinoliths, flutes and scallops are sculptured into the floor, walls and ceiling of a passage filled with flowing water. Scallops are always oriented to the main flow direction, and their spacing may be utilized to calculate paleodischarge in now-dry passages. The conditions under which scallops develop have been investigated by ALLEN (1995), GOODCHILD & FORD (1971) and BLUMBERG & CURL (1974). Additional roughness may be added to the rock surface by locally more active solution due to mixing of chemically different waters and residual layers of bedrock that are less easily soluble than the surrounding material.

2.2 Hydraulic properties of conduit systems

Karst aquifers are characterized by a matrix/conduit duality. The matrix storage leads to a non-zero base flow, while during times of high recharge most of the water will pass quickly through the conduit system. ATKINSON (1977) found in Mendip Hills, Somerset, the storage capacity of the pipe system to be 30 times smaller than the capacity of the matrix, while it accounts for 60 - 80% of the quantity of transported water. BONACCI (1987) found 25% base flow and 75% quick flow for the Klokun Spring, Dalmatia. The present study is focused exclusively on conduit flow. The hydraulic coupling with the matrix is not considered.

2.2.1 Field observations in 'La Grotte de Milandre'

Milandre is a dendritic cave more than 10 kilometers long. It is located in the Jura plateaus in the front of the Jura Mountains in Northern Switzerland. The main conduit is dominating and makes it possible to follow the underground stream upstream from the spring over a distance

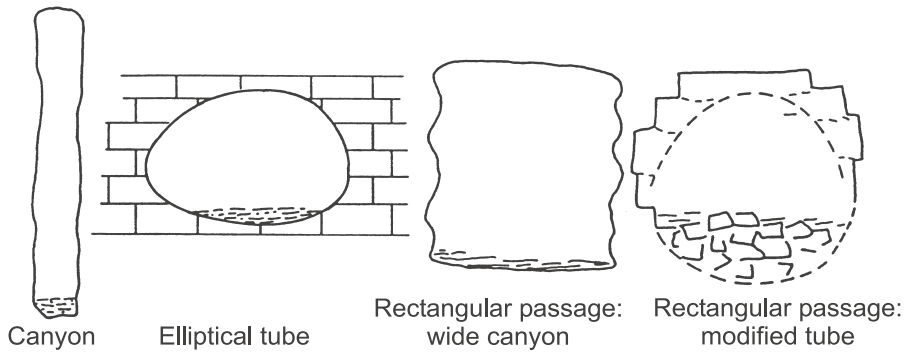

Fig. 2.3 Cross sections of passages with shapes controlled by the hydraulics of flowing water (WHITE 1988)

of about 5 kilometers (Fig. 1.2). There are 2 - 3 major confluents. Along this path, the channel geometry ranges from sections of lakes with large flow cross-sections (1 - 5 m^2), low slope and low velocity (about 0.01 m/s at low water stage) to sections of rapids and cascades. The main conduit is canyon-shaped, i.e. 5 - 10 times higher than large (comp. Fig. 2.3), with an average width of 1 - 2 m. Numerous tracing experiments on medium and short distance have been carried out along the underground path of the Milandrine stream, with injection from wells, dolines and directly into the river (JEANNIN 1996, DOERFLIGER 1996, MARECHAL 1994). Their characteristic parameters (diffusion, tailing) will later be compared to the numerical model developed here. The geomorphology of the cave has been described in great detail by MARECHAL (1994), including numerous cross-sections, classification of sections with different gradient and description of hydraulic phenomena. Exploration of Milandre is very instructive for a field study of flowforms, and the classification of flowforms in the present study (see Table 2.1) was much inspired by this.

2.3 Breakup into local basic structures

The capacity of recent computers available for the present CFD calculations lies around a grid with some 100'000 volume cells. This means that, if one wishes a resolution sufficient to show the interesting secondary flow phenomena like eddies, vortices and distribution of turbulence over a section, the conduit length that can be simulated is 1-10 m, depending on the complexity of the geometry that may require a locally refined grid. Free surface flow doubles the storage space needed because the variables of the air phase have to be stored for every volume element. This makes it necessary to break up the variety of possible passage shapes as described above into a few prototypes of flowforms. Fortunately there is evidence that single passages tend to be straight and of constant cross-section (WHITE 1989). Table 2.1 lists relevant flow forms for both free surface and pipe flow.

There are four different types of channel of interest: a regular channel with constant cross-section and flat walls and floor, a channel with ondulating walls, a more irregular channel due to solution pockets, and a channel with frequent angular bends, as it will develop when the hydraulic gradient is diagonal to the local joint set.

A pool shall be defined as a sudden expansion in cross section (horizontal and/or vertical), and a non-negligible storage of stagnant water. A particularly interesting case of this is a maze, which may also be considered as a pool with a large volume fraction taken by solid obstacles.

Potholes are a vertical profile feature described by Slabe. Flow velocities are high (0.35 - 0.5 m/s) in regions where potholes develop. However the flow regime is expected to remain subcritical. Deep potholes have also been found in Milandre cave, but generally they are a rare feature. A hydraulic jump occurs when flow is accelerated into the supercritical domain on a short stretch with higher gradient, and then meets slower or stagnant water. This requires a free surface and is therefore only defined for such a flow. A breaking wave or hydraulic jump will lead to air entrainment into the water. A vertical or near vertical drop shall be defined as a waterfall. A waterfall will usually result in even larger air entrainment and rotating flow in the downstream basin. Some waterfalls may not end into a basin, but on some rock surface, resulting in water being rejected in all directions. However, numerical modeling of this case is beyond the scope of this approach. Like a hydraulic jump, a waterfall will only

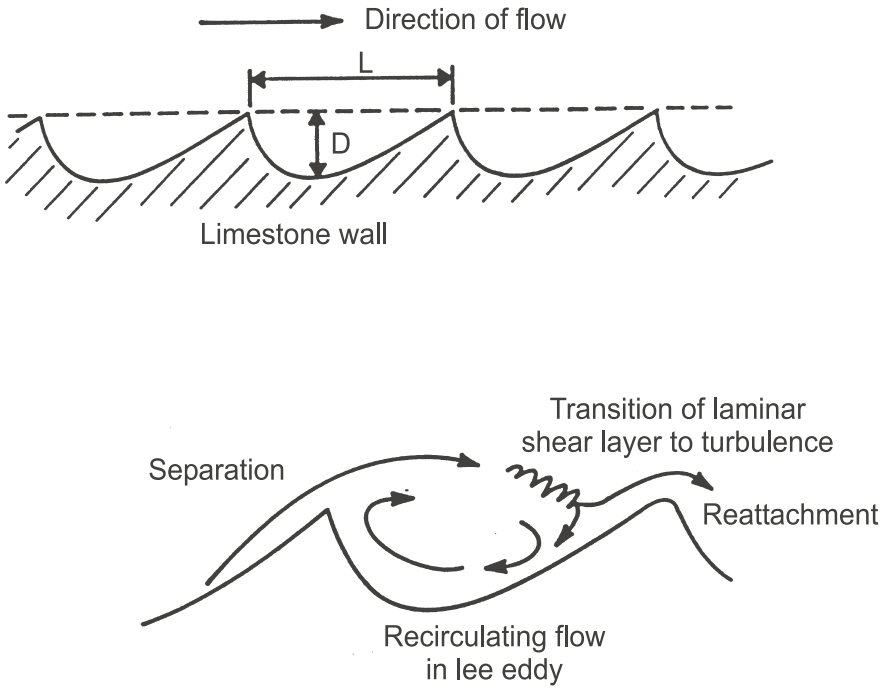

Fig. 2.4 Scallops in paleokarst allow the estimation of flow velocities (WHITE 1988)
Top: cross sections of scalloped wall showing characteristic length
Bottom: flow pattern over the scallop surface, as described by CURL (1974)

Tab. 2.1 Flowforms in subsurface streams

Flowform	Free surface flow	Pipe flow	Laminar flow	Turbulent flow	Subcritical flow	Supercritical flow
Regular channel	x	x	x	x	x	
Irregular channel	x	x	x	x	x	
Pocketed channel	x	x	(x)	x	x	
Angular channel	x	x	(x)	x	x	
Confluent	x	x	(x)	x		
Pool	x	x		x	x	
Maze passage	x	x	(x)	x	x	
Pothole	x	x		x	x	(x)
Hydraulic jump	x			x		x
Waterfall	x			x		x
Sump	x		(x)	x	x	(x)

exist in a free surface flow. The last flowform to be described here is typical and frequently found in caves: a sump which occurs when the ceiling dips down under the water level. When this happens gently it is just a transition from open channel flow to pipe flow and therefore will not produce major secondary currents. But a sump may also contain sharp vertical bends and therefore one example is included in the list of basic flowforms.

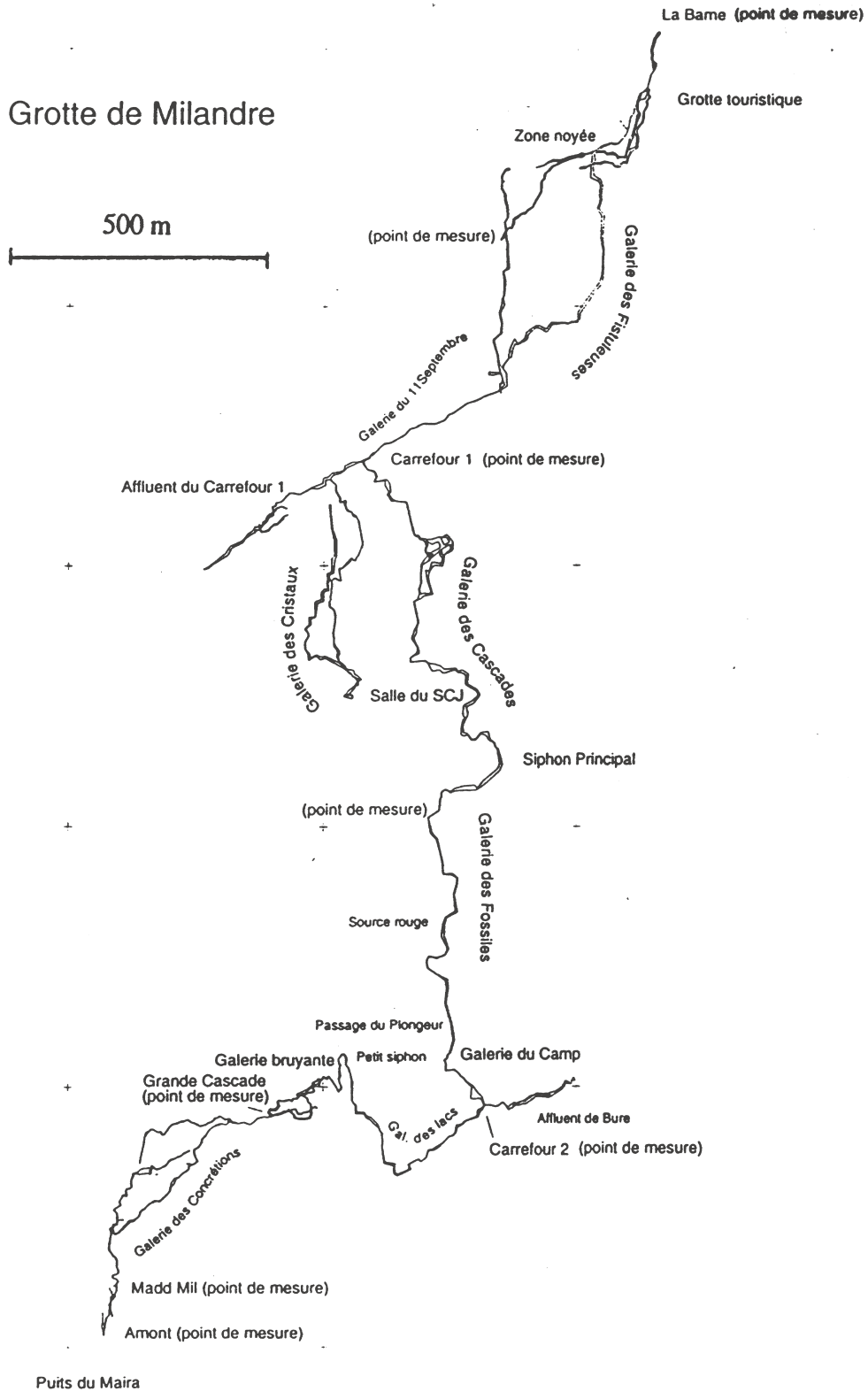

Fig. 2.5 **Map of Milandre cave, Ajoie, Switzerland** (JEANNIN 1996)

See Fig. 1.1 for geographical location.
10 km of galleries are explored and mapped, and with the exception of two sumps, the underground river can be directly observed on a distance of more than 4 km

Vadose and phreatic flowforms

Any vadose conduit system is subject to flooding, and this will transform the free surface channel and pool flow into pipe flow conditions, changing the pressure distribution and the response of the system to head changes dramatically, but eventually not changing the secondary flows much. However, the flowforms where the free surface is important, hydraulic jump and waterfalls, will vanish into flow in a vertically bending pipe.

Measured flow velocities in conduits

One important modeling parameter that can be measured in field is flow velocity. Flow velocities in conduits may be investigated by

(1) Direct measurement of flow velocity (HAUNS 1997)

(2) Bedform-erosional features (SLABE 1995)

(3) Hydraulically-transported sediment (GALE 1981)

Also, tracing experiments may be used to measure mean flow velocities. Flow velocities from scallops in 13 different caves vary from 0.03 to 1.2 m/s (GOODCHILD 1971, WHITE 1976, WHITE 1970).

Table 2.1 lists the classification of flowforms deduced from the above field investigations of conduit morphology. Perspective views of those flowforms that have been simulated are shown in Chapter 6.

2.3.1 Drop-pool sequence in torrential flow

Except for long low-gradient channels karst conduit flow has a torrential or drop-pool character, i.e. deep sections with tranquil flow are intermitted by shallow sections with rapid flow, often in the supercritical flow regime. The gradient of the bed will be locally negative, mostly at the beginning of a narrow or rapid section (see Fig. 2.6). This allows to break up the bed into a sequence of hydraulically independent segments, assuming that at normal discharge conditions there is no feedback of the flow below a waterfall to the area upstream. This explains why flow in a karst conduit cannot be successfully described by formulae for irrigation - or other man-made - channels assuming a monotonous gradient bed (JEANNIN 1996, MARECHAL 1994).

This concept of independent sections is also used for the modeling of local flowforms. The bed gradient is set to zero and the outflow is controlled by a weir-like boundary condition (comp. Chapter 3).

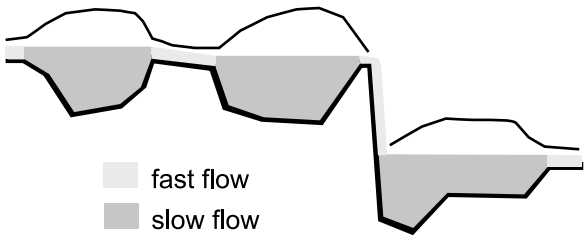

Fig. 2.6 Drop-pool sequence in a conduit: tranquil flow segments are intermitted by rapid, supercritical flow

3 Numerical model and laboratory model

3.1 Numerical model

In karst, a substantial mechanism of groundwater transport is conduit flow which is known to be turbulent (Atkinson 1977, Gale 1984, White 1970), with critical Reynolds numbers certainly lower in irregular conduits than in regular channels (White 1988). Flow velocities may be in the supercritical regime. Therefore, the Navier-Stokes equations for incompressible flow have to be solved to describe these flow fields adequately.

3.1.1 Basic equations

The Navier-Stokes equations can be derived from a general transport equation for extensive quantities (Honerkamp & Römer 1986). For a fluid or gas dynamics problem the Navier-Stokes equations in coordinate-independent vector notation are:

$$\frac{\partial}{\partial t}\rho + \nabla \cdot (\rho \underline{u}) = 0 \tag{3.1}$$

$$\frac{\partial}{\partial t}\rho \underline{u} + \nabla \cdot (\rho \underline{u} \otimes \underline{u}) = -\nabla p + \Delta \cdot (\mu \underline{u}) + F_B \tag{3.2}$$

ρ is the density of the fluid, $\underline{u}$ the local velocity vector and F_B a body force i.e. a force acting directly on the fluid volume. Equation 3.1 comes from mass conservation, equation 3.2 describes the behavior of an infinitesimal volume element in the fluid exposed to inner and outer forces. Viscous friction, pressure gradient and inertia are examples for inner forces, buoyancy, magnetic or centrifugal are examples for outer forces. Water flow may be treated as incompressible flow, therefore $\partial/\partial t\, p = 0$ and the equations simplify in the liquid phase:

$$\nabla \cdot (\underline{u}) = 0 \tag{3.3}$$

$$\nabla \cdot (\underline{u} \otimes \underline{u}) = -\nabla p + \Delta \cdot (\mu \underline{u}) + F_B \tag{3.4}$$

Water is a Newtonian fluid, that means the stress tensor will be isotropic. As the temperature of the water changes very little and slowly we consider the problem to be isothermal, there is no buoyancy force due to temperature gradients.

3.1.2 Existing work on numerical modeling of karst conduits and rivers

Double porosity finite difference models have been applied to karst systems on a catchment basin scale with good success in the past (Bonnet 1976, Teutsch 1988, Sauter 1992, Morlok 1996). A sophisticated 3D finite element model has been developed by Kiraly (1979) and further applied by Rossier & Kiraly (1992). However this is not an appropriate numerical model to study transport processes on a local scale, when detailed values of speed and turbulent energy on the scale of a conduit itself are needed. In order to do this, a model solving the

Navier-Stokes equations, at least in a depth-averaged form, and an appropriate turbulence closure are necessary. CFD models of this type have been applied to limited sections of surface rivers (RASTOGI 1978, DEMUREN 1968, SOTIROPOULOS 1995, SOTIROPOULOS 1998). One application for this is the area around hydropower intakes and outlets, where precise prediction of secondary currents may be desired.

Generally it is admitted that modeling of flow in natural rivers poses difficulty even to state of the art flow models, due to rapidly varying topographies, small-scale roughness and the free water surface induce complex three-dimensional shear flows including secondary currents, eddy and vortex formation and turbulence anisotropy (SOTIROPOULOS 1998). Torrential flows include frequent segments with supercritical flow and therefore are still more difficult to handle.

Based on this it seems reasonable to focus on small flowforms representing a short conduit segment of 1-10 m, i.e. 0.2% of the conduit length of Milandre.

On this background it seems reasonable to attempt numerical simulation of flow in karst conduits with an engineering CFD program which has to have some sort of turbulence closure and the possibility to include free surfaces and tracer and particle transport subroutines.

3.1.3 Choice of flow solver software

The flow solver CFX-F3D from AEA technology was found to comply to the above requirements. It was originally developed for mechanical and nuclear engineering purposes, but it was also utilized for several environmental applications like fluvial hydraulics (HORAT 1996, HERMANN 1996), powder avalanche kinetics (HERMANN 1990) and sediment transport in alpine rivers and reservoirs (SCHLEISS 1998).

3.1.4 Finite volume method

Finite differences, finite volumes and finite elements are the basic methods used in computational fluid dynamics. The volume between neighboring points will be referred to as a volume element, generally a parallelepiped. Finite elements may have triangular or tetrahedral volume elements. They are well-suited for very complex geometries. The Galerkin process is used to resolve the equation system. However, for large and time dependent problems, the finite element method is quite slow, and grid construction is difficult in 3D. The finite difference method is based on a homogeneous, rectangular grid. It is computationally fast and stable, but many cells are wasted in complex geometries, and there is no possibility to increase the grid density around hotspots (hotspots are areas of high interest in the computational domain, e.g. an edge where turbulence is created). In the finite volume method, the cells are rectangles or bricks, whose edges can be curvilinear and meet at an angle different from 90^{o}. However, too much deformation decreases the numeric stability, therefore angles should preferably be between 45 and 135 degrees. The grid is block-structured and by joining blocks complex branched geometries can be mapped, or the density increased at regions of interest. Fig. 3.1b shows how a circular pool is constructed by wrapping a curvilinear block around a quadratic block. The physical grid must be always structured in the sense that point *j-1* is followed by *j* (comp. Fig. 3.1a), in order to be mapped to the computational grid which is again rectilinear, but on a non-orthogonal coordinate system. The transformation between the two grids involves

elements of tensor calculus and will later influence the differencing scheme for the equations. The Navier-Stokes equations will contain additional force terms originating from the transformation of an isotropic advection-diffusion problem in physical space to an anisotropic advection-diffusion problem in computational space. The variables are discretized at the centers of the elements, and the equations are discretized treating these elements as control volumes for the conservation laws. The Navier-Stokes equations have to be satisfied for each control volume simultaneously. The default differencing scheme is UPWIND. Other available differencing schemes are HYBRID, CENTRAL and QUICK. The SIMPLEC algorithm is used for velocity-pressure coupling.

3.1.5 Turbulence modeling with the k-ε closure

Imagine the shear forces on a volume element becoming larger then the viscous damping. It will be pulled out of the laminar flow it followed and start to rotate, therefore breaking up the laminar flow field. There are no volume elements defined in a fluid, but the above described happens at the onset of turbulence at different scales. Generally vortices will be created at larger scales and then cascade down to the Kolmogorov scale of smallest eddies, which is in the range of 10 to 100 μm in the media we are considering. Turbulence changes many important properties of a fluid, including apparent viscosity, heat and concentration transport. The turbulence-driven diffusion of tracer may be two orders of magnitude higher than the molecular diffusion rate. When direct calculation of the vortex cascade is attempted, the resolution required grows with $Re^{9/4}$. For most turbulent problems a grid that resolves the small eddies is not feasible with current technology. Therefore a turbulence model is needed. Several turbulence models are implemented in CFX. We chose to work with the k-ε model which is extensively tested and known to perform reasonably well to engineering accuracy in a wide range of applications. The k-ε model solves the transport equations for the Reynolds-averaged quantities:

$$\overline{\Phi}(t) = \frac{1}{2\Delta t}\int_{t-\Delta t}^{t+\Delta t}\Phi(\tau)d\tau \tag{3.5}$$

Φ represents any averaged quantity, e.g. velocity, pressure. It is important that the frequency of turbulent fluctuations and the frequency of mean value fluctuations are well separated. So Δt in equation 3.5 can be chosen large relative to the time scale of turbulent fluctuations, but small relative to the time scale of the problem we wish to solve. Under this assumption, fields Ξ can be split into their mean and fluctuating parts:

$$\Xi = \overline{\Xi} + \Xi' \tag{3.6}$$

With the laws for the averaged quantities, Equation 3.4 can be rewritten in Reynolds-averaged form:

$$\frac{\partial}{\partial t}\rho\underline{u} + \nabla\cdot(\rho\underline{u}\otimes\underline{u}) = -\nabla p + \Delta(\mu\underline{u}) - \nabla\cdot(\rho\underline{u'}\otimes\underline{u'}) \tag{3.7}$$

where the bars for all variables as well as the body force term have been dropped for clarity. The additional term describes the influence of the turbulent eddies on the mean flow and has the dimension of a stress. One possibility to model is to introduce turbulent viscosity by setting

$\overline{\underline{u}' \otimes \underline{u}'} = \nu_t(\nabla \underline{u} + \nabla \underline{u}^T)$, where $\nu_t = c_\mu \frac{K^2}{\varepsilon}$. Here K is the local turbulent kinetic energy and ε it's decay rate. K, ε and c_μ have been generally determined from laboratory experiments.

3.1.6 Free surface modeling with a two-fluid-model

For vadose flowforms in the supercritical flow regime, i.e. simulations of the second type the position of the free surface must be found in the simulation. One possibility to do this is using a multiphase flow model for air and water. The Navier-Stokes equations are solved for both phases in the whole flow domain. The volume fractions for all phases in each cell must add up to unity. However most cells will be almost completely filled by one phase and contain only a tiny fraction of the other. The free surface is then defined as the plane with 50% water. For quasi-stationary flow conditions the transition zone should not be larger than one cell. A surface sharpening algorithm is implemented in CFX to keep the transition zone thinner than one cell and to overcome the numerical diffusion. Fig. 3.1c shows the principle of a free surface calculation by a multiphase approach.

3.1.7 Tracer transport modeling

In CFX transport of a conservative tracer plume may be calculated with the scalar advection-diffusion equation (ADE), which is, in coordinate independent form and for incompressible flow:

$$\frac{\partial}{\partial t}\Psi = -\nabla \cdot (\underline{u}'\Psi + D_t \nabla \Psi) \tag{3.8}$$

assuming that the tracer is not influencing the flow. Ψ is an additional species mass fraction, $\underline{u}$ the flow velocity and D_t is the coefficient of turbulent diffusion. In special cases it may be necessary to introduce an extra phase. This is the case for NaCl, when tracer in a certain concentration may influence the fluid density and thus the hydraulics.

3.2 Solution strategies for different flowforms

With all of the above we might be ready to attack the complicated case, i.e. a waterfall, which generally is of the three-dimensional, turbulent, time dependent and free-surface with air-mixing type. However, this requires a very large computer and it may be wiser to start with hydraulically simpler cases, which may expose even more interesting transport phenomena. Every basic flowform listed in Chapter 2 has it's appropriate modeling, and often it is possible to introduce simplifications of the numerical approach allowing to save a lot of computational effort. Doing this leads to two principal types of simulations:

- Tranquil flow may be treated within a rigid-lid approximation. This means that the water surface is kept in a fixed position and it has the big advantage that, using a single phase model, it is possible to calculate a steady state solution and then do the tracer transport without further iterations of the hydrodynamic equations, thus only solving the scalar advection-diffusion equation.

- Vertical structures with a constant cross section leading to supercritical flow may be treated on a zx-plane cut (in the following by convention x shall be the major flow direction while z is anti-parallel to gravity).

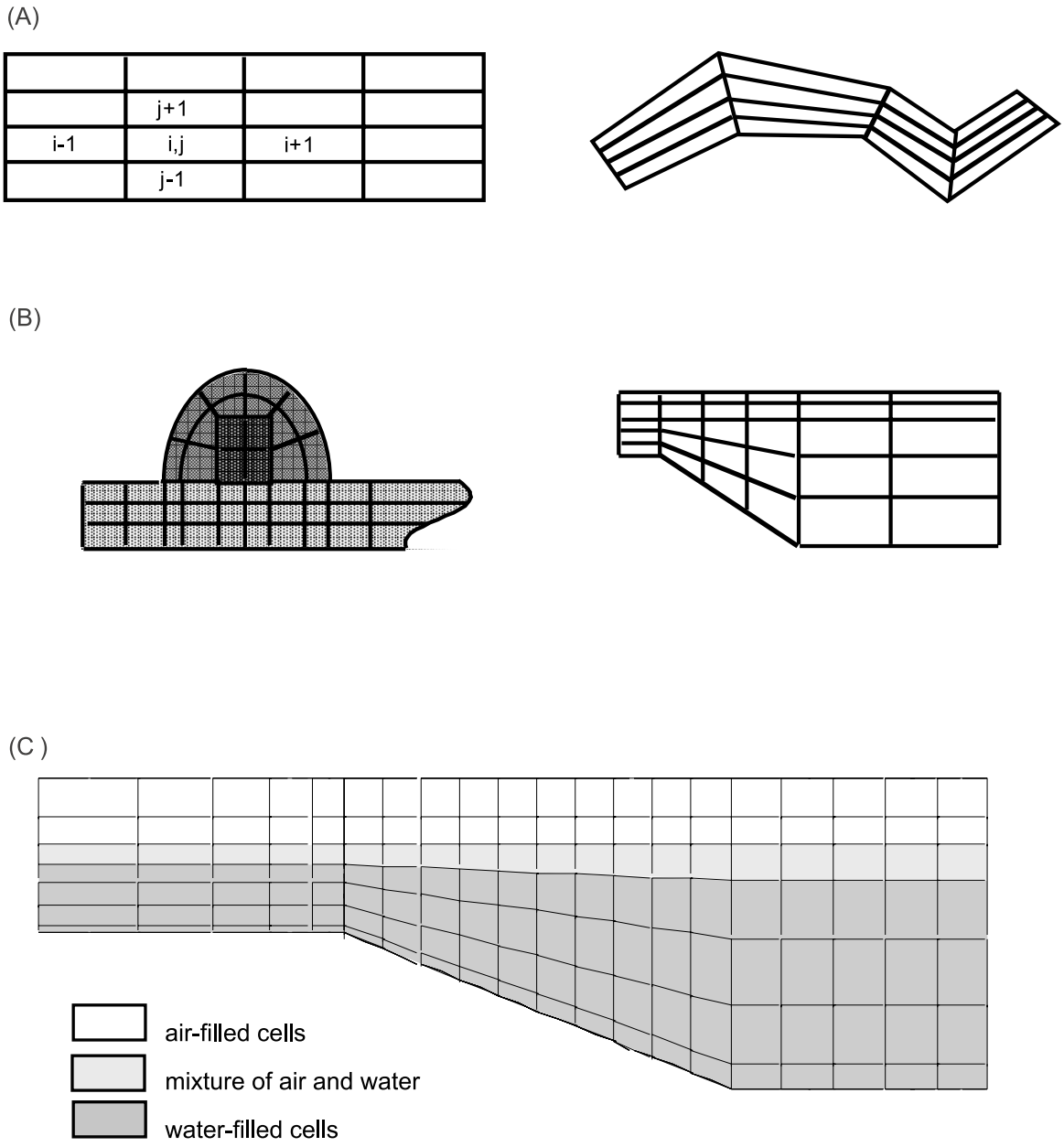

Fig. 3.1 The finite volume method is used for the numerical simulations

(A) Physical grid fitted to an irregular channel and corresponding computational grid
(B) Body fitted grid for varying channel geometries - blocks are shaded
(C) Free surface calculation with a two-fluid-model

Figure 3.2 illustrates these two principal types.

As the modeled passages are quite short, it is important to find appropriate inlet and outlet boundary conditions. For a pipe flow this turns out to be quite simple. While the entrance and exit are at the same hydraulic head, a mass flow condition with the same discharge values will do. When there is a head difference, a pressure boundary condition at the entrance will allow for a correct pressure distribution and will adjust to the mass flow at the exit. On a rigid lid approximation mass flow conditions will be appropriate. A pressure boundary condition at the outlet together with a fixed inlet velocity also works. This corresponds to a free overfall as it is used in the laboratory model. Assuming a free overfall at the end is favorable because it allows easy control of the water depth in a short geometry, and it corresponds to a natural situation in a drop-pool stream. Still, while using a rigid-lid approximation, as the water level is fixed as a boundary condition, its position has to be determined which is one of more complicated tasks in hydraulics (SIMON 1992). One way to do this is to measure the water level in an appropriate experimental or field setup. Another possibility is to use a general weir or free overfall formula on an appropriately shaped outlet boundary condition. The relation for a sharp-crested, rectangular weir is (FINNEMORE 1985):

$$H = \left(\frac{Q}{C_w B}\right)^{2/3} \tag{3.9}$$

H is the water height over weir crest, without the drawdown over the edge, Q the discharge, B the channel width and C_w a constant that depends mainly on the shape of the weir crest. Fig. 3.3 shows the resulting water depth for the laboratory setup, with measured values for three different discharges. The value of C_w has been adjusted to fit the measured values and is used for all the numerical simulaions.

The head loss along the channel, as often considered in engineering formulae for channel layout, is completely suppressed because the geometries are so short and the gradients very small.

In free surface scenarios the head loss may be large on a very small horizontal distance, but it is estimated during the calculation of the free surface.

3.2.1 Implementation of the numerical approach with CFX-F3D

In this paragraph the application of CFX to calculation of flow and tracer passage in short pieces of conduit is explained in detail. Fig. 3.4 shows a flow diagram of this.

To resolve a flow problem in a geometry with CFX, a grid file for that geometry must be created. The corner points of the geometry are put into a point file. In the cases treated here a file containing points in a plane e.g. for the bed, will be sufficient. The flow domain can then be created by extruding this plane. The pointfile is then opened with CFX-meshbuild and blocks, subdivisions and the patches describing the boundary conditions are set. The

default is a wall patch, therefore only inlets, outlets (a pressure boundary condition is nearly always chosen for the outlet here) and symmetry boundary conditions for the air/water surface in the rigid lid approximation have to be set.

In the CFX command file the type of flow (2D or 3D, turbulent flow , buoyant flow, transient or steady-state solution) is specified. Also, a time step interval and the desired number of time steps for transient runs, or a maximum number of iterations and a required precision (mass source tolerance) for steady-state runs are set. The command file contains also physical properties of the fluid and it's environment, like density, viscosity, temperature and the gravity vector for buoyant flow. Also, an appropriate solution algorithm and a turbulence closure can be chosen in the command file. Finally, the output options must be set. All variables of the run at all grid points or a subset of them may be written to file at a chosen interval (e.g. every 50th time step). This is needed to produce animations in time, but produces very large dump files. It is also possible to write the value of one variable at a specified sample point to a separate file. This option is used for tracer passage runs on a steady state velocity field, when the other variables do not change during the run. Dumpfile sizes range from about 8 Mb for a typical grid size when only the final solution of a steady state run is written, to several hundred Mb when a dumpfile with all variables is written every some time steps. A linegraph file for a breakthrough curve over 10'000 time steps with a value for every time step has approximately 300 Kb.

With the command file and a geometry file the run can be started. Sometimes a FORTRAN file is needed when user fortran routines are added. This was used in this study in order to set an initial velocity field. With the restart option, a run is initialized with the result variables from a previous simulation. In the present application of CFX, for the rigid-lid approximation type of simulation this looks the following:

- A steady state flow solution is found, with one command file. By convention, this has the extension *-ini* here.
- The *-ini* result file is used with a *-ti* command file where tracer is injected during a few time steps, i.e. the value of the variable 'user scalar' is set to unity on the inlet.
- The *-ti* result file is used to start the *-t* file, which usually goes over 10'000 time steps and where the passage of the tracer plume in the flow domain is computed.

No steady state solution exists for the supercritical flow, i.e. two-fluid-model simulations. Here the procedure is:

- Some seconds of simulation are needed to get a quasi-stationary state. The velocity distibution and position of the free surface keep on fluctuating.
- Then tracer is injected, and the flow simulation must go on during the whole numerical tracer experiment.

The dump files may be converted to a format that can be read by appropriate visualization software. The visualization software utilized in this study is introduced in the next paragraph.

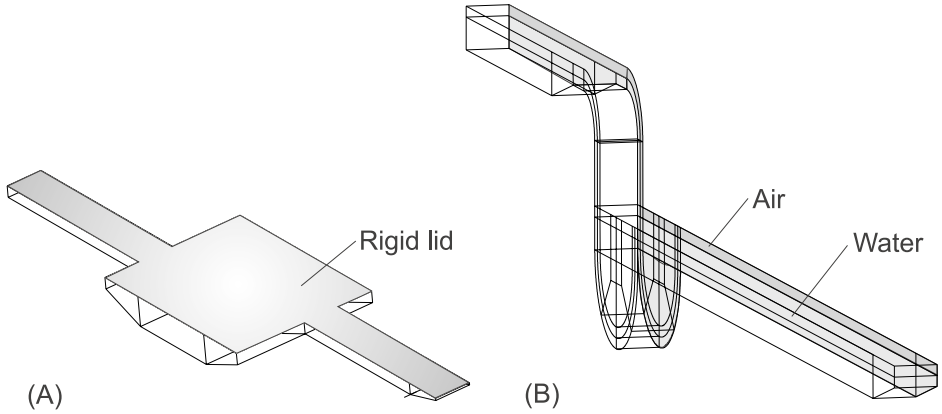

Fig. 3.2 Different approaches are used for subcritical and supercritical flow

(A) Subcritical flows with little variation of depth: a rigid lid approximation is utilized for the water surface, and the number of cells in z-direction is low (typically 3-4)
(B) Supercritical flows: the multiphase flow model is utilized to estimate the position of the free surface; to save computational effort, no variation of the horizontal section is assumed. This allows to work with only one layer of cells in the y-direction

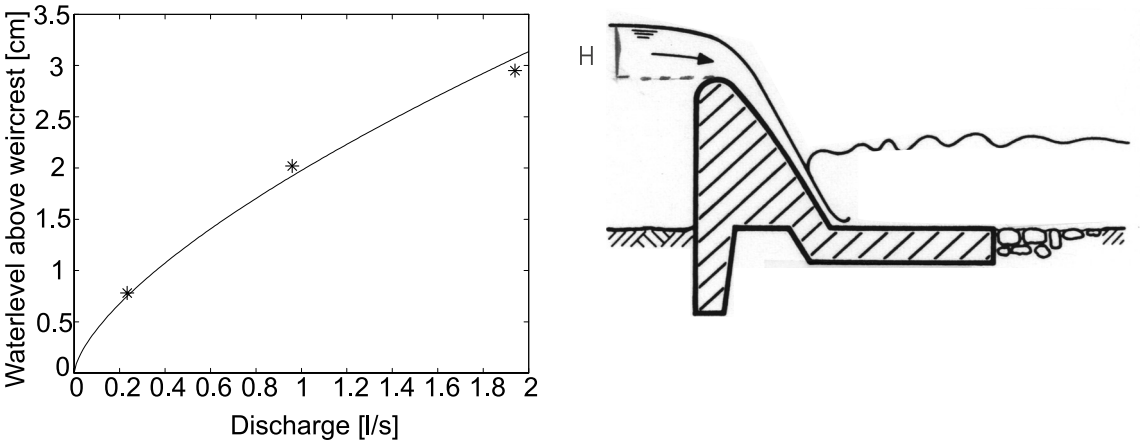

Fig. 3.3 A weir outlet allows to estimate the waterlevel in geometries with tranquil flow

Left: discharge-waterlevel function for a free overfall or weir exit: Eqn. 3.9 is fitted to the measured values from the laboratory model
Right: flow over a weir (VISCHER 1984, modified)

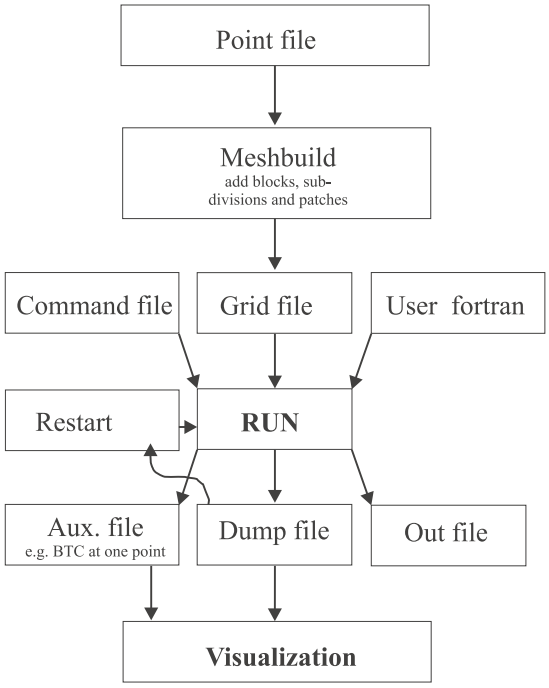

Fig. 3.4 Flow diagram of CFX runs

3.2.2 Visualization

The results of the most sophisticated CFD flow solver are hard to interpret without an appropriate visualization program. There is a large number of available visualization techniques, like a simple velocity arrow generator and contour line plots to more sophisticated ones like isosurfaces to represent a scalar variable. Recent computer science literature lists more than 50 of them. Commercial visualization packages contain the standard visualization tools. In this study, we used on one hand the commercial programs RUNVIEW, which is part of the CFX environment and a second commercial program named FIELDVIEW. On the other hand, when complex specialized analyses have to be made, working with those packages becomes awkward and time-consuming. This is natural because they cannot be tailored to fit all user's needs. At this point it was very helpful to work with the visualization platform ZoomIn (SANGLARD 1999), which is currently under development at the Computer science department of Neuchatel University. The structure of ZoomIn allows easy integration of user defined visualization tools. For this study we mainly developed:

- A glyph that allows to create a 'breakthrough curve', i.e. a graph concentration vs. time, at an arbitrary sampling point within the geometry. With a standard visualization tool this is quite time-consuming.

- An integration routine (surface inside a contour line) for the boundary shear stress distribution. This is needed for the particle deposition model. This allows to work with a large number of contour lines without having to do the integration manually.

3.3 Laboratory model

A simplified (rectangular) scaled model of a single pool in an underground river was chosen to study the passage of a tracer plume. The shape is rectangular to simplify the irregular shorelines of natural basins. We intended to build a schematic model that reproduces the aspect ratio of characteristic dimensions (bed geometry, water depth, discharge) found in nature. Hence the physical dimensions of this model are related to the dimensions of a large lake in the Grotte de Milandre. This is approximately 6 m by 5 m, and 1 m deep in the cave.

3.3.1 Construction and measuring techniques in the laboratory model

The physical dimensions of the laboratory model are 1 m by 0.8 m for the pool which is 0.15 m deep. Entry and exit channel are considered on a length of 1 m each with a width of 0.2 m. The floor of the basin is 0.1 m lower than the channel floors. At the end the water falls over a spillway into a basin. There is no gradient on the model, the water level is controlled by the equilibrium between inflow and the discharge of the spillway. The basin is built from plywood; the edges are sealed with silicon. Two sides are made of glass to allow lateral illumination. Inflow is held constant with an overflow basin fed by a regulated pump from a large reservoir. The absolute discharge rate is estimated by the time needed to fill a 100 liters barrel at the exit, the stability of the discharge in time is monitored with a pressure sensor. Grids at the entrance calm the flow. Fig. 3.5 shows the laboratory model.

Tracer substance is fluoresceine, also widely used in field tracer experiments. At the exit a fluorometer measures the concentration to get a continuous breakthrough curve of the tracer concentration. Simultaneously the basin is illuminated by UV neon from the sides and the passage of the tracer cloud is filmed from above with a digital video camera. The pictures are acquired from video by computer at one image per second and treated using Image 6.27 (NIH) (see Fig. 3.6). The spatial tracer content is estimated from pixel colors with reference to average colors obtained from standards. Due to the small number of acquisition colors (256) the given concentrations must be considered as semi-quantitative only.

3.3.2 Scaling

While a numerical model can easily be rescaled to field dimensions, there are technical limitations (available space and pump discharge) for the laboratory model. In this case it was possible to build a 1:5 scale model. When there is a free surface the two dimensionless numbers Fr and Re are important:

$$Fr = \frac{U}{\sqrt{gl}} \tag{3.10}$$

$$\mathrm{Re} = \frac{lU}{\nu} \tag{3.11}$$

Thereby g is the gravitational acceleration, l a characteristic length and U a characteristic velocity of the flow. Fr gives the ratio of inertia and driving pressure gradient, while Re stands for the ratio of inertia and shear. When there is a free surface in a scale model containing it, it is more important to conserve the Froude number Fr than the Reynolds number Re.

Otherwise the free surface would be at the wrong position, resulting in an overspill. This happens because velocity in a Froude model is adapted with the inverse square root of the scaling factor, while in a Reynolds model it increases linearly with the scaling factor. For open channel flows, usually the water depth is taken for a characteristic length. At our test site 'Grotte de Milandre', the average size of large pools is 1 m of depth for 5 m of length and width. The flow velocity at the entrance point into the pool is given by the discharge divided by the cross-section of the input channel (0.07 m by 0.2 m). To conserve the Froude number while reducing the model scale, the characteristic velocity must be scaled by the square root of the length ratio.

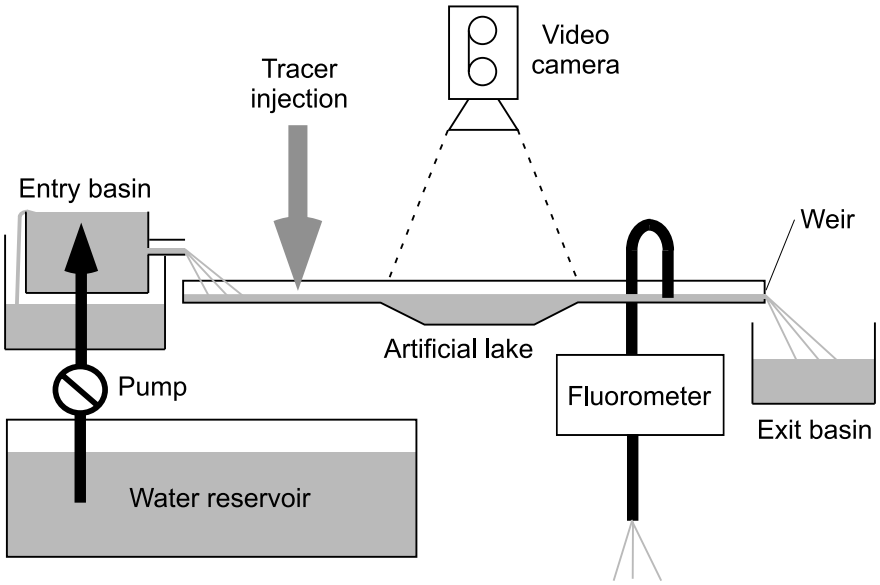

Fig. 3.5 Schematic view of the laboratory model with inlet, basin and fluorometer at the exit

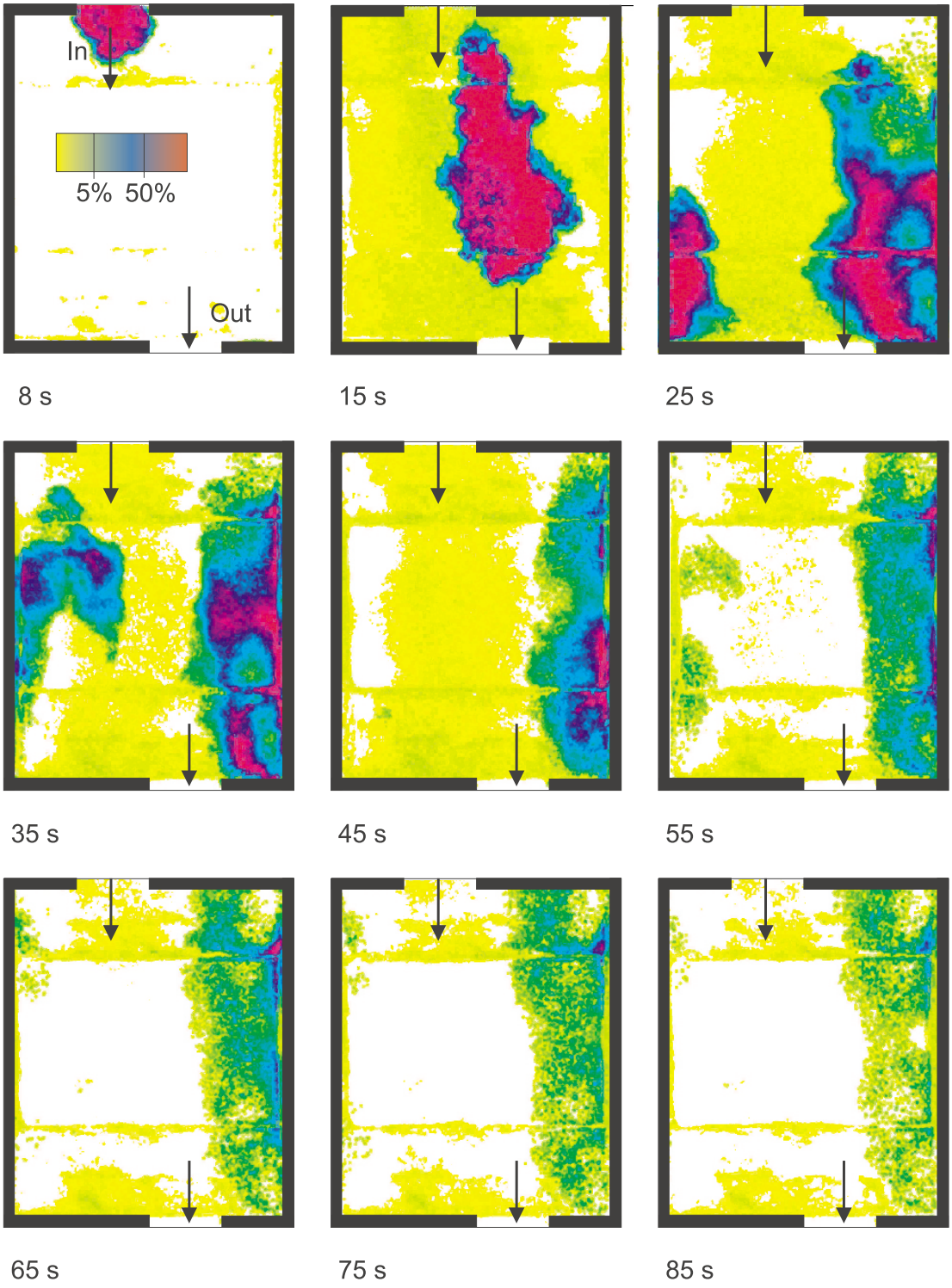

Fig. 3.6 **Passage of a uranine tracer plume in the laboratory model as filmed with the video camera. The discharge is 1.96 l/s and 500 ml of a solution containing 0.002 g/l have been injected. Refering to average colors from standards, the intensity of yellow/green fluorescence has been mapped to a rainbow color scale**

4 Tracer breakthrough curve fitting

In this chapter, a fitting method based on an analytical solution of the advection-diffusion equation is developed. The analytical solution is fitted to the rising limb of the experimental breakthrough curve.

Tailing of a breakthrough curve, i.e. non-negligible tracer concentrations remaining after the passage of the main peak, is quantitatively defined in relation to the falling limb of the analytical solution. This allows a more quantitative characterization of tracer breakthrough curves (BTC) in karst conduits. This fitting procedure is used to characterize the results from the numerical simulations, including their extension to conduit scenarios by concatenated transfer functions (see Chapter 7), the results from the laboratory model and some field results from Milandre cave.

4.1 Advection-diffusion equation for turbulent flow

It has been shown experimentally that the advection-diffusion equation in a slightly modified form may be used for tracer transport in fully turbulent flow (TAYLOR 1954). The molecular diffusion coefficient has then to be replaced by a turbulent diffusion coefficient. From the basic Fick's Law for diffusion, the 1D diffusion equation is:

$$\frac{\partial C}{\partial t} = D\frac{\partial^2 C}{\partial x^2} \tag{4.1}$$

with a concentration C and a general diffusion coefficient D. An additional advection term leads to the advection-diffusion equation (ADE). This equation is often used in porous media, where u is the average velocity, D_m the molecular diffusion coefficient and D_t the turbulent diffusion coefficient:

$$\frac{\partial C}{\partial t} = (D_m + D_t)\frac{\partial^2 C}{\partial x^2} - u\frac{\partial C}{\partial x} \tag{4.2}$$

In a numerical simulation describing turbulent flow, $D = (D_m + D_t)$. D_t describes the effect of mixing by vortex cascades. In fully developed turbulence, this coefficient is much higher than the molecular diffusion (due to Brownian motion), and the latter can be neglected (CFDS 1996). Therefore in the following we set $D \equiv D_t$. The equation writes then:

$$\frac{\partial C}{\partial t} = D\frac{\partial^2 C}{\partial x^2} - u\frac{\partial C}{\partial x} \tag{4.3}$$

In order to fit a tracer breakthrough curve, u is replaced by the peak velocity u_{peak} of the plume, which may be calculated from peak passage time when the path length is known:

$$u_{peak} = \frac{L}{t_{peak}} \tag{4.4}$$

The 1D-solution of equation 4.3 at a distance L downstream from the injection point for a Dirac input of a mass M of tracer, given by KINZELBACH (1992), is:

$$C(x=L,t)=\frac{M}{\sqrt{4Dt}}\exp\left[-\frac{(L-ut)^2}{4Dt}\right] \tag{4.5}$$

where C and D are defined as above, t is the time, u the tracer peak velocity and L the length at which the concentration is measured. This solution will be used to fit experimental or simulated BTC. Note that this curve is symmetric in space, i.e. for a given time, but dissymmetric when concentration is measured through time at a given distance. All simulated curves (except the one for the flowtube example) are fitted on two points of the rising limb, at the maximum and half the maximum concentration, respectively.

4.2 Tailing

All curves in geometries with finite physical boundaries will have a falling limb that is different from the fit with equation 4.5. Usually the falling limb will lag behind the fit on the rising limb, and we call this a tailing or retardation, a sign that some particles of tracer have a much longer residence time in the flowform than others. When retardation occurs, M from equation 4.5 is the non-retarded mass. The retardation percentage shall be defined as the ratio of the retarded to the non-retarded mass. It can be computed as the ratio of the surfaces under the fitted curve and the measured or simulated breakthrough curve. (The curve of the flowtube is fitted to the peak value only, because there is no retardation in this case.)

The fitting procedure consists in finding the time of the peak, maximum of the BTC, t_{peak}. Then, as L is known: $u = L/t_{peak}$ and t_{mid}, the time at which the mid of the concentration of the peak is reached, defined by $C(t_{mid}) = C(t_{peak})/2$ and $t_{mid} < t_{peak}$, can be found on the BTC. At that point we find:

$$\exp\left[-\frac{(L-ut_{mid})^2}{4Dt_{mid}}\right]=\frac{1}{2}\sqrt{\frac{t_{mid}}{t_{peak}}} \tag{4.6}$$

so that,

$$D=-\frac{(L-ut_{mid})^2}{4t_{mid}\ln(\frac{1}{2}\sqrt{\frac{t_{mid}}{t_{peak}}})} \tag{4.7}$$

Using this value for D in equation 4.5 gives the fitted analytical curve. In the following the „percentage of tailing“ R is defined by the difference of the surfaces under the two curves:

$$R=-\frac{A_{curve}-A_{fit}}{A_{fit}} \tag{4.8}$$

While structures of different length are compared, it is convenient to scale the diffusion coefficient D by the distance L between injection and sampling point:

$$D^*=-\frac{D}{L} \tag{4.9}$$

The two parameters D, respectively D* and R will be used to describe the shape of different tracer breakthrough curves. The above is illustrated by Fig. 4.1 on the example of a field tracer curve from Milandre.

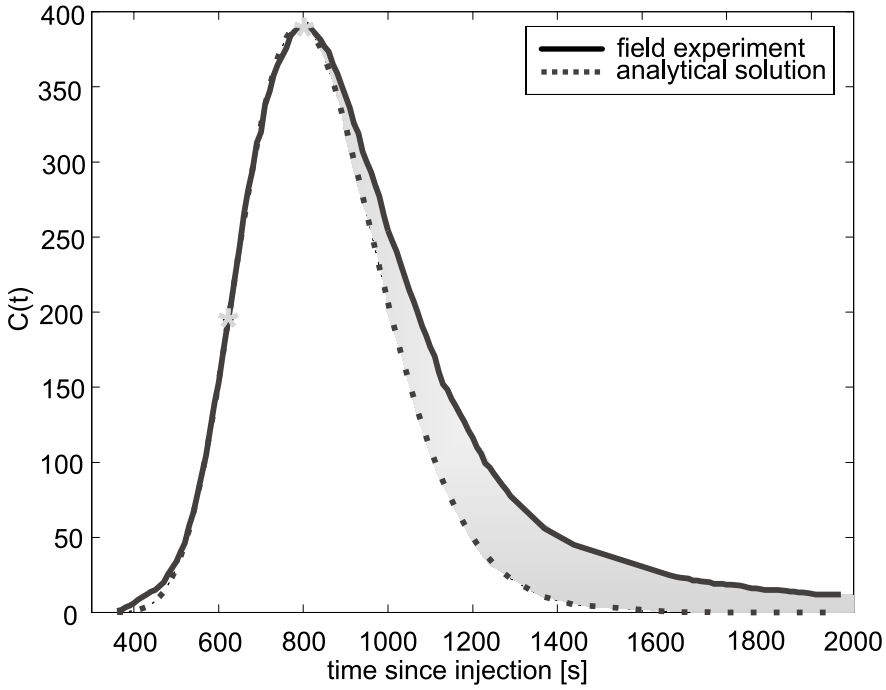

Fig. 4.1 **Example of tracer breakthrough curve fitting: the two points used for the fit are marked (*). Fitting parameters are: L = 85 m, u_{peak} = 0.0432 m/s. The shaded area corresponds to the tailing R. The resulting values are D = 0.03187 m^2/s and R = 16.12%. Breakthrough curve from a tracer experiment in Milandre, tracing A in Fig. 8.1**

5 Small particle transport and deposition

The size range of granular matter transported by water flowing in creeks, rivers and streams of different discharge and gradient extends over many orders of magnitude, from large boulders of many cubicmeters of rock weighting several tons down to particles in the submicron size range. This is also the case for rivers flowing underground, while the inlets to the underground system are large enough to allow the passage of large pieces. Obviously large blocks in a cave river may also originate from breakdown, but these will dissolve much more quickly than sediment of different chemical composition transported inside the cave by stormflows.

The mechanics of interaction of fluid flow with granular solids is the subject of numerous papers and textbooks, e.g. BOGARDI (1974), GARDE & RANGA RAJU (1985), GRAF (1971), RAUDKIVI (1982,1990), SIMONS & SENTUERK (1982) and YALIN (1972). While the sinking velocities of large and medium sized particles are reasonably high compared to the stream velocity, they will collect at the bed and be transported further as bedload or by saltation.

The small particles and colloids considered here are on the lower end of the scale (< 50 μm), and therefore adhesive forces are expected to be more important than gravitational force. Most work on cohesive sediment in wet environment has been done in the context of soil transport in agricultural channels. Yet, the understanding of the physics of erosion of cohesive material is limited and no rational models exist that are capable of quantitative predictions of erosion rates (RAUDKIVI 1993).

5.1 Attachment and resuspension of small particles

A microscopic theory is therefore needed in order to understand these transport processes. It is based on the following assumptions:

- Fine particles have settling times in the order of days. In turbulent flow they may follow eddies and vortices, and their pathline may look like a random walk without a noticeable sinking component.
- For attachment of small particles, adhesive forces are much more important than gravitational forces.
- The resuspension of particles is controlled by removal forces from the fluid. These are dominated by turbulent bursts sweeping the surface of the flow boundary (comp. Fig. 5.2).

5.1.1 Homogeneous distribution of particles in turbulent flow

The homogeneous distribution of small particles in turbulent flow has been investigated by CHANG (1997). Direct numerical simulations of homogenous isotropic turbulence were used to investigate the effect of turbulence on the transport of particles or bubbles. The particle response time T_p on turbulent fluctuations for a small particle of diameter d is

$$T_p = \frac{\rho_p}{\rho} \cdot \frac{d^2}{18\nu} \tag{5.1}$$

provided a Stokes drag law may be assumed. ρ_p is the particle density, ρ the fluid density and ν the kinematic viscosity of the fluid. The turbulence dissipation range can be characterized by the Kolmogorov time scale T_k

$$T_k = \frac{\nu^{1/2}}{\varepsilon} \tag{5.2}$$

where ε is the rate of turbulent kinetic energy dissipation. When

$$T_p / T_k << 1 \tag{5.3}$$

particles respond fully to turbulence fluctuations and therefore stay randomly distributed. As T_p/T_k increases, inertial effects will become significant and particles will tend to concentrate locally. Here the variation of T_p/T_k is controlled by ε and d, while all other parameters are constant in the flow domain. For particles with a diameter of 10 µm, T_p/T_k is always sufficiently small (about 10^{-4}) in the flowforms encountered here.

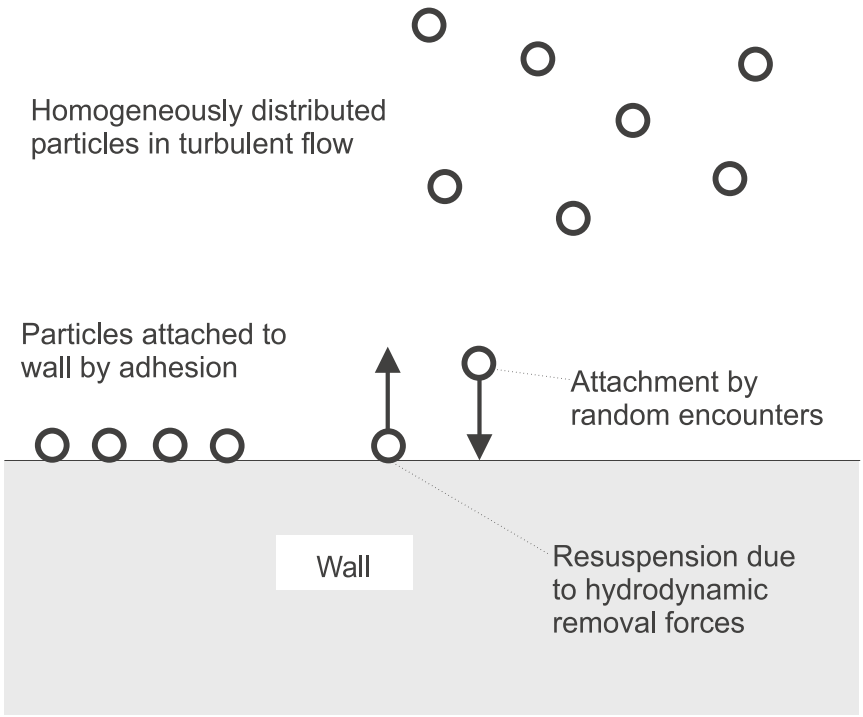

Fig. 5.1 Processes controlling particle attachment and resuspension

5.1.2 Adhesive forces on small particles

For small particles, adhesive forces include double layer repulsion or attraction, London-van-der-Waals attraction, hydration and steric interaction. The van-der-Waals forces are the more important ones (BHATTACHARYA 1978). The DVLO theory describes these intersurface forces in terms of a potential energy.

Experimental investigations on adhesion have been conducted by FUCHS (1964), ZIMON (1982), BRAATEN (1988), HOBBELS (1988) and others. Generally, adhesive forces show large variations depending on the chemical composition of the particles, their shape (HOBBELS 1988) and the nature of the fluid. BROCKMANN (1982) found that cohesive forces between small particles may be an order of magnitude higher than the gravitational force. Forces may be different in a multi-layer bed. However this approach is restricted to particle-wall interactions. Unfortunately most of the experimental work has been done on dry powders (RAUDKIVI 1990). In an aquatic environment interparticle forces may be reduced.

5.1.3 Removal forces in turbulent flow

Particles are removed from a surface by forces from the fluid acting on them. In the 1960's, a removal model based on the idea of a laminar wall sublayer in turbulent flow was proposed by CORN (1966), LARSEN (1958) and GUTTERMAN (1959). Forces derived from this kind of model were always too small to explain resuspension. Later the idea came up that local vortices may play a role in detachment, and CLEAVER & YATES (1973) proposed the model of particle removal by 'turbulent bursts', or vortices sweeping the attachment surface. This allows to introduce a threshold criterion for removal of particles of a certain size (CLEAVER & YATES 1973, PHILLIPS 1980, HUBBE 1984). NINO & GARCIA (1996) studied the shape of turbulent funnels experimentally with a high speed video system. Fig. 5.2 shows a schematic diagram of this.

CLEAVER & YATES (1996) found an empirical removal criterion expressed as

$$\tau_0 > \frac{d^{4/3}}{\beta} \tag{5.4}$$

where τ_0 is the mean wall shear stress and β is a constant depending on the particle shape, the fluid and the type of adhesive force holding the particle to the surface. BROCKMANN (1984) suggested that these chemical forces be in the range of 1..10 times the gravitational force. The choice of β for the numerical scenarios in this study is detailed in Chapter 7.

Tests of the theory of particle mobilization by hydrodynamic shear have been conducted by KRUPP (1968), VISSER (1976) and HUBBE (1987), and confined the predictions of the DVLO theory. However, these tests are limited to simple model systems of particles attached to flat surfaces, and the resulting information is probably of very little applicability to natural systems (RYAN 1996).

The mean wall shear stress τ_0 may be deduced from the numerical flow model, allowing conclusions on particle attachment in the calculated flowforms, which however have to be interpreted with care.

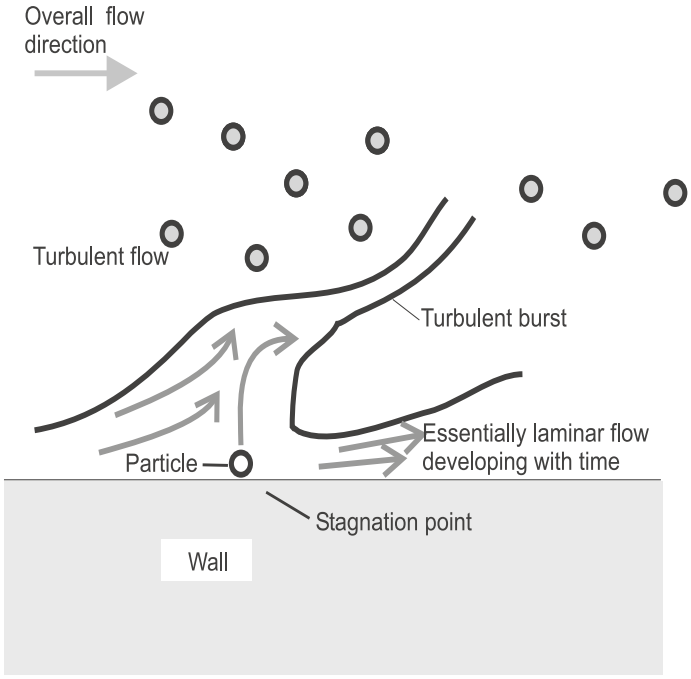

Fig. 5.2 Schematic diagram of turbulent burst in the wall region (CLEAVER & YATES 1973)

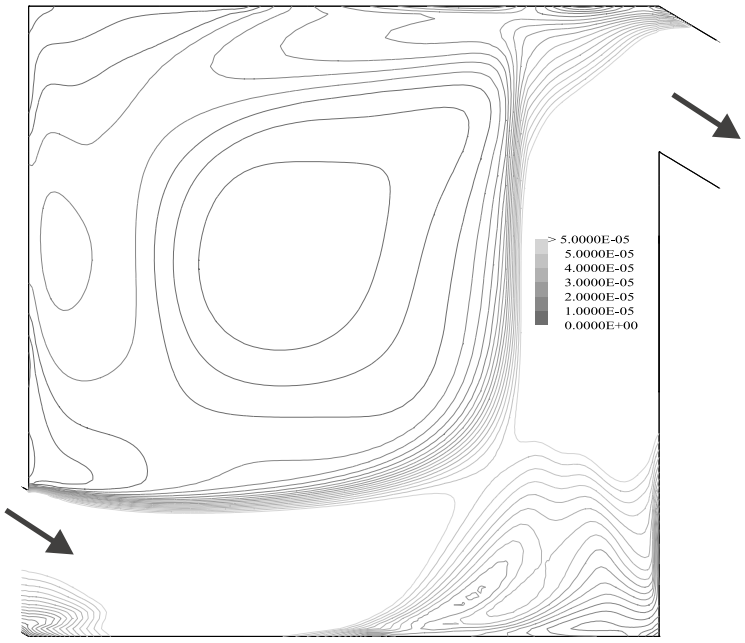

Fig. 5.3 Isolines of turbulent kinetic energy *K* on the floor of the diagonal pool

5.2 Wall shear stress from the CFX flow model

From a simulation with CFX-F3D, the turbulent shear stress on the boundaries can be derived from the flow solution (CFDS, 1994). The wall shear stress τ_0 is calculated from the turbulent kinetic energy K (from the k-ε turbulence model; the notation for the turbulent kinetic energy is chosen uppercase here to avoid conflict with the index k), in the cells adjacent to the wall

$$\tau_0 = \rho \cdot C_\mu^{1/2} K \tag{5.5}$$

where ρ is the fluid density and C_μ a constant from the k-ε model (for this application, $C_\mu = 0.3$). A shear stress contour map can be drawn, and Fig. 5.3 shows an example of this for the diagonal pool. Fig. 5.4 shows the corresponding cumulative graph (A*, comp. Eqn. 5.6) for a regular channel and the diagonal pool.

5.3 Particle size and deposition area

It is assumed that particles will attach only in a region where τ_0 is small enough to prevent immediate resuspension. This is another important assumption of this approach:

1 The available deposition area for a particle of a certain size in a flow domain is given by the boundary shear stress distribution.

The percentage of the area of the flow domain boundary, available for deposition of particles of a certain size, can thus be deduced from Fig. 5.4.

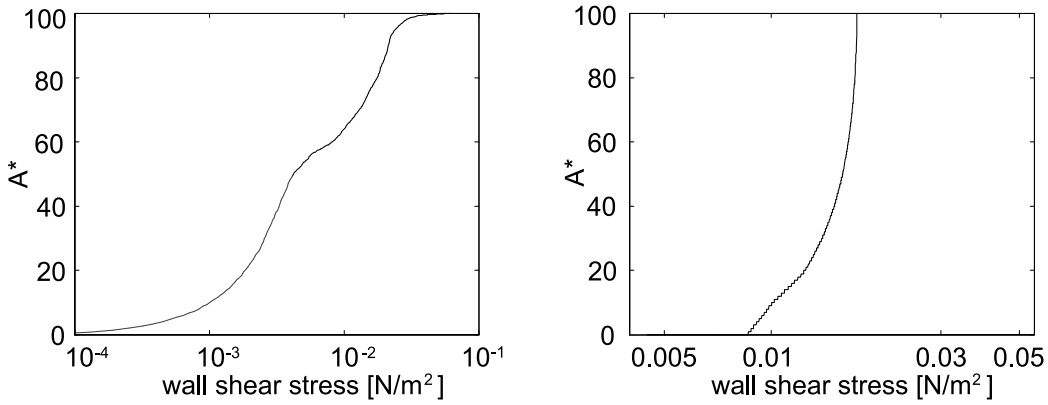

Fig. 5.4 Cumulative graphs of shear stress distribution

Left: in the 'diagonal' pool
Right: in the channel with constant cross section between x = 6 and x = 8

5.3.1 Theta function for particle removal threshold

A hypothesis has to be made on the nature of the threshold shear stress, i.e. the proportion of particles removed at the critical value and close to it.

In classical sedimentation theory, where gravitational forces are dominant, the critical shear stress $\tau_{0,crit}$ is defined where 50% of the particles are removed (GESSLER 1965). Consequently there will be a distribution describing the proportion of particles removed closely above and below this value (dashed curve in Fig. 5.5).

Meanwhile for a case where adhesive forces are dominant the exact shape of this function is not known and therefore it is replaced by a Θ function, i.e. in an area all particles with $\tau_{0,crit}$ below τ_0 will be removed will all particles above will stay attached.

Let A*(d) be the area where particles of size d may attach, scaled to the total deposition area in the geometry:

$$A^*(d) = \frac{A(\rho_0 \le \tau_{0,crit}(d))}{A_{tot}} \tag{5.6}$$

Still assuming homogeneously distributed particles, the deposition probability of a particle of size d_0 will be:

$$P(d_0) \approx A^*(d_0) \tag{5.7}$$

For short geometries as considered here, it is realistic to assume that not all particles will encounter a wall, therefore a factor C_E is introduced:

$$P(d_0) = C_E A^*(d_0) \tag{5.8}$$

C_E was chosen equal to 0.1 in the scenario in Chapter 7. For a particle size distribution N(d), a function S(d) will describe the change during passage in a geometry:

$$S(d) = 1 - P(d) \tag{5.9}$$

and

$$N_{out}(d) = S(d) \cdot N_{in}(d) \tag{5.10}$$

For numerical modeling it is convenient to discretize d into size classes, N and S are now vectors whose dimension is equal to the number of classes.

This allows to estimate the number of particles of each size that will remain in a segment. Concatenation of flow domains may lead to scenarios for larger conduits, and some of them are calculated in Chapter 7.

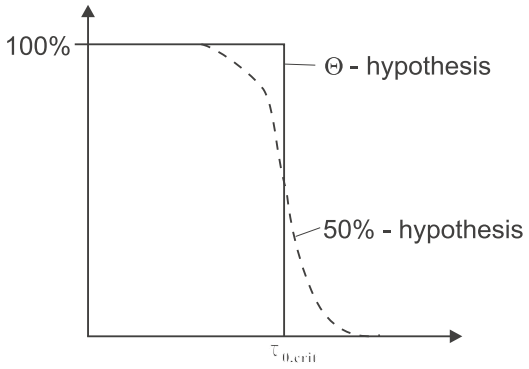

Fig. 5.5 Different hypotheses for removal proportion at critical wall shear stress

6 Simulations and results

A set of example-types of conduit flow forms has been simulated, and these are presented in this chapter. Section 6.1 contains the geometries and flow parameters. The results are presented in three parts:

1. Simulated geometries and general flow results.
2. Numerical tracer experiments: tracer plume passage and interpretation of the breakthrough curves - interpretation of the BTC from the laboratory experiments.
3. Interpretation of wall shear stress distributions, these are relevant for particle attachment in a flow form.

It is difficult to give a comprehensive description of a numerical flow simulation containing between eight and twenty variables in a three dimensional domain of 20'000 to 150'000 grid cells within a printed document. First, the simulated geometries are shown in a perspective view, together with some more detailed technical explanations for some simulations, and necessary simulation parameters. The steady-state or quasi-steady state flow solutions are then characterized using the key variables speed and turbulent kinetic energy. Velocity arrows best represent a flow field. However they are not very suitable to represent flows with large velocity variations, because either information in areas with small speed is lost when choosing a low arrow length scale, or arrows will overlap in areas with higher speed when a larger length scale is chosen. While here it is important to recognize simultaneously what happens in fast and slow flow areas, two complementary representations were chosen: streamline pictures and speed isolines. Streamlines give an excellent visualization of the eddy pattern. Isolines of speed make this image more quantitative, and, at the same time their density gives an idea about the shear stress. While there are no really three-dimensional flows among these simulations, plane views will be sufficient to characterize the flow. For long, thin geometries like the channel specimen, a streamline and speed contour representation is not very informative, therefore profiles in x-direction have been chosen for these cases. On the other hand, profiles in a pool might be quite confusing to a reader who is not very familiar with each specimen.

6.1 Description of simulations

While the characteristic dimensions of karst conduits cross sections in nature vary on a continuous scale from about 1 cm to 10 m or more, discharges in a single conduit vary from some ml/s to some m^3/s and observed flow velocities (analyzing scallops) between 0.03 m/s and 1.2 m/s (GOODCHILD 1971, WHITE 1970, WHITE 1976), the present simulations are mostly restricted to one set of these three parameters, i.e. a conduit width of 0.2 m at a discharge of 1.0 l/s, leading to average flow velocities of approximately 0.07 m/s. It seemed a more important objective to compare some different geometries than to study a wide range of cross-sections and discharges. These results should therefore be considered as an example-type of flowforms in a karst conduit system. However, the numerical model is basically suitable to cover the size range of conduits in karst, and this may be the subject of a future

study. Base for the chosen scale is the 1:5 scale laboratory model of some typical flowforms found in 'La Grotte de Milandre', Ajoie, Switzerland.

The numerical treatment of the examined flowforms splits up into two major classes:

- Horizontal structures in the subcritical flow domain are calculated with a rigid lid approximation, and generally a small resolution in z-direction. This applies in first place to galleries (channels) with a small gradient and pools. The same geometries may be used for pipe flow conditions, with the only difference that the upper boundary condition becomes a wall in this case.

- Vertical structures, typically in the supercritical flow domain, are calculated with a two-phase water/air model that allows estimation of the free surface. This approach is intrinsically much more resource-consuming, and therefore only cases with a constant width, allowing a 2D vertical modeling, are treated.

When using a rigid lid approximation, the water depth must be a priori known, in order to assure a correct relation discharge - water depth - inflow velocity. When modeling short pieces of conduit it is convenient to assume a weir outflow condition. This allows to utilize Equation 3.9 to estimate the water depth and inflow velocity for a given discharge.

This numerical approach is based on the assumption from Chapter 2 that topographic structures separated by overfalls or riffles are independent.

6.1.1 Computational effort

The calculation of a steady state solution in a rigid-lid model takes typically 4-12 hours on a Silicon Graphics Indigo workstation with 128 MB RAM. The calculation of a tracer experiment based on a steady-state solution of the velocity field, i.e. no further iteration of the hydrodynamic equations, will take another 4-12 hours for 10'000 time steps of 0.1 s. For the free surface models, the CPU times are a factor 3-4 higher because two sets of variables must be computed, one for water and one for air at each cell. Also, it may be necessary to choose a shorter time step - this reduces the real time that is calculated further.

6.1.2 Simulated geometries, simulation parameters and boundary conditions

Figures 6.1, 6.2, and 6.3 show the relevant geometries in a perspective view.

Channels and confluent

The most basic form is the regular channel, with a free surface or as a pipe. Field data from cave exploration and survey suggest to add a gently ondulating channel, a channel with periodic 90° bends and a channel with irregular extensions (solution pockets). The shapes of the ondulating channel and the channel with solutions pockets have been created with a random number generator. In a branchwork conduit system it is interesting to know the influence of a confluent. The grid size of the channels is 350-500 cells in x, 20-30 in y and 3-4 in z-direction.

Pools and maze

The simplest pool in Fig. 6.2 has a trapezoidal shape. Complexity has been added by deplacing the entrance/exit out of a straight line and deflecting the flow with obstacles. Irregular pools have not been created for two reasons:

- The number of realizations to be considered may be arbitrarily high.
- As will be shown in more detail later in this chapter, the essential feature of a pool is the presence of a flow reversion or stagnant water zone, in exchange with the through flow zone. There has to be a sudden expansion to create this situation, and the detailed shape of the surrounding walls should be of secondary importance here.

The only pool that has a variation in depth is the 'laboratory pool', corresponding to the model built in laboratory. The maze is somewhat in between a channel and a pool, with small eddies developing at many places. The same is true for the angular channel, where an important eddy develops after each bend. The grid size of the pools is around 100 by 100 cells without entry and exit channel, and 3-4 cells in z-direction.

Vertical flowforms

Among the vertical flowforms, it seemed interesting to look at a gently sloped rapid or riffle, with a hydraulic jump, and a waterfall. The pothole is omitted because it is a relatively rare flowform, and it corresponds basically to a vertical solution pocket. The difference between entry and exit water levels is 5 cm for the hydraulic jump on a length of 20 cm, and for the waterfall the fall height is 27.5 cm. The grids for the vertical flow forms contain only one layer of cells in the y-direction, with symmetry boundary conditions at each side, and therefore represent a plane cut of these flowforms. The ramp rapid (hydraulic jump) is on a grid of 200 by 35 cells.

Simulation parameters, initial and boundary conditions

Some physical properties of the fluids, i.e. water and air, have to be defined in the command file. These are the densities $\rho = 1000$ kg/m^3, $\rho_a = 1$ kg/m^3, the respective viscosity $\nu = 1 \cdot 10^{-3}$ kg/ms, $\nu_a = 1.8 \cdot 10^{-5}$ kg/ms and the gravity vector $g_z = 9.81$ m/s^2 for buoyant flow. At the entry, the velocity over the whole section is given as a constant, perpendicular to the flow domain boundary.

6.2 Flow results

The results of the flow simulations, i.e. stationary flow fields for the rigid lid approximation flowforms and quasi-stationary solution for the free surface flowforms are presented next, in order to give the reader an idea about the sometimes complicated flow patterns. By convention, here and in the following, inflow is always from the left except otherwise mentioned.

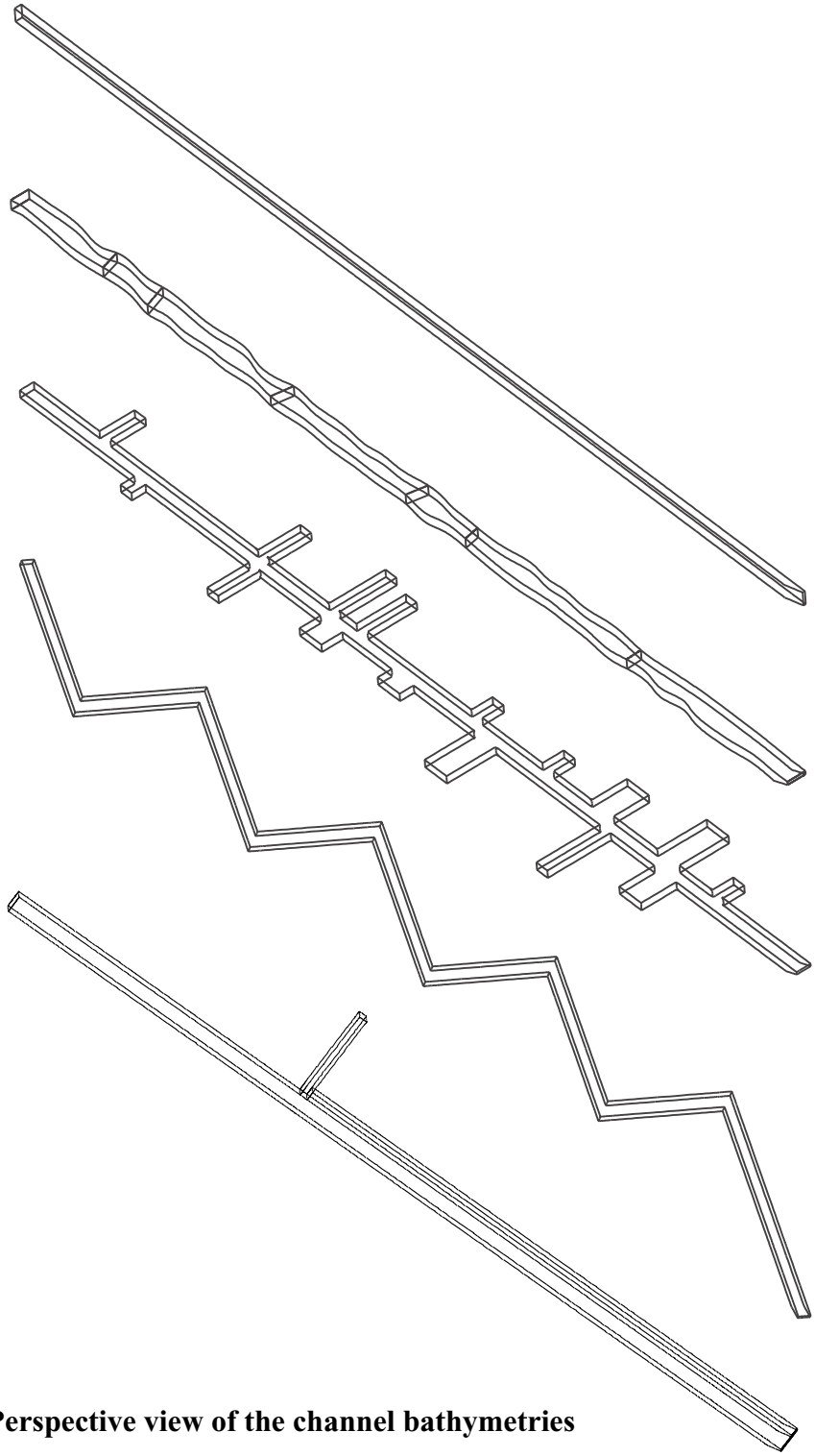

Fig. 6.1 Perspective view of the channel bathymetries

- Regular channel
- Irregular channel
- Channel with pockets
- Angular channel
- Confluent

All examples are a bit longer than 10 m, except the angular channel where each leg is 2 m long

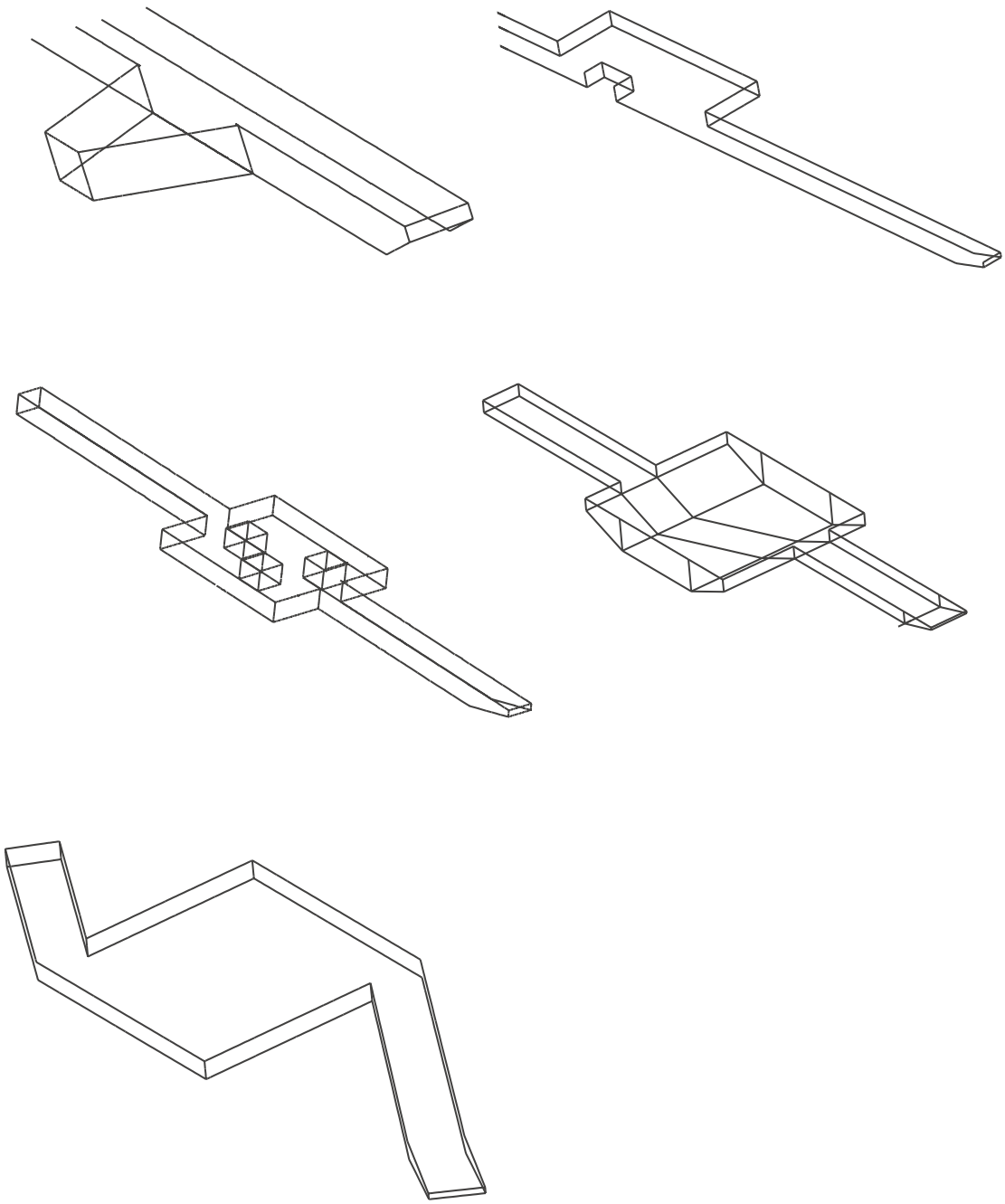

Fig. 6.2 Perspective view of the pool bathymetries

- Trapezoidal pool / Obstacle pool (simulations with central symmetry plane)
- Stones pool / Laboratory pool
- Diagonal pool

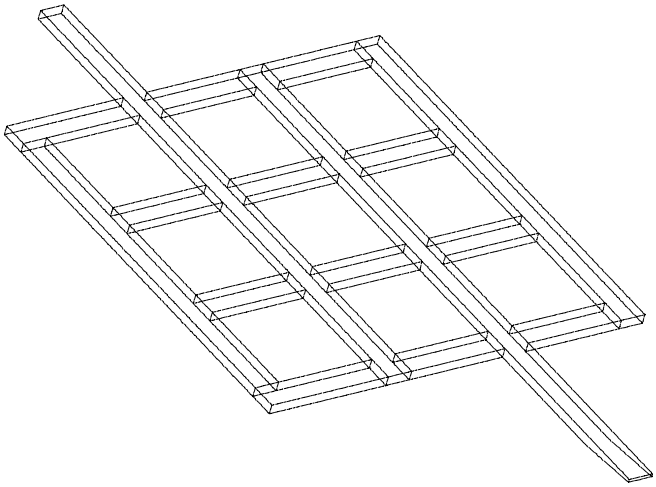

Fig. 6.3 Perspective view of the maze geometry

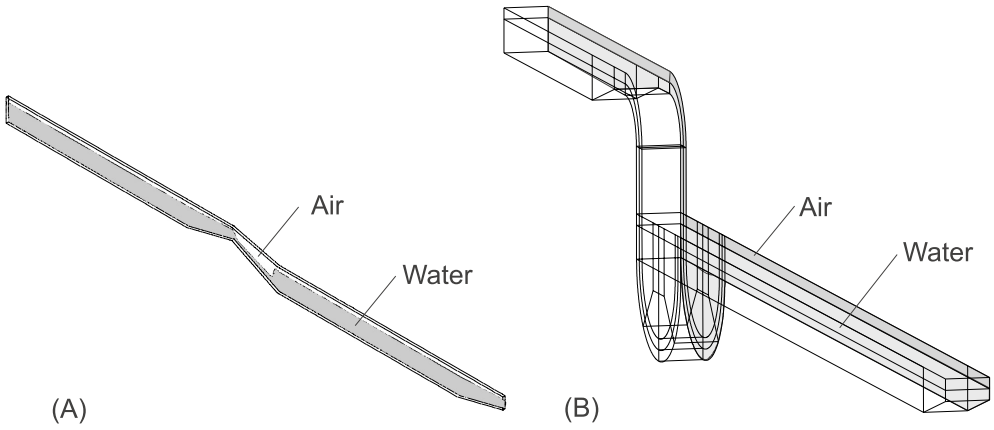

Fig. 6.4 Perspective view of the vertical model bathymetries

(A) Ramp with hydraulic jump
(B) Waterfall

6.2.1 Velocity and turbulence profiles of channels

As mentioned above, for the regular channel, irregular channel and pipe (phreatic channel) streamlines do not deliver much interesting information. Therefore, profiles in x-direction have been plotted for these cases.

Profiles in x-direction

Profiles in x-direction for speed and turbulent kinetic energy are shown in Fig. 6.5 at each layer of cells in depth. The y-coordinate of the profiles is in the center for the regular channel and channel with pockets, while it is following the actual middle of the flow section for the irregular channel.

For the regular channel, both speed and turbulent kinetic energy K take some distance (about 5 - 6 m) to adjust to a constant value. Speed is increasing from bottom to top, while K is larger at the bottom ($6 \cdot 10^{-5}$ m^2/s^2) and decreases towards a third of this at the water surface in the rigid lid model. For the irregular channel and channel with pockets, both variables react quite sensitively to the irregularities of the geometry. The speed increases in the narrow sections of the irregular channel up to twice it's value in the wider sections, while it drops a little close to the pockets in the geometry containing those. The turbulent kinetic energy rises in the narrow sections of the irregular channel, and also in the shear zones close to the pockets. In both geometries this variation of K is much larger close to the bed than close to the water surface. Profiles in x and z-direction show similar distributions.

Hence, a relatively small irregularity of the geometric form may lead to large variations of important flow variables. This may considerably change the transport processes of tracer and particles. It is also an indication that it is necessary to use a non-linear flow model and a turbulence closure to describe these flows adequately.

Detail views of speed in angular channel and confluent

Sharp bends in the flow geometry lead to eddies of intermediate size. This may be observed in the angular channel and confluent, in the detail view of speed contours in Fig. 6.6. The main flow is compressed to about half the channel width.

6.2.2 Flowforms in pools and maze: streamlines and eddies

In the pools, the influence of one large inhomogeneity can be observed rather than the effect of many small inhomogeneities, as it is the case for the channels. The flow through a pool may be conceptually separated into a central flow path, or flow tube, and stagnant water zones which may occupy up to 90% of the volume in some of the geometries (comp Fig. 6.18). This separation can be clearly seen in the streamline pictures. One large eddy develops in the 'diagonal pool', respectively one at each side in the 'trapezoidal' and 'laboratory pool'. The two other pools show smaller eddies behind each obstruction, and slower velocities in the through flow.

Fig. 6.7 shows planar streamline views in a z-plane with z = h/2 for the five types of pool simulated in a horizontal/rigid-lid setup. This view is completed by Fig. 6.8 with speed isolines, for speed between 0 and 0.06 m/s. The main flow path where speed is higher than in zones of stagnant water and flow reversal zones is shaded in gray. The patterns in a maze pool are similar to those in an angular channel and therefore they are not shown separately.

6.2.3 Flow field in vertical/free surface flowforms

A ramp, leading to a hydraulic jump at its lower end, has been simulated as an example-type of a vertical flowform with free surface. Fig. 6.10 a shows the flow field in the hydraulic jump. Where the jet meets the water body below there is a complete reversion of the flow. Supercritical flows are physically transient and no steady state solution exists. A periodically breaking wave can be observed in this example, as shown in the time series for t = 0 - 3 s after start of the simulation in Fig. 6.11. There is complete flow reversion in the volume below (see velocity arrows in Fig. 6.10 a), with backwards flow on the surface. A speed profile

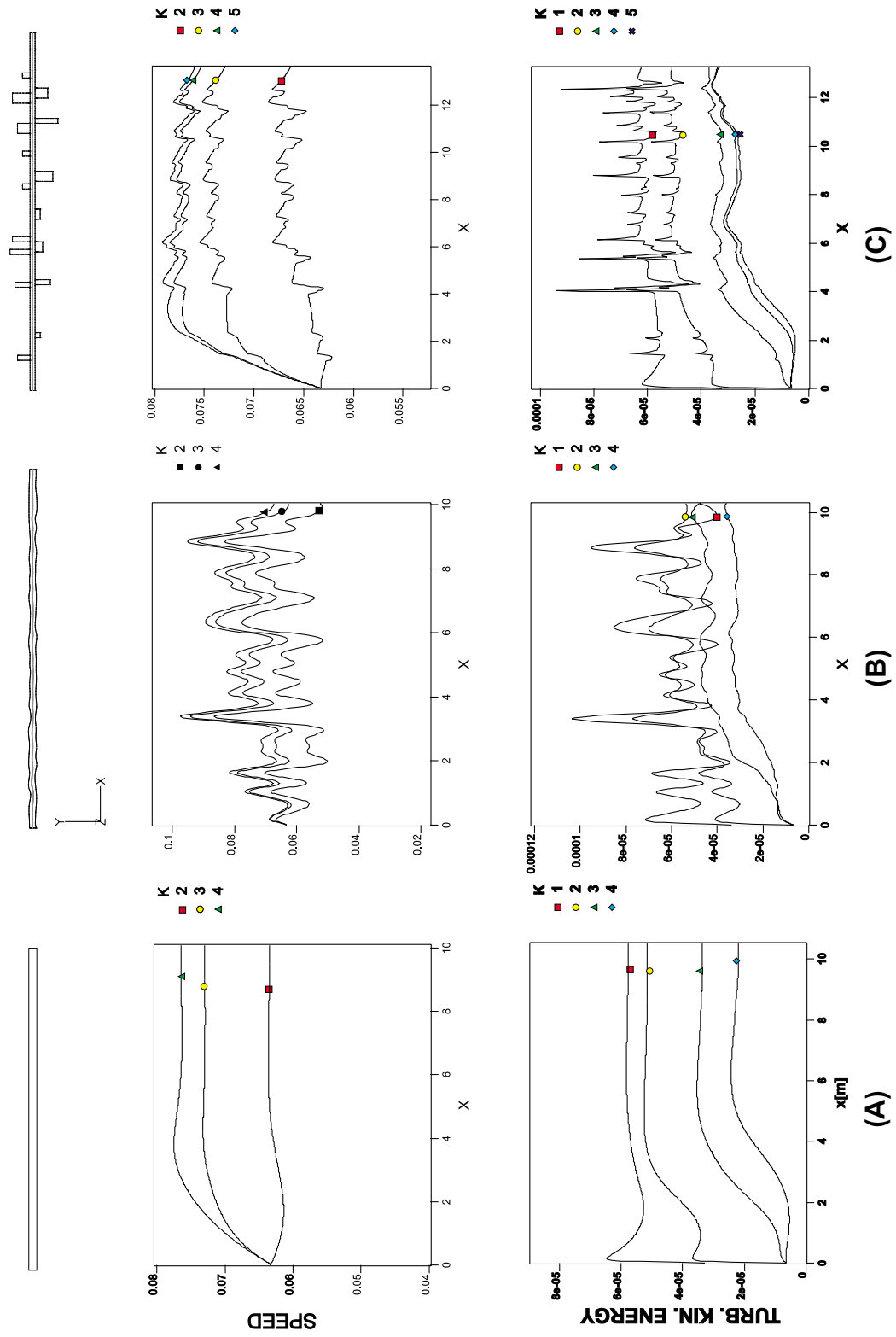

Fig. 6.5 **Speed and turbulent kinetic energy profiles for**

(A) Regular channel
(B) Irregular channel
(C) Pocket channel

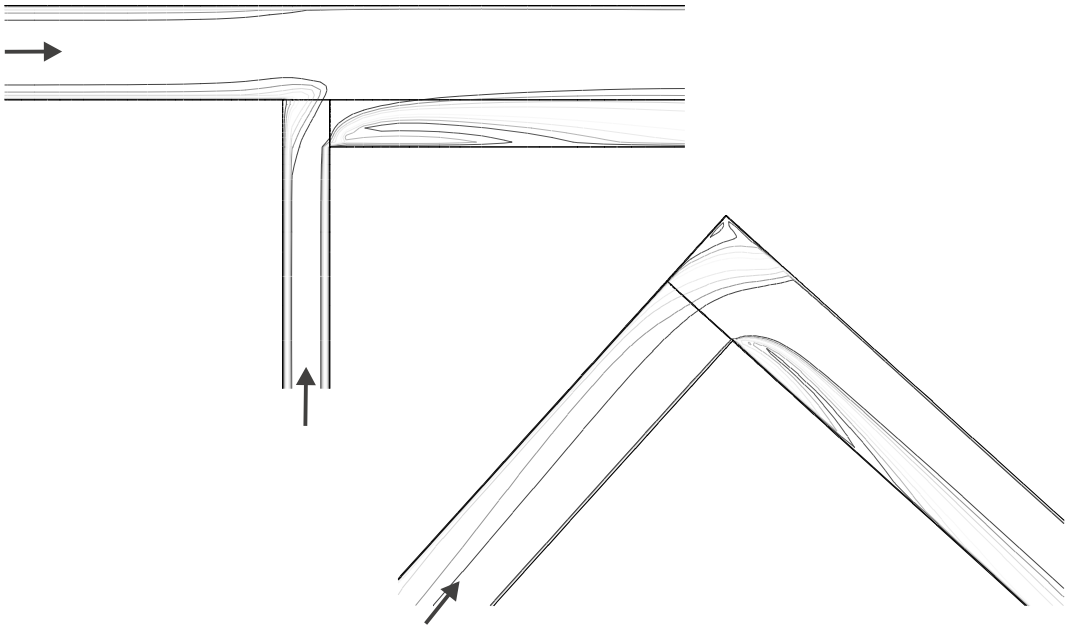

Fig. 6.6 Speed in 'confluent' and 'angular channel' (10 isolines between 0 and 0.06 m/s)

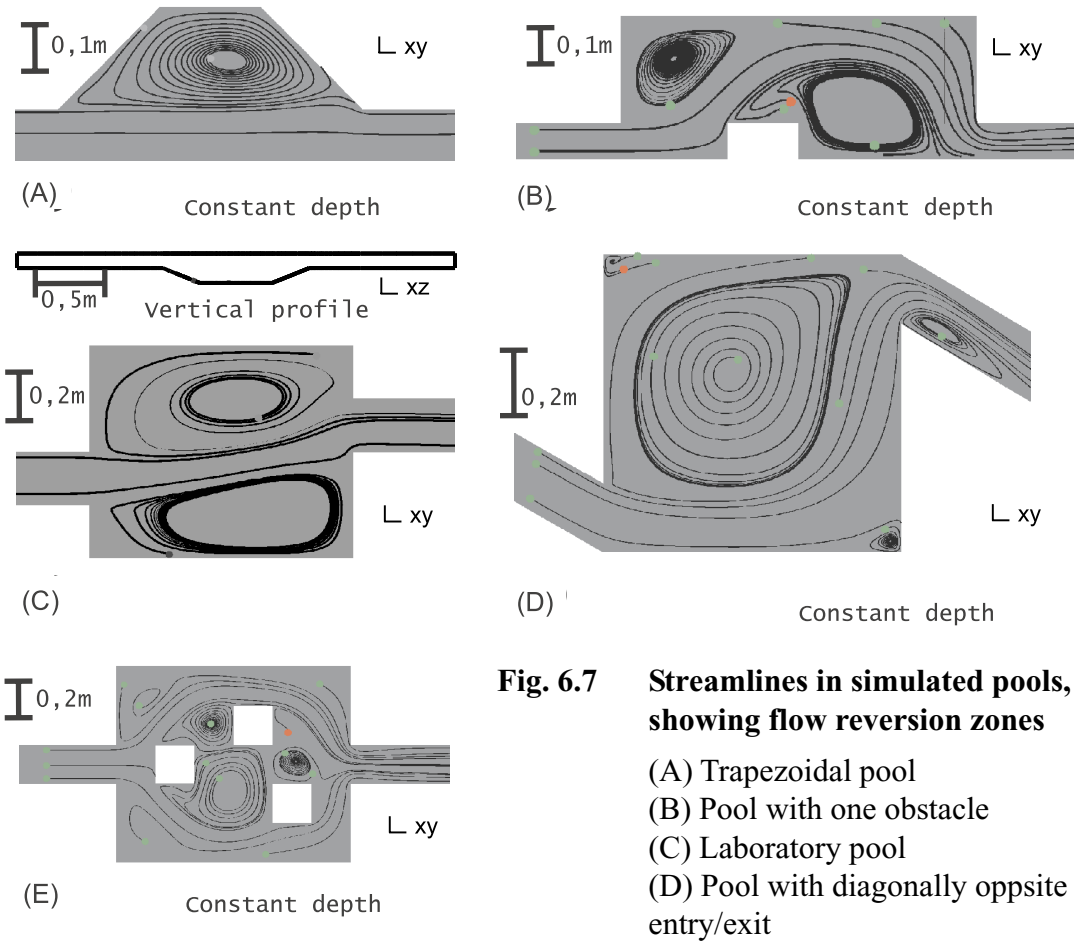

Fig. 6.7 Streamlines in simulated pools, showing flow reversion zones

(A) Trapezoidal pool
(B) Pool with one obstacle
(C) Laboratory pool
(D) Pool with diagonally oppsite entry/exit
(E) Pool with three obstacles (stones)

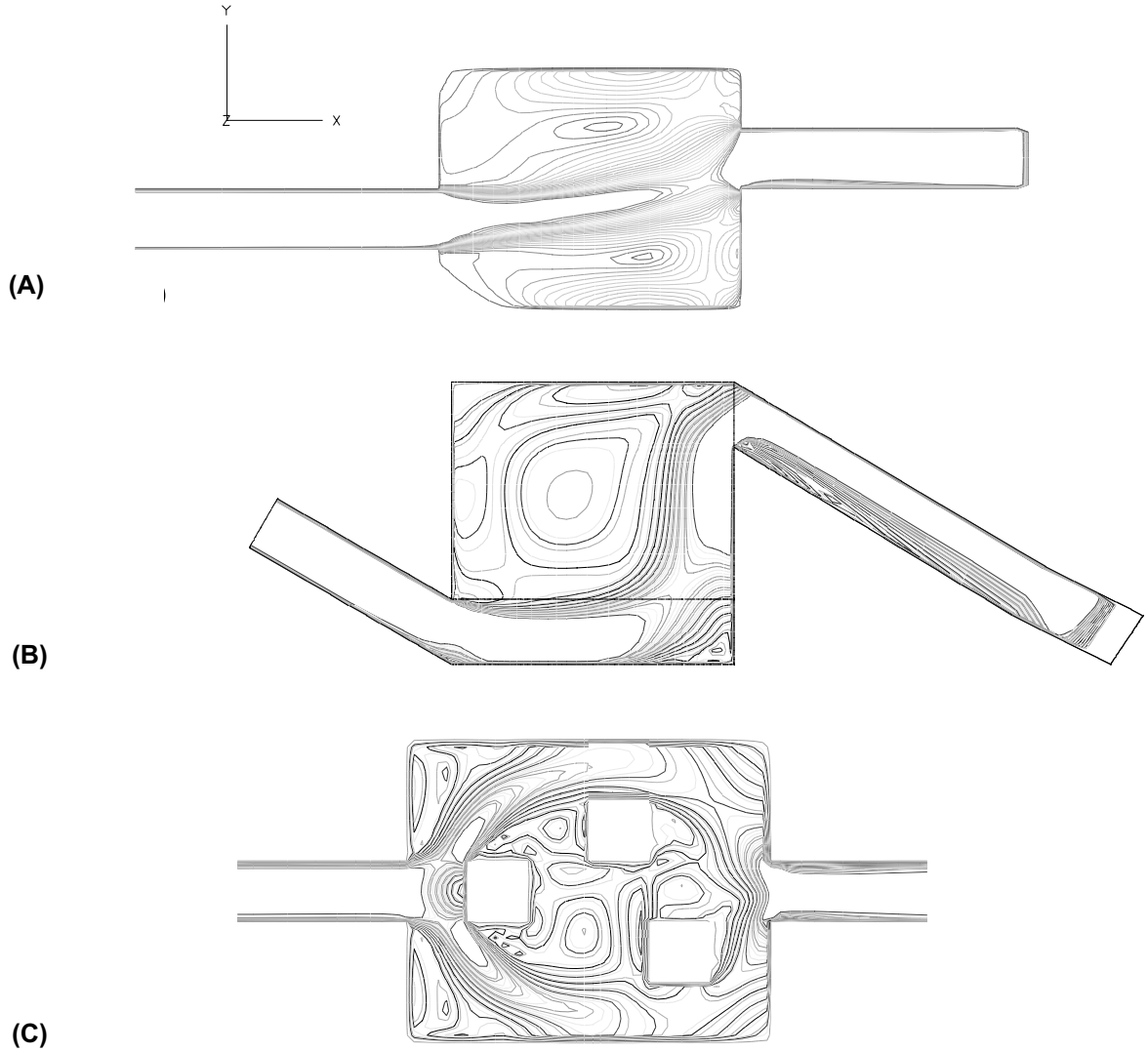

Fig. 6.8 **Speed distribution in pools** (20 isolines of speed between 0 and 0.06 m/s)

(A) Laboratory pool
(B) Pool with diagonally opposite entry/exit
(C) Pool with three obstacles (stones)

following the bed contour shows velocities of more than 1 m/s on the ramp, and the turbulent kinetic energy K in the drop area is up to 0.03 m^2/s^2, this is 300 times the peak values in the channels. Consequently, the characteristic variables in a supercritical flow regime are two orders of magnitude from tranquil flow forms at the same geometric scale.

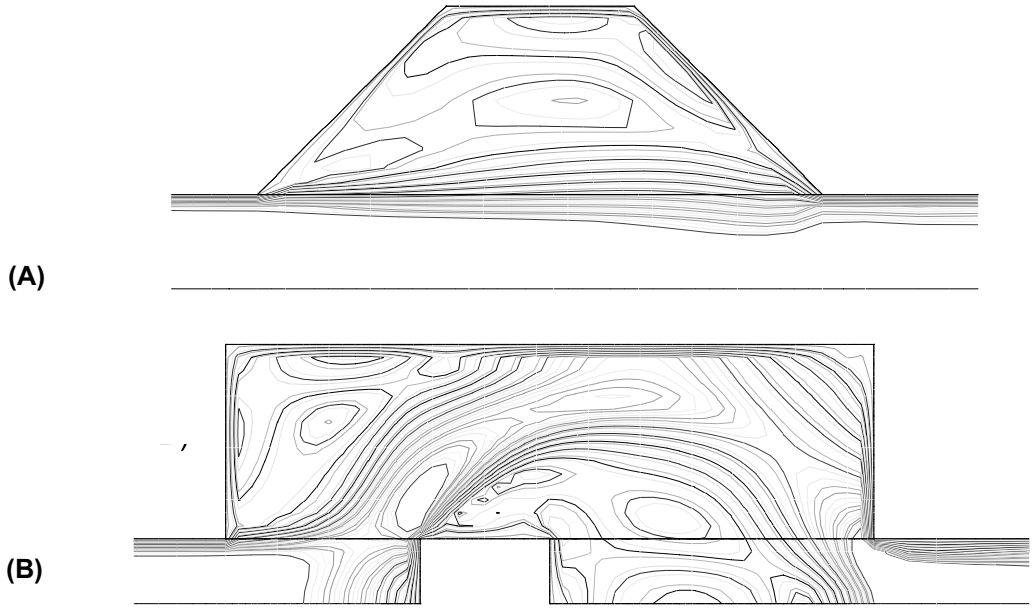

Fig. 6.9 **Speed distribution in pools** (20 isolines of speed between 0 and 0.06 m/s)

(A) Trapezoidal pool
(B) Pool with one obstacle

Note: the geometries in this figure have been simulated assuming a central symmetry plane. Therefore the graphs display only one side of the symmetric structure

6.2.4 Areas of slow flow in horizontal structures

The size of the areas where $s \leq \frac{2}{3} u_{in}$ has been estimated for some flow forms. These areas shall be considered as regions of slow or stagnant flow, and later in this chapter it will be shown that they can be related to the amount of tailing observed in these flowforms.

6.2.5 Discussion of the flow solutions

Flow solutions within the chosen geometries could be found for all cases. The most important secondary currents, like large and medium size eddies in pools and channels can be identified. Velocity profiles in channels show important variation of speed and turbulent kinetic energy K in a central profile due to inhomogeneity of the border geometry. Flow reversion zones are found as expected from field observation, and in all but the simplest cases a region of through flow or a main current can be clearly distinguished from stagnant water zones. However the resolution is restricted to one or two orders of magnitude of eddies. Vortices in the shear zone between eddy and current cannot be observed in the available resolution. However, their influence on transport processes is approximated in the numerical model, as the diffusion coefficient is coupled to the turbulence closure. The area of slow flow varies between 5-15% for the channels, where it is due mainly to slow flow on the borders and up to 90% for the pools, with eddies large compared to the dimension of through flow. The values of K on the flow domain boundary allow to estimate the areas where particles of a certain size will be

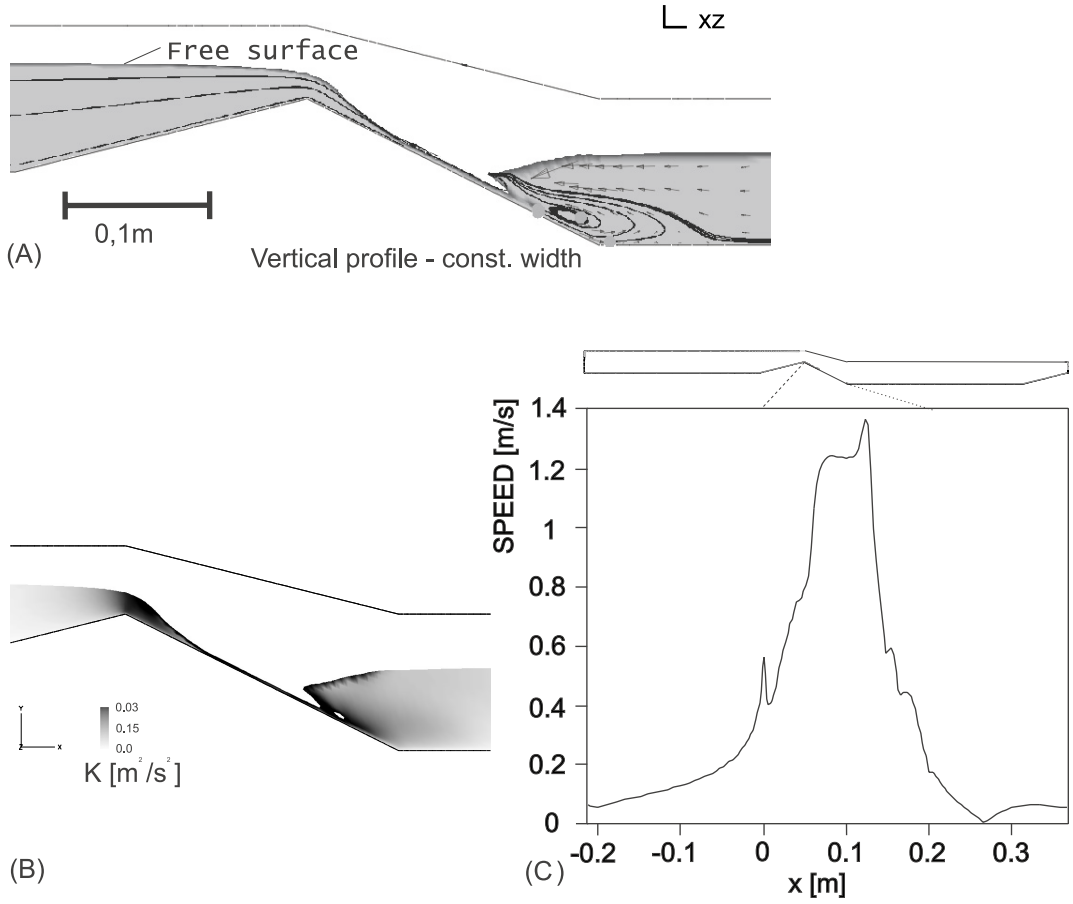

Fig. 6.10 Numerical simulation of flow over a hydraulic jump

(A) The gray area corresponds to the volume occupied by the water. There is a small flow reversion inside the wave. The wave is periodically breaking and therefore a transient simulation has to be done for a tracer experiment
(B) Turbulent kinetic energy K on the ramp: the values are about two orders of magnitude larger than in tranquil flow
(C) Speed along a profile close to the floor

able to attach. Areas of high K are often not identical to high flow speed - they are more likely to be found behind edges and obstacles, in the shear zone between eddies and through-flow.

Two vertical flow forms, a riffle with hydraulic jump and a waterfall were simulated. The values of speed and turbulent kinetic energy are found to be two orders of magnitude lager in this kind of supercritical flow than in comparable tranquil flow.

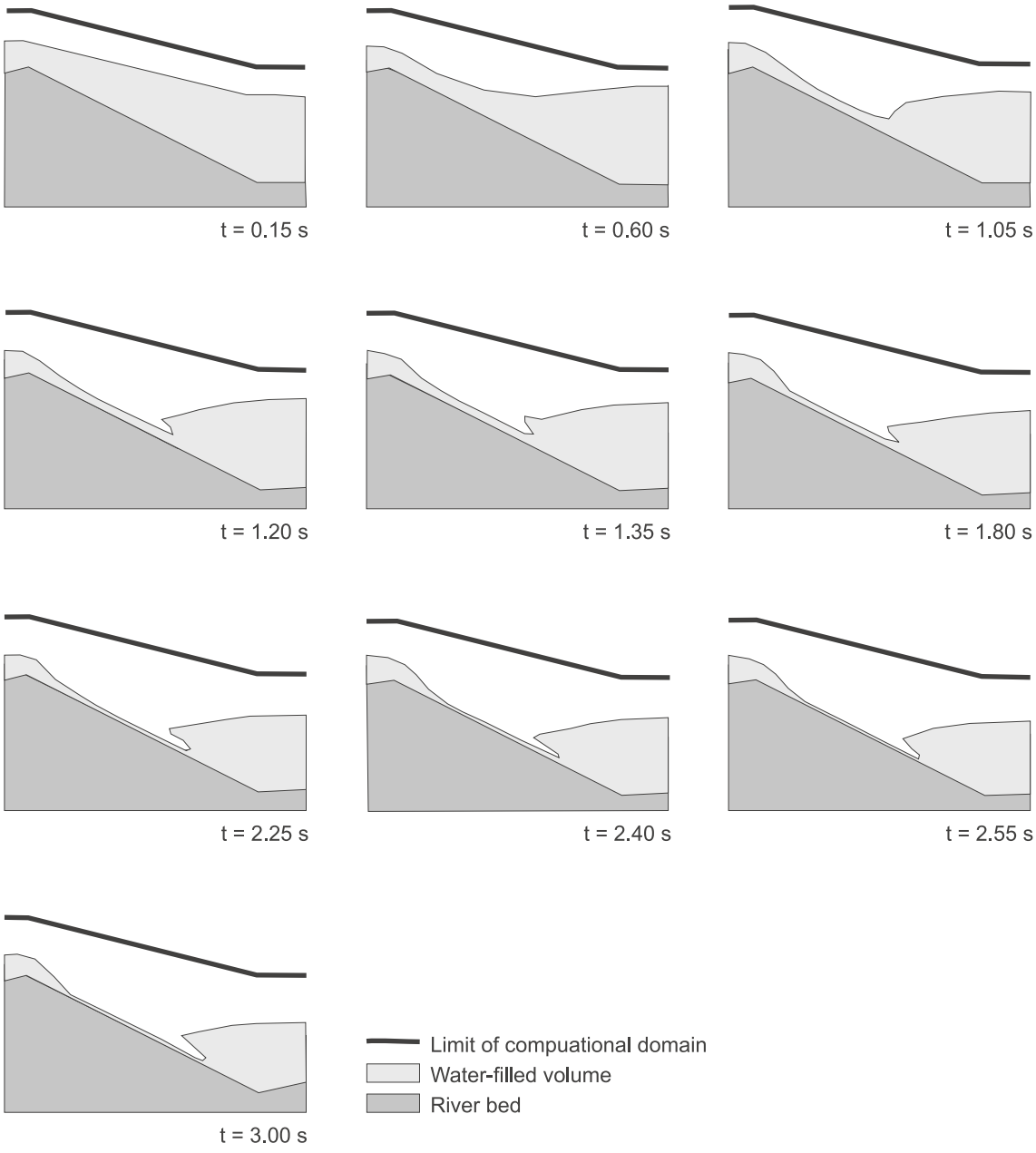

Fig. 6.11 Free surface in hydraulic jump: evolution of the free surface in the time interval t = 0 - 3 s after start of the simulation

6.3 Numerical tracer experiments

Numerical tracer tests, i.e. passage of a tracer plume through a geometry in a numerical simulation, have been done based on the flow solutions described above. Tracer is injected in form of a scalar concentration. This is called a user scalar in CFX and its transport is described by the advection-diffusion equation in three dimensions. In all cases, tracer was injected over the whole inlet surface, the initial tracer concentration was chosen to be unity. The Courant

criterion has to be respected when calculating these numerical tracer experiments. It gives a minimum time step depending on grid size and flow speed.

$$\Delta t \leq \frac{\Delta x}{s} \tag{6.1}$$

The time step may be chosen to 0.1 s on the present velocities and mesh size. The runs included 10'000 time steps, which is the maximum allowed on a single run in CFX. Using the 'restart' option in CFX it is possible to do overall longer runs, but since in nearly all simulations more than 99% of the tracer could be recovered in a single run this was not necessary.

Tracer was injected during 2 s or 20 time steps usually. For the rigid lid simulations with only one fluid phase the tracer transport may be calculated on a stationary solution without further iterations of the hydrodynamic equations. This saves a large amount of computing time. For the free surface simulations this is not possible because there is per definition no stationary state in a multiphase model simulation.

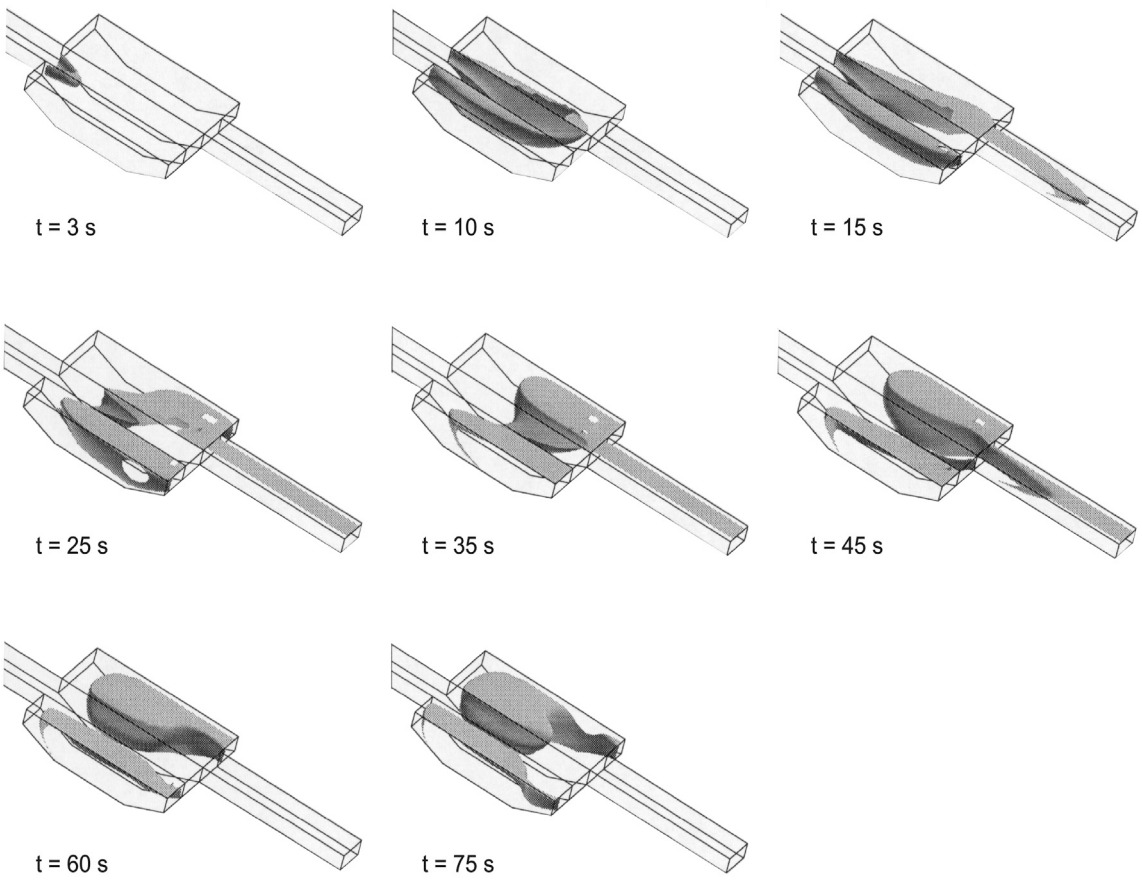

Fig. 6.12 Numerical simulation of tracer plume passage in the laboratory pool
(The plume shape is visualized with an isosurface at C = 0.005)

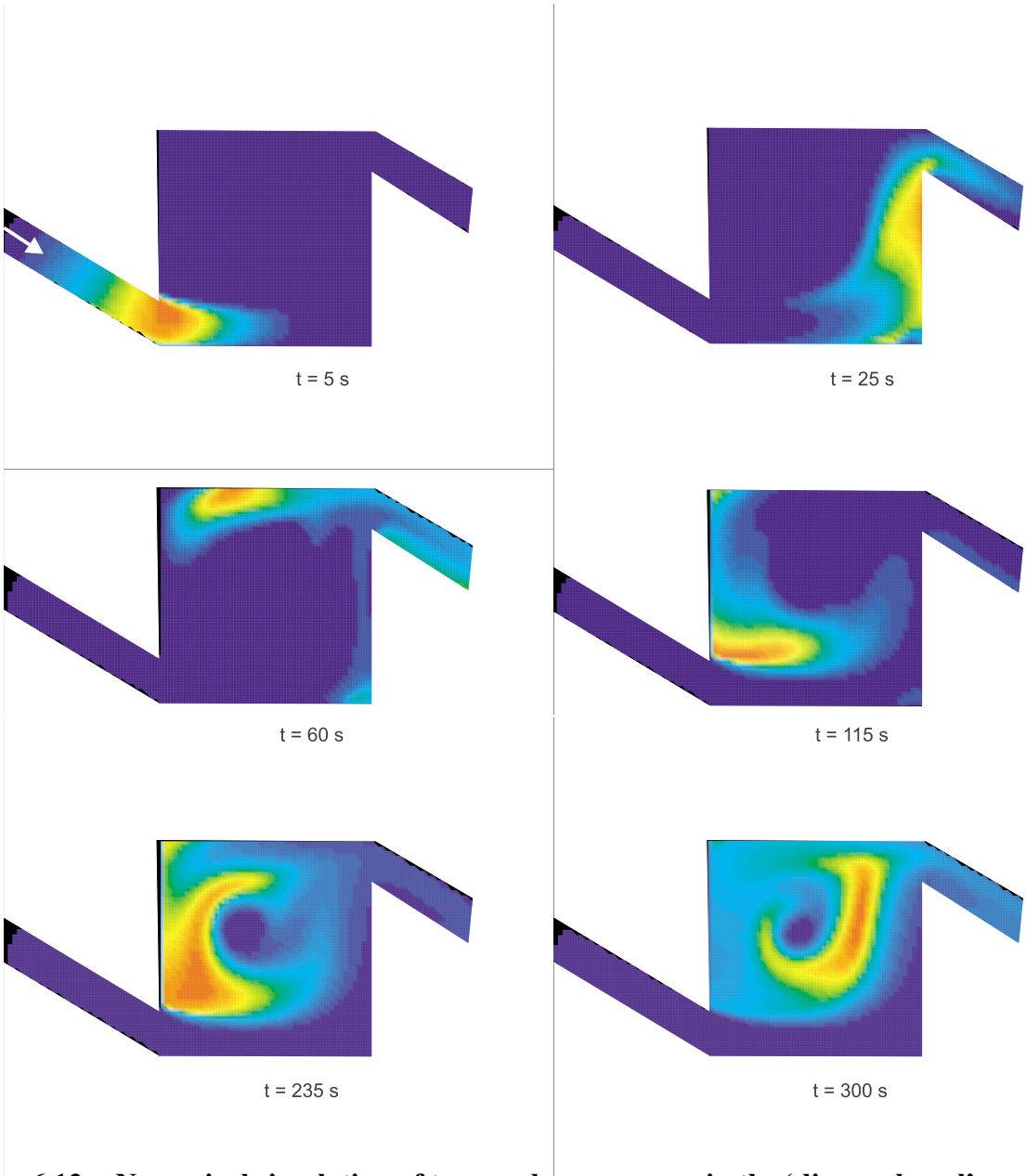

Fig. 6.13 Numerical simulation of tracer plume passage in the 'diagonal pool'. The color scale represents the tracer concentration. Red corresponds to the maximal concentration in the geometry at the actual time step

6.3.1 Time series

The best way to understand the mechanism of tracer retarding due to geometry inhomogeneity is to look at a time series of tracer plume passage. Therefore animations of this in the 'laboratory pool' and 'diagonal pool' are shown here. Fig. 6.12 shows, in a perspective view, the passage of a tracer plume in a numerical simulation of the laboratory pool. The plume comes in through the central stream tube and spreads out laterally while passing through the pool (10 s). It divides into three pieces (25 s). The middle part passes right through, followed by a plume of clear water (45 s). The portion of tracer caught in the recirculation zones is transported back towards the entry, where it migrates slowly back into the main stream tube.

The time series for the 'diagonal pool' is shown in a plane view in Fig. 6.13. The color scale is adapted to correspond to the maximum tracer concentration at the actual time step. Again, the tracer plume is divided into a part that passes right through and a part that stays in the

eddy, from where it disperses slowly back into the main current. The dispersion of the plume inside the only one large eddy while rotating in it can be clearly seen. The corresponding breakthrough curve is shown in Fig. 6.16.

6.3.2 Breakthrough curve interpretation

In the numerical simulations it is very easy to measure a breakthrough curve at any desired number of sampling points. When a sufficient number of time steps has been written to file it is even possible, with the visualization platform ZoomIn, to create a posteriori a concentration curve at any sample point. In all cases, breakthrough curves have been written to file during the run on 1 - 9 sampling points close to the exit of the flow domain.

Analysis of the breakthrough curves is done with the approach developed in Chapter 4. It turned out that, while the simulated geometries are quite short, it is essential to sample at more than one point, in order to obtain a correct result.

Flowtube - or a channel with no walls

To verify the validity of this fitting approach, a special case was simulated: flow in a channel with the same geometry as the 'regular channel', but with a symmetry boundary condition on all sides. Physically, this corresponds to a flowtube, cut from a homogeneous flow with infinite cross section, or a channel with no walls. For this example, the fit wit Eqn. 4.7 is perfect (see Fig. 6.14).

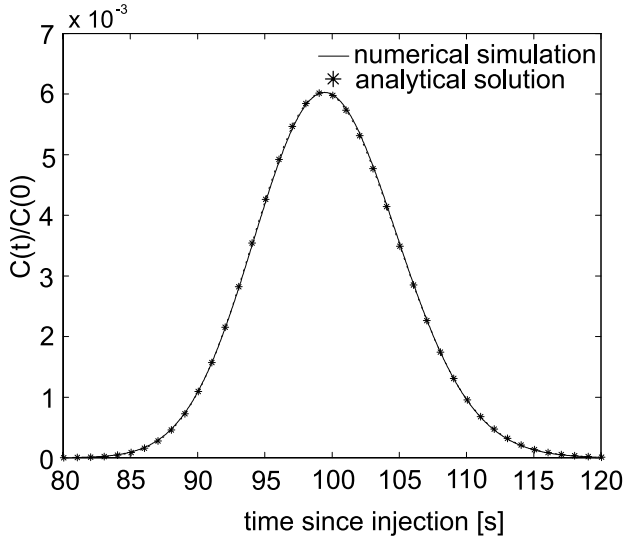

Breakthrough curves in channels

Fig. 6.15 shows the breakthrough curves in the six types of channel and the fitted analytical solutions. The peak arrival times are quite similar: the pipe is 2.8 s or 2% slower than the regular channel (additional ceiling friction), while the peak in the angular and irregular channel arrives 2.6 s (2.4 s) earlier, due to narrower cross section and therefore higher velocities of the main flow in these cases. There is no difference in the peak arrival time between the 'regular channel' and the 'channel with pockets', but the peak concentration in the latter is 39% reduced; this mass will reappear in the tailing.

Fig. 6.14 Breakthrough curve of a 10 m flowtube (line within a homogeneous flow domain of infinite cross-section) simulated with CFX compared to the analytical solution (Eqn. 4.7) with L = 10 m, u_{peak} = 0.1005 m/s and D = 0.001426 m²/s

Table 6.1 Breakthrough curve parameters for channels and pipe

Channel	L [m]	t_{peak} [s]	C_{peak}	D [m^2/s]	R [%]	Recovery [%]
Regular	10	154.7	0.0517	0.00256	10.8	100.0
Irregular	10	152.3	0.0517	0.00281	8.6	100.0
Angular	10	152.1	0.0315	0.00612	18.0	100.0
Pipe	10	157.5	0.0466	0.00297	11.1	100.0
With pockets	10	154.7	0.0378	0.00281	15.3	80.7
Confluent	10	146.3	0.0282	0.00369	17.4	69.0

In the ‘confluent’ BTC the velocity of the peak seems quite slow; this may be due to the large differences in arrival time between the left and right side of this geometry. That may also be the reason for the low recovery rate here.

Dispersion of the main peak is smallest in the ‘regular channel’, followed by the ‘irregular’ and ‘pocket channel’ (9% more). It is still larger in the pipe, again due to additional turbulence from the ceiling. In the ‘angular channel’, D is more than twice as large as in the ‘regular channel’.

The shape of the tail is similar for the ‘regular’, the ‘irregular channel and the pipe: it is later than the falling limb of the analytical solution, but mostly parallel to it, and falls to zero shortly after the latter. The tail of the ‘angular channel’ falls noticeably slower than the analytical solution and lasts about 25 s longer. Meanwhile, the ‘channel with solution pockets’ shows a quite different behavior: the tail follows the analytical solution, but then stays constantly at about 2% of the peak value. This is to the number of small, but non-negligible reservoirs. Also, the ‘channel with solution pockets’ is, besides the maze, for which the same arguments may be true, the only geometry with a non-vanishing tail after 10’000 time steps.

Breakthrough curves in pools

All breakthrough curves from numerical tracer experiments in pools are shown in Fig. 6.16, together with the fitted analytical solutions. Table 6.2 lists the effective distance between injection and sampling point, the time of the maximum, the resulting dispersion/length, D* and the Tailing in percent of the fitted analytical curve. Dispersion has been scaled with length here because the distance between injection and sampling point varies more than a factor two between the geometries. The distance between injection and sampling point has been measured following a streamline connecting the two points. The recovery is also listed.

The peak velocities correspond to the average velocity in the ‘laboratory pool’ and ‘trapezoidal pool’, while they are considerably reduced in the pool geometries with obstructions. The ‘diagonal pool’ shows a strongly increased peak velocity. Meanwhile, this may be due to an additional eddy that developed in the exit channel of this geometry. The peak concentrations vary considerably, between 15% of the initial concentration for the trapezoidal pool down to 4.5% for the pool with one obstacle. However this is partly due to the different lengths. The dispersion values of the pool btc are scaled to D*=D/L, because the lengths are quite diffe-

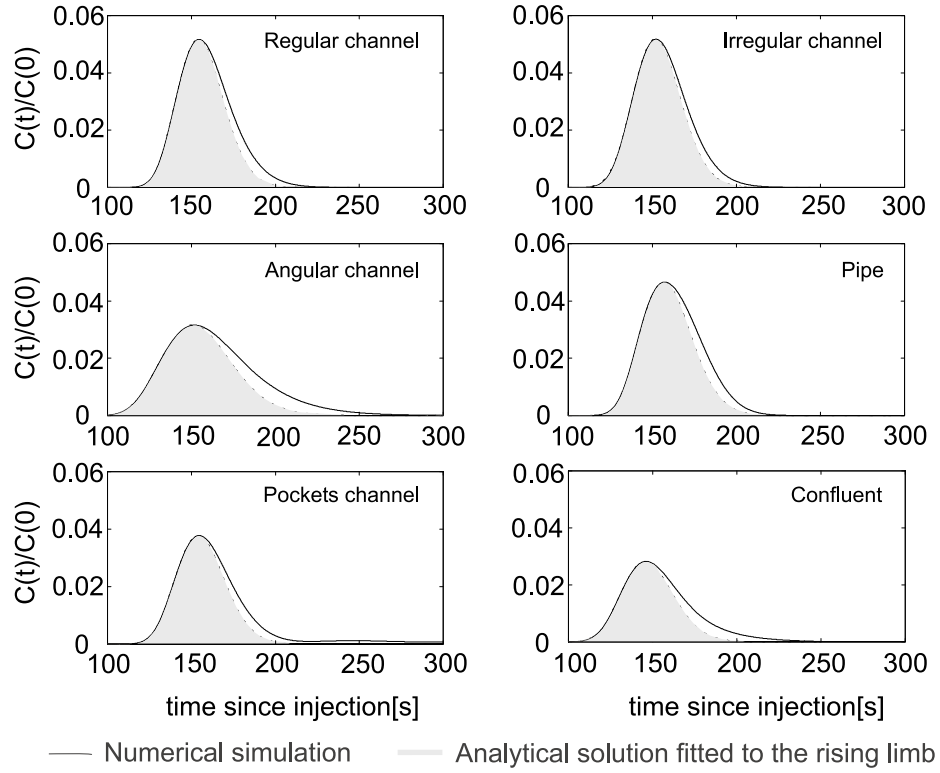

Fig. 6.15 Breakthrough curves of channel and pipe geometries simulated with CFX-FLOW3D compared to the analytical solution

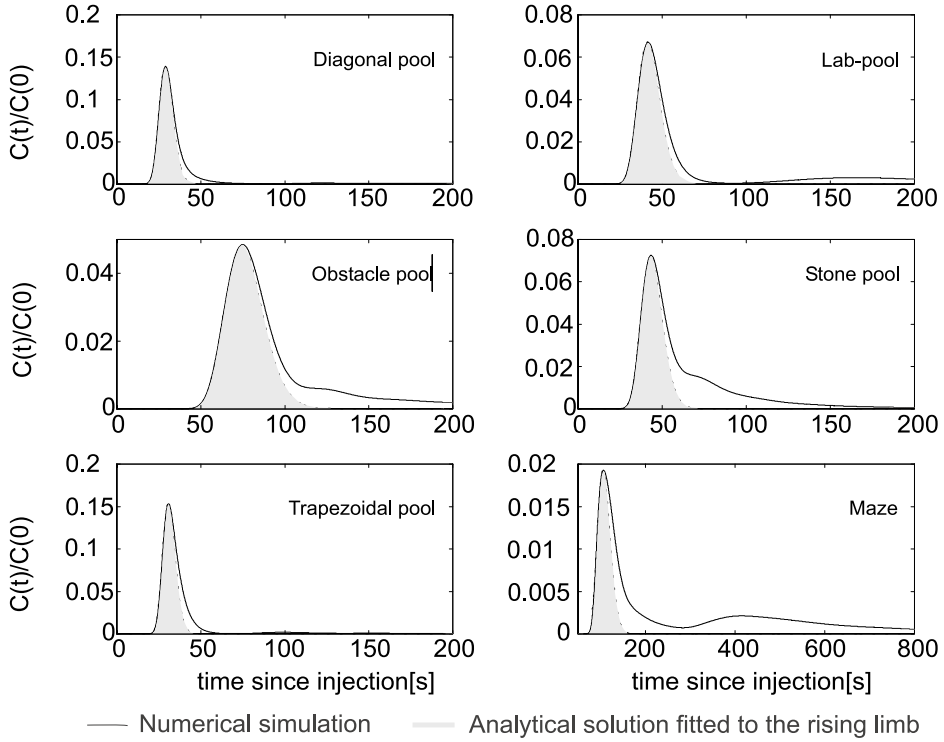

Fig. 6.16 Breakthrough curves of the five pool geometries and the maze simulated with CFX-FLOW3D compared to the analytical solution

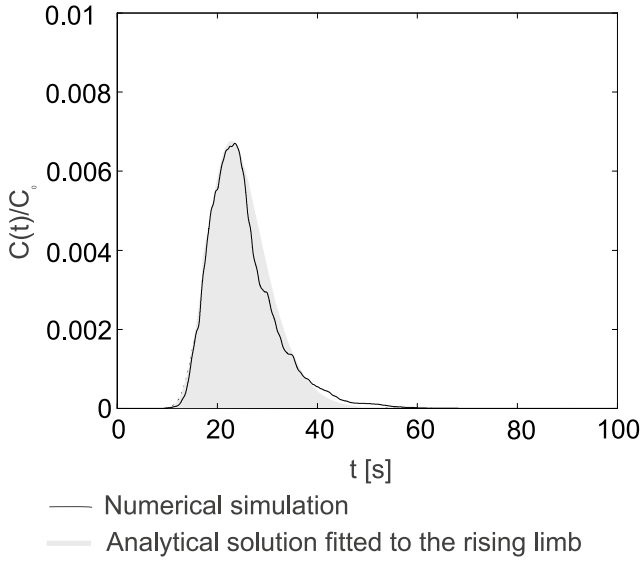

Fig 6.17 Breakthrough curve of the ramp with hydraulic jump simulated with CFX-FLOW3D compared to the analytical solution

rent. Generally dispersion increases with peak velocity, except for the 'pool with stones' and the maze, where the existence of two different flow paths increases the dispersion. The curves of the five pools show a tailing between 28% and 44%. The tails of the pools with obstruction have a distinct shoulder on the falling limb at 20% of the peak height and roughly the same width as the principal peak. The tail in the BTC of the diagonal and trapezoidal pool is quite short, while in the laboratory pool it falls to zero and starts to rise again at 2.5 times t_{peak}. The maze has a constant tail, similar to the 'channel with pockets', and a second peak at t = 400 s.

Table 6.2 Breakthrough curve parameters for pools and maze

Pool	*L* [*m*]	t_{peak} [*s*]	C_{peak}	*D* [m^2/s]	*R* [%]	Recovery [%]
Diagonal	3.42	29.1	0.118	0.001175	22.2	99.8
Laboratory	2.62	41.8	0.063	0.000770	44.6	99.2
Obstacle	4	75.0	0.053	0.000599	31.7	100.0
Stone	2.1	43.5	0.048	0.000491	43.6	100.0
Trapezoidal	2.1	30.9	0.068	0.000493	28.4	100.0
Maze	5	106.8	0.047	0.000412	23.5	93.6

Breakthrough curve of a hydraulic jump

A numerical tracer test was done with the ramp/hydraulic jump geometry. The distance between injection and sampling point was 1.5 m; the dispersion of the BTC is the same as in an irregular channel after 10 m, i.e. D = 0.00284 m^2/s, while the peak velocity u_{peak} = 0.0638 m/s corresponds to the ones observed in tranquil flow. In contrast to all BTC observed so far this one is not smooth but irregular. Small bumps show every 5 s, and they may be due to the breaking of the wave. The 'tailing' of this BTC is negative (-8.6%), i.e. the falling limb is earlier than the falling limb of the analytical solution fitted to the rising limb. This may be a sign that supercritical flows are able to reduce tailing, but it may also be due to interference

of the input signal length with the flow conditions in this particular case. More numerical tracer tests on supercritical flows are necessary to answer this.

6.3.3 Relation between tailing and eddy size

All breakthrough curves except the flowtube, which is not really a physical example, do expose some lag compared to the falling limb of the analytical solution. For the geometries without significant volumes of stagnant fluid the tail is short, the curve is slightly displaced but parallel to the analytical fit, generally following the exponential decrease of the latter. For the pools the tailing may persist for a long time, showing that a non-negligible part of the tracer plume has been trapped in the stagnant water. The tailing should then be controlled by three parameters: how much of the flow is deviated into the eddy, how large is the eddy, and how intense is it's exchange with the main current by turbulent diffusion. While influence of the first and the third process are difficult to evaluate, a relation between the areas of stagnant water, and the amount of tailing is visible. Fig. 6.18 shows the ratio between the stagnant water volume in a geometry and the observed tailing, and suggests a square relation.

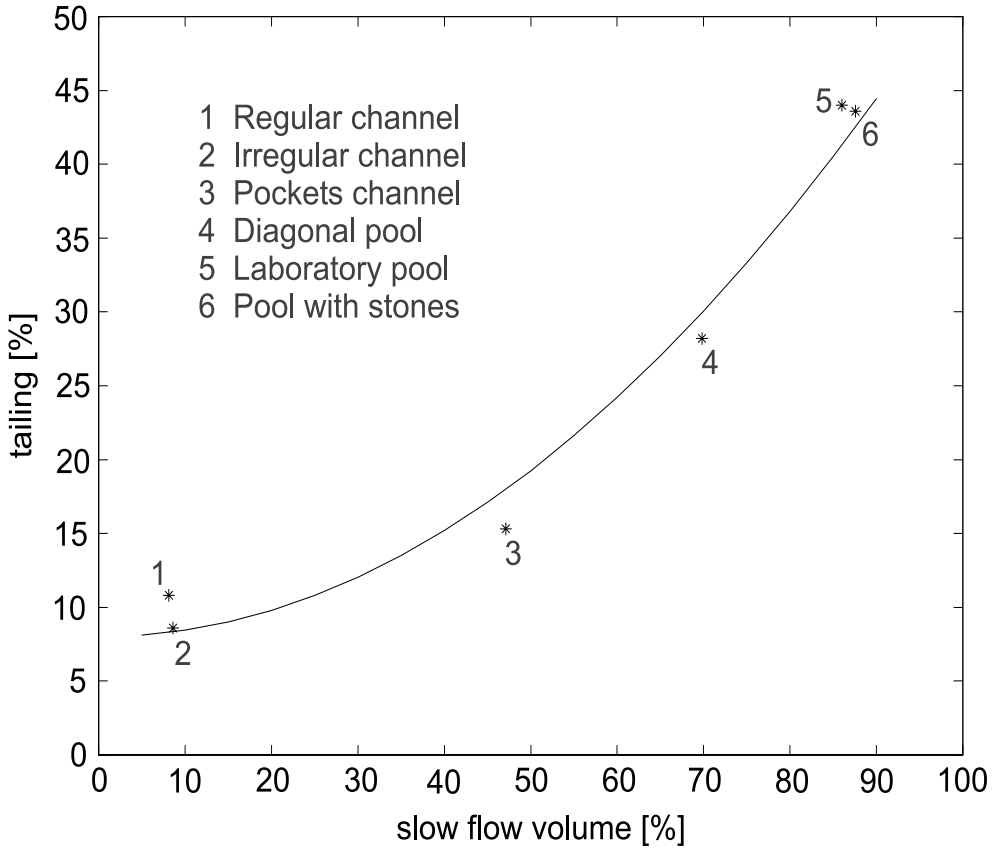

Fig. 6.18 The points in a graph stagnant water volume vs. tailing may be fitted with a polynomial of second order

6.3.4 Laboratory experiments

In the laboratory pool, tracer experiments at different discharges of approximately 0.2 l/s, 1 l/s and 2 l/s were conducted, to provide a verification of the hypothesis of tracer capturing in stagnant water volumes and of the numerical model.

Discharges have been measured by the time needed to fill a graded barrel at the exit. The water level was monitored with a pressure sensor during the experiment and was very stable.

Quantitative reproduction of tailing effect observed in field experiments

The first objective of the experiments with the laboratory pool was to show qualitatively that a tailing is related to the presence of a pool. Therefore an inlay was built (comp. Fig. 6.19) that allows to disconnect the pool volume, leaving a regular channel with two slight bends. The resulting breakthrough curves do show that the tailing is related to the presence of a pool: no tailing was observed in tracer experiments in the channel, but important tailing in the pool. Fig. 6.19 shows the relevant geometries and a comparison of the breakthrough curves.

Analytical fit to the lab model breakthrough curves

Tracer experiments with fluoresceine have been done, for discharges of 0.233 l/s, 0.96 l/s and 1.94 l/s, respectively. The breakthrough curves for totally six tracer experiments at three discharges are shown in Fig. 6.20. Fig. 6.21 shows the smoothed data with a Sauty fit. In all the laboratory breakthrough curves there is a sharp transition between main peak and tail, and then a nearly constant tail. Each experiment was done twice. The data are quite noisy and therefore a smoothing with moving average was applied before fitting with the analytical solution. The dispersion D decreases with increasing discharge as well as the tailing. While there are two realizations for each discharge, comparing them allows some conclusion about the reproducibility. Only the peak arrival time is quite consistent, while the amount of tailing

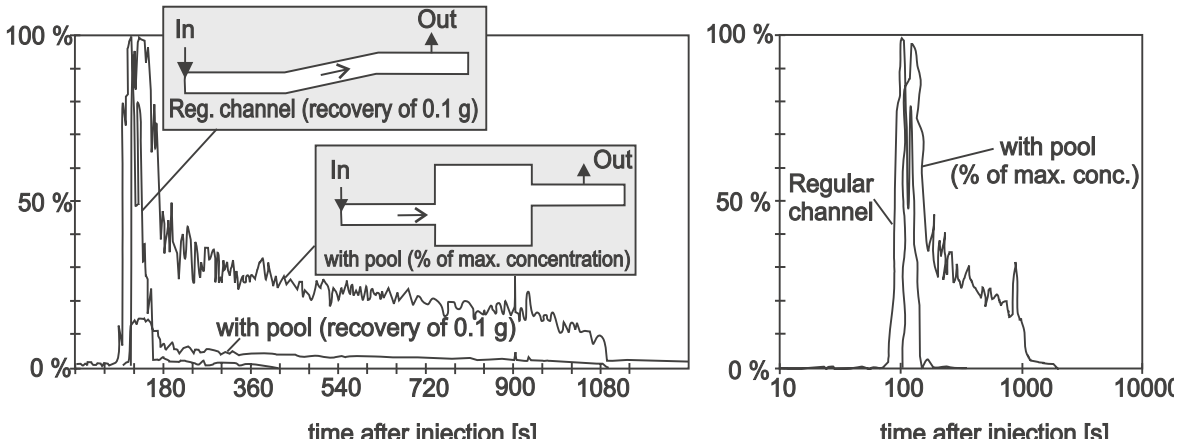

Fig. 6.19 Breakthrough curves of two different laboratory experiments, with and without a pool. The existence of a pool produces retardation of the peak and a tailing. Left: linear time scale; right: logarithmic time scale

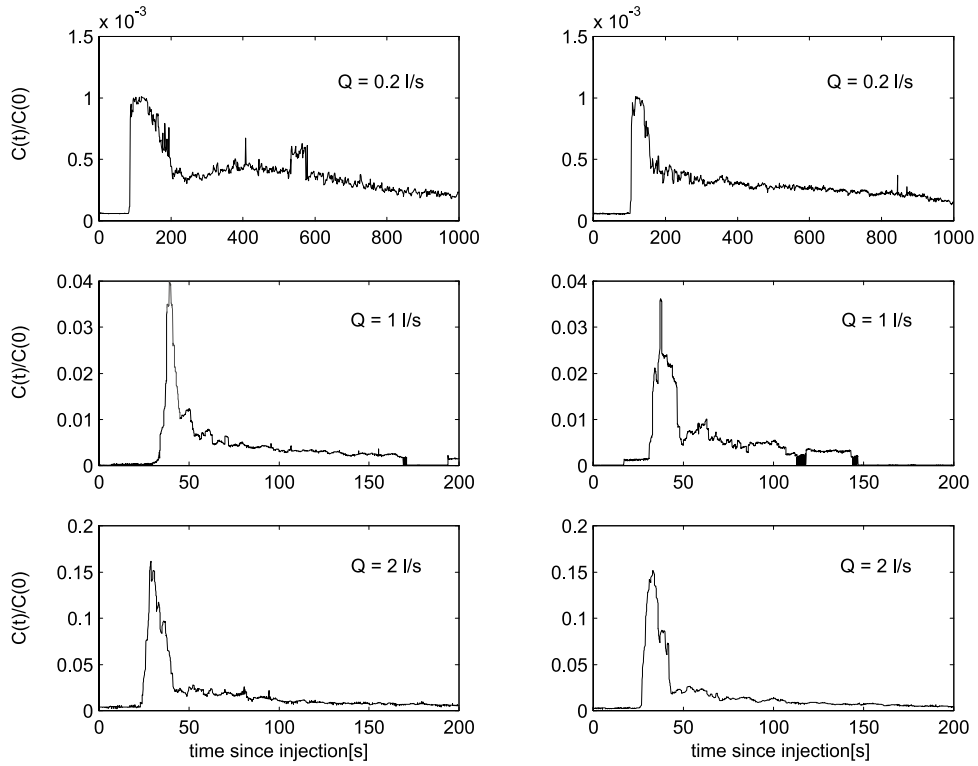

Fig. 6.20 Breakthrough curves of the laboratory experiment. For each discharge (from top to bottom 0.233 l/s, 0.96 l/s and 1.94 l/s) two realizations of a tracer experiment have been conducted

shows differences of 10-20% between two realizations and the dispersivity up to a factor 3 for the experiments of 0.2 l/s and 1 l/s. For the experiments at 2 l/s there is only a difference of about 10%.

As this compared to the results of the numerical model, the peak arrival time is reproduced within less than 10% (37.5 and 39.5 s vs. 41.8 s).

The tailing is 50-70% larger in the experiment and the dispersion differs by at least a factor 4. One possible explication for this is that the turbulent mixing might not be adequately described in the numerical model, in the sense that there is too much diffusion. Therefore dispersion is exaggerated. On the other hand, the curves in the numerical simulation drops back to nearly zero before of the retarded mass. This might be explained by an underestimated mixing. The large variation of D, which is controlled mainly by processes in the part of the plume going right through, may be due to the injection from a one liter container by hand. This may cause different flow conditions in the plume head from one realization to another. Also the appearance of the laboratory experiment breakthrough curves must be compared to field experiments that have been made on a slightly larger scale (15-35 m) in Milandre, and whose tailings do not show a sharp transition and a nearly constant tail as in laboratory. One possible explication for this is that tracer released from the eddy mainly flows along the wall and is not measured in the fluorometer whose inlet is at the center. Rather, the instrument sees immediately the core of a ‘clear water plume’ following the main peak (comp. Fig 6.12). For the same reason, the gradient of the rising limb may be exaggerated. This leads in turn to an underestimate of the dispersion, as the analytical solution is fitted to the rising limb.

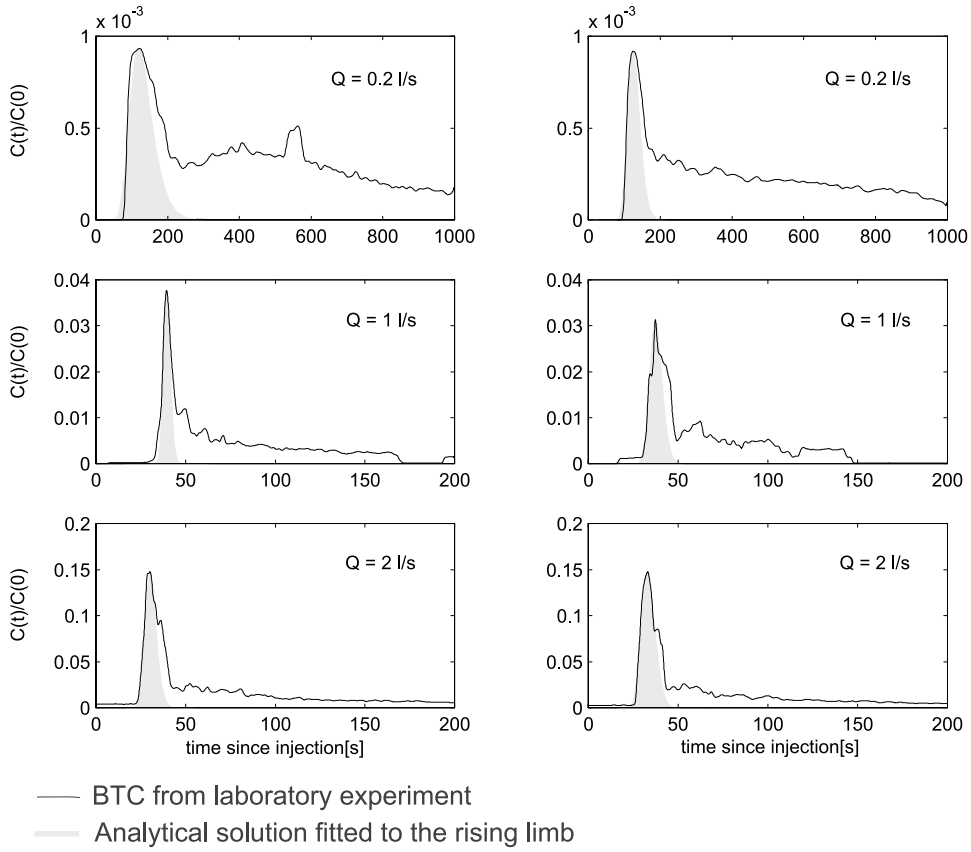

Fig. 6.21 Breakthrough curves of the laboratory experiment: smoothing with moving average and fit with the analytical solution

Consequently, the results of the laboratory model have to be interpreted with care, and should not be considered as a calibration of the numerical model, which however is based on calculation of deterministic physical processes and therefore can not be calibrated like a black box model.

6.4 Shear stress distribution for the deposition model

For particle deposition, the boundary shear stress is the variable of interest. For the particle deposition model, the shear stress on the flow boundary is the interesting variable from the flow solution. The most convenient form to represent this is the variable A*, a cumulative diagram of the shear stress distribution. These „fingerprints“ are shown in Fig. 6.22 for several flowforms. In the regular channel there is a steep rise around $\tau_o=10^{-2}$ m^2/s^2. Only particles from a threshold size will deposit at all in such geometry. The channel with bends has, due to the compression of the flow by the intermediate size eddies, some deposition over for smaller particles. About 40% of the surface of the „channel with pockets“ are in the pockets. This provides a large plateau from attachment of smaller particles.

One large eddy in the diagonal pool has noticeable areas down to very low shear stress while in the pool with roughness elements the shear stress is everywhere larger than 10^3 cm^2/s^2.

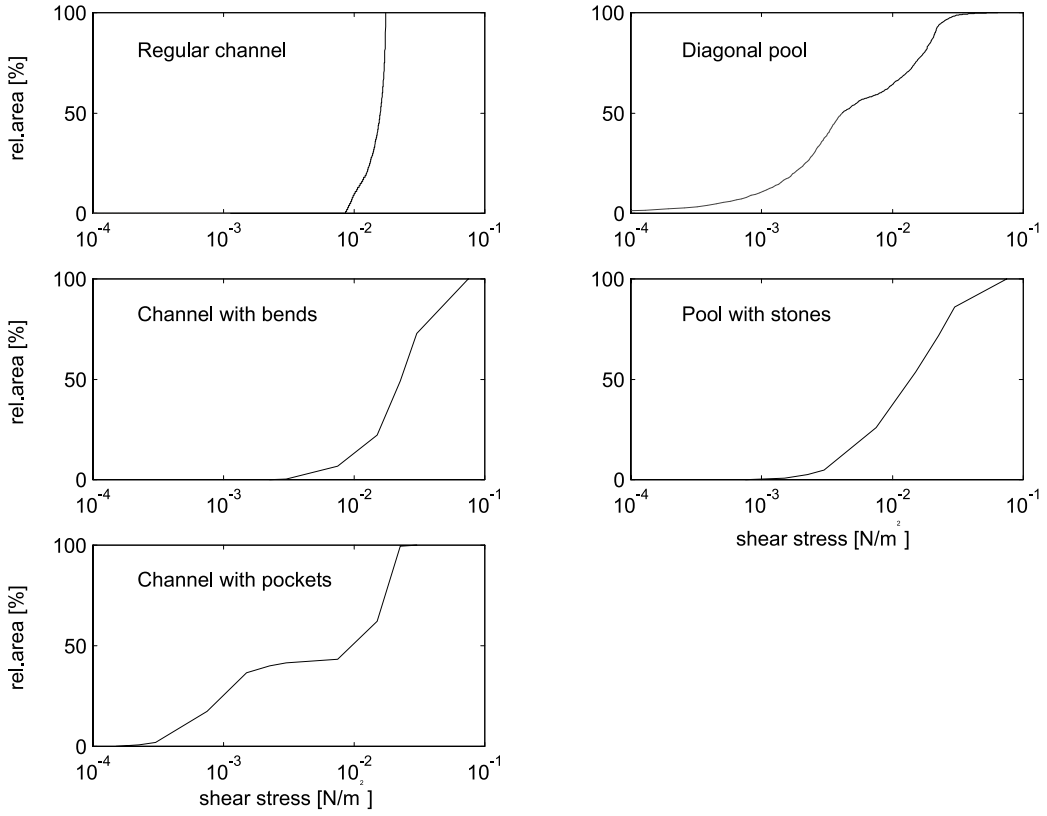

Fig. 6.22 A* graphs for some flow forms

7 Transfer function and conduit scenarios

While the fully deterministic modeling of flow and transport is restricted to a local scale, there are mathematical tools that allow the extension of local results to larger structures. These are introduced in the following, and utilized to create some scenarios. Meanwhile, the use of the transfer function is not restricted to numerical input data: data from local field experiments may also be used as input.

7.1 Transfer function for tracer transport

DOERFLIGER (1996) used transfer functions to characterize karst conduit systems on the scale of a drainage basin.

Here we do the same starting from a microscale: the simulation of breakthrough curves with CFX is clearly restricted to a local scale, i. e. a conduit length of 1-10 m. The transfer function of such a local conduit element may be estimated, and by concatenation of multiple transfer functions, which do not necessarily have to represent the same type of base element, scenarios of conduits and conduit networks over a length scale of some hundred meters and more may be created.

7.1.1 Theoretical basis

The transfer function F(t) is a convolution operator which transforms an input signal I(t) into the system response O(t), with F = deconv(O,I) and O = Conv(I,F). Consider a short piece of conduit and the flow conditions inside as a system, then its response to a rectangular input signal can be expressed with the DUHAMEL integral:

$$0(t) = F(t) * I(t) = \int F(t-\tau)\partial\tau \tag{7.1}$$

For numerical application it is convenient to express the integral in discretized form:

$$F(t_j) \equiv \frac{1}{I_0}\left[\frac{O_j}{\Delta t} - \sum_{k=1}^{j} F_{j-k} O_k\right] \tag{7.2}$$

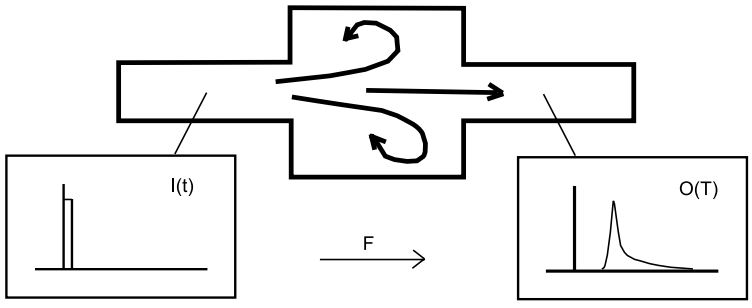

Fig. 7.1
The transfer function is created as a discretized Fourier transform between input signal and response

The method is very sensitive for the creation of the transfer function: the deconvolution will not be convergent for non-monotone input functions. However this is not an important limitation for simulated tracer experiments. Here the input function can be chosen freely, and once F is created its application and concatenation are robust.

7.1.2 Validation on a sequence of three pools

To verify the self-consistence of the method a tracer experiment in three identical, subsequent pools is simulated using a CFD approach and the breakthrough curve at the end of the third pool is compared to a curve calculated from convolution of the transfer function of the first pool. Two different pool forms have been used: a trapezoidal shape and a rectangular pool with an obstacle in the middle. Fig. 7.2 shows the convoluted versus CFD simulated curves at the exit of the third pool. The convolution approach gives a fairly good fit for the trapezoidal lakes. However some differences remain, which are less marked for the rectangle lakes with an obstacle. This different behavior can be explained by looking at the distribution of the turbulent kinetic energy in and after the three lakes. One might say that K values keep the 'memory' of the preceding lake, the tracer might thus not be entirely redistributed between the pools, as assumed in the convolution model. Meanwhile the convolution approach can be used for investigation of large structures.

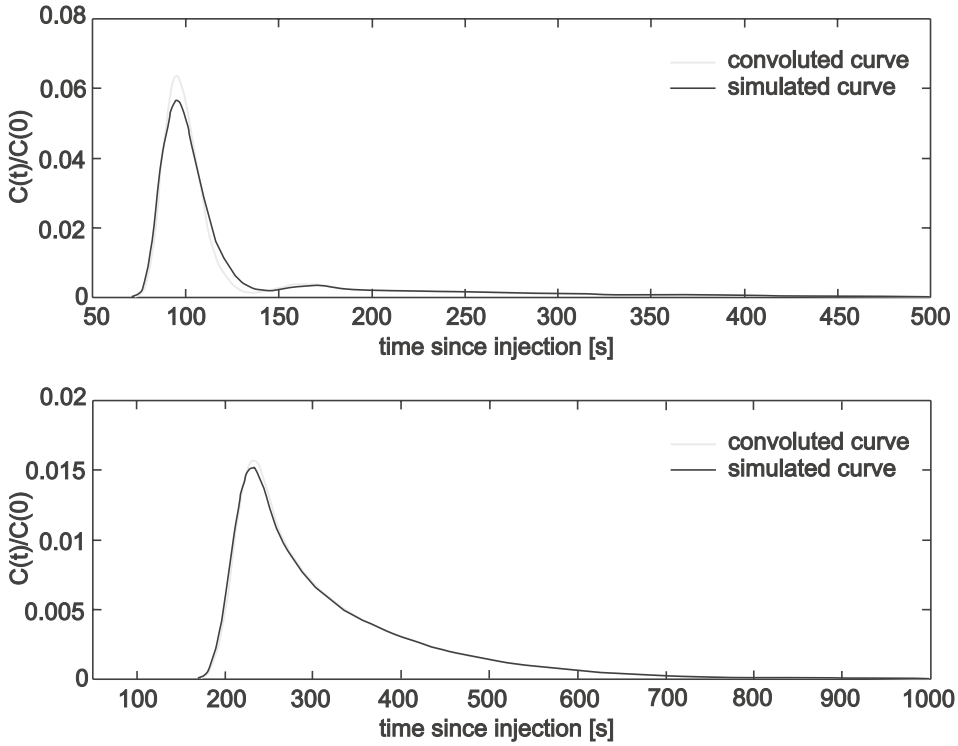

Fig. 7.2 Comparison of convoluted vs. simulated breakthrough curves after three subsequent pools. Although not completely identical, the convolution approach appears to be a good approximation of the deterministic model

7.1.3 Analysis of dispersion and retardation in sequences of structures

With the tools described above, some examples have been created. Fig. 7.3 shows the evolution of dispersion and tailing in some geometries up to 250 m long. A simple conduit with constant cross-section is the 'baseline' (a). The other cases are: b) a pool every 20 m, c) a rapid every 20 m, d) a sequence pool - rapid - pool. A pool BTC is represented by the 'pool with stones' BTC in these scenarios. Dispersion increases faster at the beginning and tends towards a linear increase with distance; the high increase at the beginning is due to the rectangular input signal. For the same reason, a considerable tailing is created at the beginning, which will reduce and transform into dispersion later. Each additional pool leads to a jump both in tailing and dispersion.

The first rapid strongly increases the dispersion of the plume, while the influence of the following will be smaller to fading. Tailing is increased by the first and second rapid while

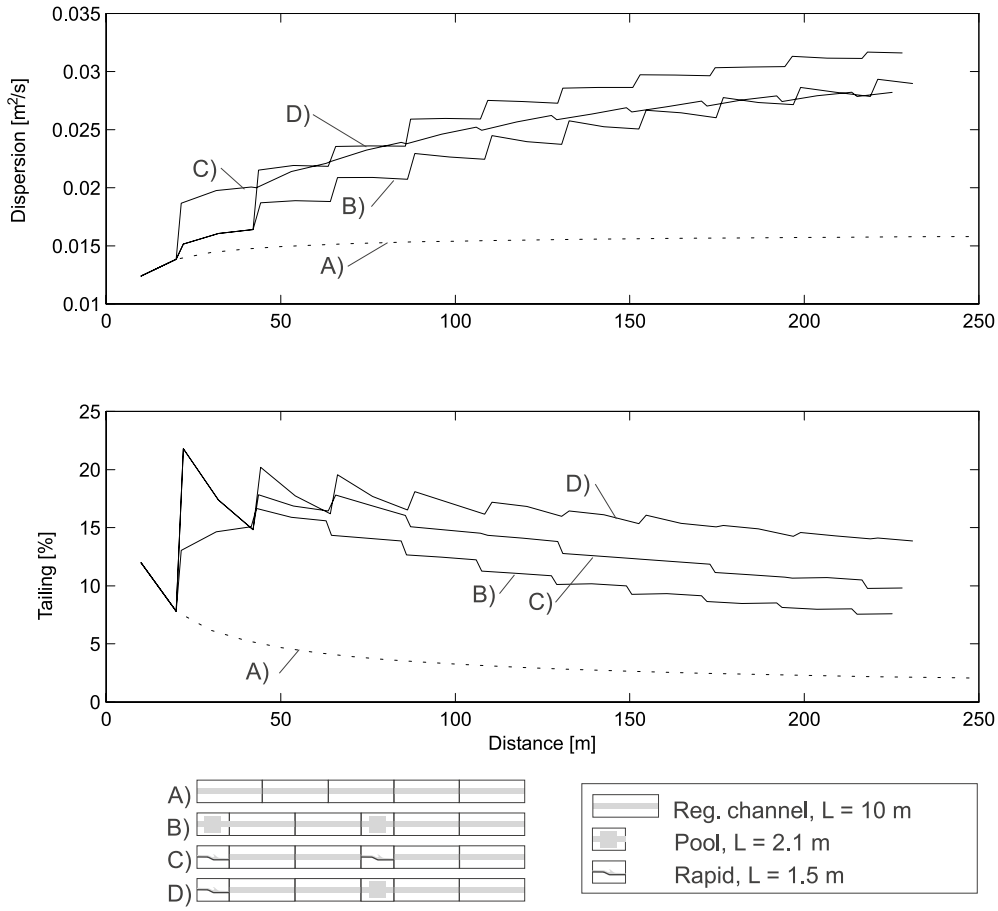

Fig. 7.3 Evolution of dispersion and tailing in some types of conduit
(all calculated with the convolution approach)

(A) Channel only
(B) Channel with a pool every 20 m
(C) Channel with a rapid every 20 m
(D) Channel with pools and rapids intermittently every 20 m

the following will reduce it. This may be explained by the high sensitivity of this special structure to the length of the input signal.

The mixed case lies both for the evolution of dispersion and tailing between the two others. When there are multiple structures, the dispersion will increase and not, like in the first case, converge to a constant value.

7.2 Particle size distribution scenarios

The approach for particle deposition is a little analog to the transfer function approach. The hypothesis from Chapter 5 for particle deposition is utilized on a local scale. Assume a fluid volume that is large compared to the volume of a local structure. The fluid volume shall contain an ensemble of particles satisfying the conditions from Chapter 5 (i.e. particles are sufficiently diluted and sufficiently small to be isotropic distributed by turbulent flow). Let N(d) be the particle size distribution of this ensemble, and S(d) the deposition probability from Chapter 5. For simplicity, assume that the fluid volume does not mix with other fluid volumes. Then, after passage of one flow form:

$$N_{out}(d) = S(d) \cdot N_{in}(d) \tag{7.3}$$

For convenience, N and S may be written as vectors where each element represents a size class. The passage of a 'PSD plume' in m subsequent structures may then be written as:

$$N_m = S_m \cdot S_{m-1} \cdot \ldots \cdot S_1 \cdot N_0 \tag{7.4}$$

7.2.1 Particle deposition in a conduit

Two examples have been calculated using equation and flow simulation data:

- Passage of a 'particle size distribution plume' in a channel (length 50 m)
- Passage of a 'particle size distribution plume' in a sequence of five pools

Fig. 7.4 shows the setup and the resulting particle size distributions. The initial distribution is assumed to be

$$N_0(d) \sim d^{-b} \tag{7.5}$$

with b = -2. While the constant β from equation 5.4 is not known, curves have been plotted for β = [0.001 .. 0.005]. It is assumed that the chemical attraction forces are at least as large as gravity.

Attachment of the particles depending on their size produces PSD curves similar to those found in the Noiraigue aquifer, i.e. there are two parts having different slopes. The slope of the 2nd part depends on the geometry, while the position of the breaking point depends on the value of β.

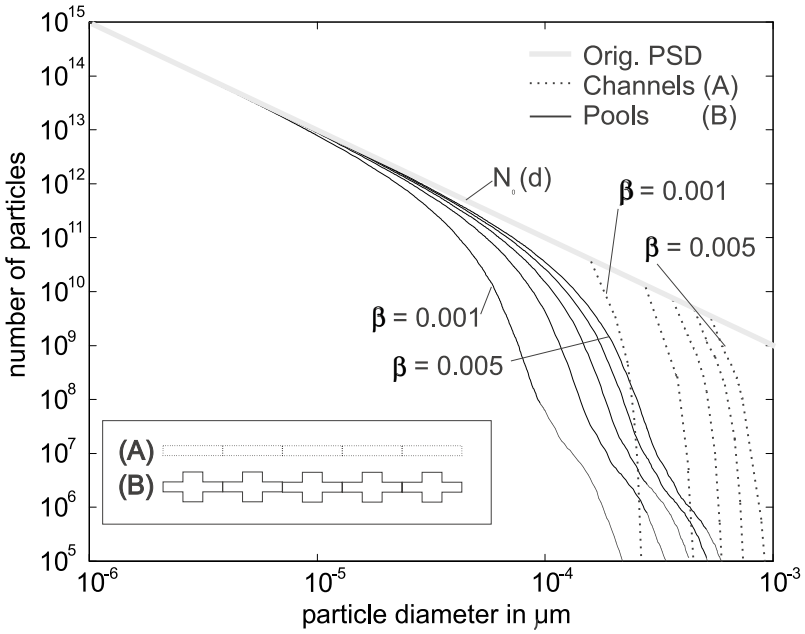

Fig. 7.4 Passage of an initial power-law particle size distribution in two different geometries

(A) Sequence of five channels
(B) Sequence of five pools

The parameter β characterizes the strength of the adhesive forces and is varied between 0.001 and 0.005

8 Applications

In this chapter the concepts of tracer transport and particle deposition are compared to field tests, i.e. tracer tests in the Milandre system and particle size distributions in the Noiraigue aquifer. This may lead towards future applications of these concepts.

8.1 Comparison of the numerical scenarios to field tracer tests: evolution of dispersion and tailing

From the numerous short distance tracer tests conducted in the catchment basin and in the conduit system of Milandre, some are analyzed with the fitting described in Chapter 4 and compared with the numerical results.

Local scale in field tests

The tests 'tracing A' and 'tracing B' have been injected directly into the underground river. Tracer substance in both tests was NaCl. These tests were chosen here because they pass, on a small scale, in quite interesting flow forms. Tracing A is sampled at two points, 85 m and 1208 m below the injection point. There is a detailed sketch of the first segment in Fig. 8.1. It is a channel with mainly tranquil flow and only a few small rapids. At 85 m, a dispersion of 0.03187 m^2/s and a tailing of 16% is found. At 1208 m the dispersion has increased to 0.46 m^2/s while the tailing is reduced to 10%. This corresponds qualitatively to the numerical scenario, which predicts increase of dispersion and decrease of tailing with increasing length. The overall much higher dispersion in these field tests is explained by:

1. The different flow regime (discharge was 13 l/s instead of 1 l/s in the numerical scenario).

2. A different channel width of 1 m or more, including more roughness elements, obstructions and inhomogeneities than the relatively smooth geometry in the numerical model.

A repetition of the latter with adapted cross section and discharge should provide a better comparison. However there is evidence that the influence of discharge and cross-section, parameters that can easily be changed in the numerical simulation, is larger than the influence of roughness and small obstructions.

Tracing B is sampled three times, at distances of 15 m, 35 m and 873 m from the injection. Between the first and second sampling point there is the 'Grande Cascade', a vertical drop of 4 m followed by a large pool. The tailing increases from 11.5% to 34.2% between the first two sampling points, while the dispersion is 0.0269 m^2/s and 0.0695 m^2/s, respectively. This means that D* (dispersion/length) changes from 0.00179 m/s to 0.00198 m/s. At 873 m, the tailing is at 17%, and the dispersion is 0.53 m^2/s.

Hence, tracer tests in this underground river show the same trends as the numerical scenario: with increasing length, there is a decrease of tailing, and an increase of dispersion of the BTC. The dispersion should increase more when there are large inhomogeneities. Unfortunately there are no field tracer tests on a completely homogeneous geometry, which could be compared with case (A), Fig. 7.3, available.

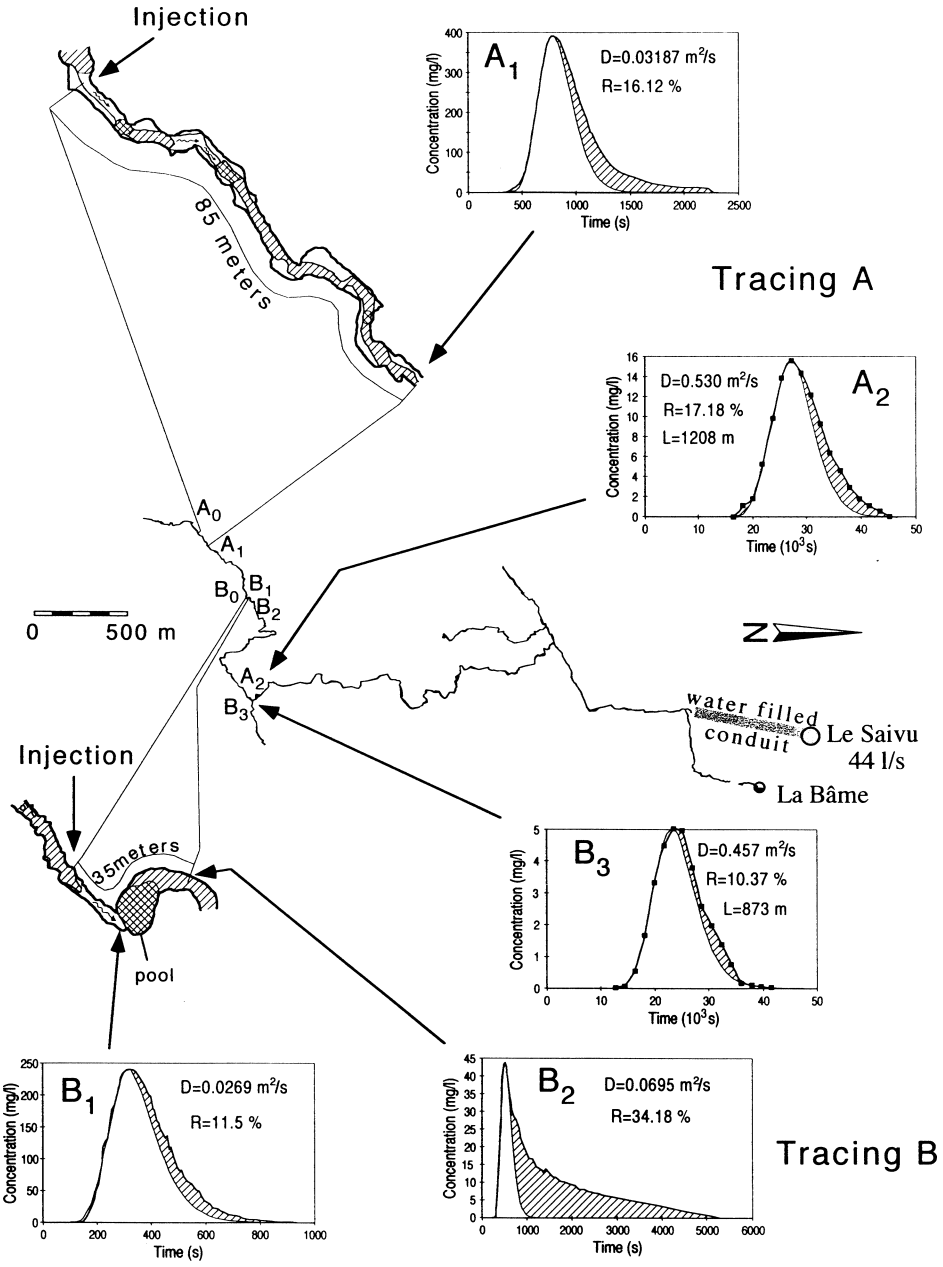

Fig. 8.1 Tracer experiments in Milandre (JEANNIN 1996)

Kilometric scale field tests vs. extrapolation of the numerical scenario

The dispersion of larger scale tracer tests, i.e. with injection in boreholes and sinkholes, and sampling along different points in the cave and at the exit, is summarized in Fig. 8.2 for tracings at low, intermediate and high discharge. The 'scale effect' hypothesis predicts an increase of dispersion with distance, due to inhomogeneities of different size and random distribution. However within the present data no trend can be seen whether this increase is less than linear, linear or more than linear.

The numerical scenario suggests that the increase with length is less than linear, but this may be due to multiple repetition of the same structures. Therefore, a linear increase has been assumed for extrapolation of the numerical scenario (length 250 m) to a kilometric scale. The field data show a strong dependence of the increase of dispersion on discharge, and the extrapolation of the numerical scenario fits well into this trend.

8.2 Deposition model and particle size distributions in karst water

Particle size distributions in nature are of exponential or Pareto type. For very small particle sizes the number of particles found increases tremendously. The same can be found for other classes of size-distributed objects in nature. The particles that are interesting for colloidal transport in natural environment are in the size range between 50 nm and 10 µm.

Particle size distributions in the Noiraigue aquifer have been measured from 1994 - 1998 and are reported by ATTEIA & KOZEL (1997). The size distribution curves showed two parts having different slopes. Variations of the first part (smaller particles) appeared to be correlated to changes in pH. The analysis of the second part in relation with discharge values suggested an effect of sedimentation and resuspension on these particles. Fig. 8.3 shows the observed particle size distributions.

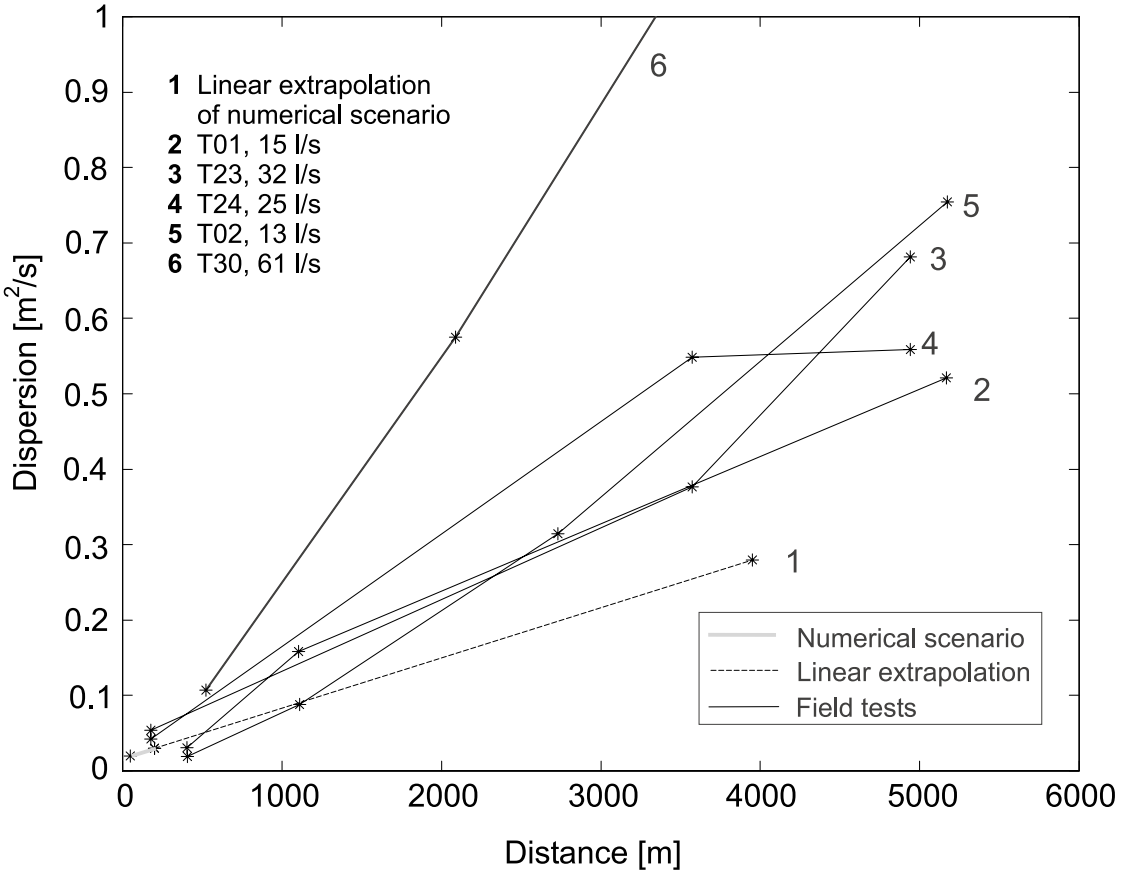

Fig. 8.2 Evolution of dispersion of BTC from several microtracings in Milandre

The result of the deposition scenario from Chapter 7 is qualitatively comparable: a breaking point appears at the onset of deposition, and this leads to two segments with different slopes.

However, it is not possible to calibrate the deposition model on this, because there are too many unknown parameters (geometry of the Noiraigue conduit system, value of β for different particles).

8.3 Future applications in Hydrogeology

While tracer experiments are on the way to become a quantitative tool in hydrogeology, more detailed knowledge about the processes determining the shape of the breakthrough curves becomes important. The numerical experiments show that, on a local scale, it is possible to conclude from the shape of a BTC on conduit geometry and flow regime. Unfortunately, this information gets lost with distance. Also, in field there are more factors that could not be taken care of in this study, i.e. influence of the passage in soil and epikarst, interaction with the matrix, adsorption and chemical alteration of tracer. However, more detailed knowledge of the processes in conduits means one step forward towards a comprehensive understanding of tracer tests.

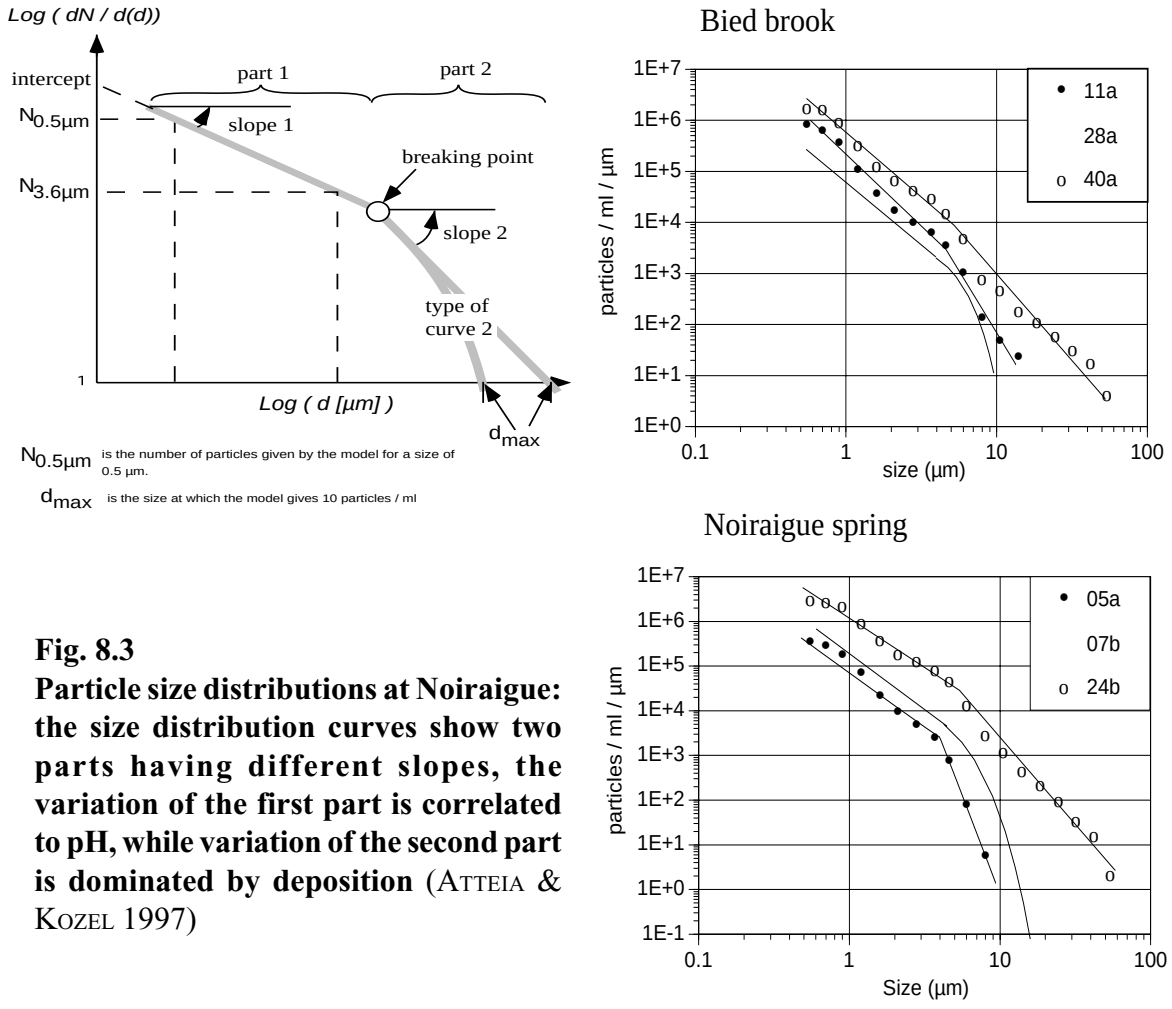

Fig. 8.3
Particle size distributions at Noiraigue: the size distribution curves show two parts having different slopes, the variation of the first part is correlated to pH, while variation of the second part is dominated by deposition (ATTEIA & KOZEL 1997)

9 Conclusion

Knowledge about structure and flow processes in karst aquifers should be as detailed as possible to optimize water resources protection and management (JEANNIN 1998).

An ideal general model of a karst aquifer might describe, on a grid resolution of decameters or even meters, all relevant physical processes, parameter and flow fields in the four sub-systems infiltration, epikarst, unsaturated zone and saturated zone (comp. Fig. 9.1). Variations of the system state in time (hydrograph) should also be taken into account. Meanwhile present knowledge is limited by four problems: definition of sub-systems, knowledge of physical processes, parameter measurements and abilities of the available numerical models (JEANNIN 1998).

The present thesis is focused on the conduit subsystem. The major physical process here is free-surface flow of the karst groundwater in conduits of decimeter to decameter dimensions. Associated with the karst water flow are transport processes of solute tracer and suspended particles.

9.1 Principal results of this thesis

A necessary condition to do numerical modeling of processes in karst water is the existence of an appropriate conceptual model. In this case a conceptual model of the conduit system was needed. While a typical problem of hydrologic parameter measurements in karst is large variability between grid points (e.g. piezometric levels), the geometry of a conduit system might, from a technical point of view, be measured to any desired precision. But this would lead to a result specific to an individual location while the objective was to find example-types of geometries. The second constraint for the conceptual model is the maximum size of the example-type geometries. It is defined by the limits of the engineering CFD program used for the calculations. The use of this model is necessary because common hydrological flow simulation software does not have the ability to calculate the physical processes - namely 2D and 3D turbulent transport - to the desired accuracy.

9.1.1 Transport of solute tracer through the conduit system

Numerical tracer experiments on a decameter scale show that it is possible to identify a geometry by its BTC. A relation could be established between the stagnant volume in a geometry and the percentage of tailing in the BTC. The shape of the tail may contain information about the distribution of the stagnant volume: intermediate eddies close to the through flow produce a ‘shoulder’ on the main peak, while long, small dead ends, like in a maze geometry, lead to a small but constant tailing during a long time.

The concatenation of transfer functions allows to overcome the limitations of the CFD program and to create scenarios that may be compared to conduit scale field tracer tests, e.g. in Milandre cave. These show reasonable agreement with the numerical results.

9.1.2 Transport and deposition of small particles in a karst aquifer

The results of the conduit flow model may also be used to predict deposition of suspended particles in a conduit system. A conceptual model for this process was developed, but only partly validated.

9.2 Benefits of this study to karst hydrology research

This thesis is a contribution to the deterministic approach in karst hydrogeology. With numerical simulations and laboratory experiments it could be shown that the conduit system may have storage capacities which play a role both in tracer experiment breakthrough curves and for the deposition of suspended particles. This is confirmed by laboratory experiments which however are not always in perfect agreement with the results of the numerical model.

Experimental hypotheses about the evolution of tailing and dispersion during the passage of solute tracer in a single karst conduit (JEANNIN & MARECHAL 1997) could be verified with this method.

The use of the tracer breakthrough curve fitting method developed in Chapter 4 may be of interest for many existing and future tracer tests. This method may be used independently of the numerical scenarios it was developed for. It may alo be useful on test sites which do not contain a conduit system. However, discharge should remain approximately constant during the tracer passage.

The particle deposition model is still in a construction state, but it may be a base for more sophisticated deposition models.

9.3 Perspectives of future research

- A coupling of the conduit model to larger scale double porosity models may be of interest to improve understanding of the hydraulics of karst aquifers with changing hydrograph conditions. This coupling doesn't have to be explicit but may be in the sense of result lumping. Prior to this it may be interesting to work with the same conceptual model on a more flexible CFD environment. This might allow to simulate flooding of a conduit system as described by JEANNIN & WILDBERGER (1995) for the Hölloch cave system.

- The example-type breakthrough curves for the conduit system may be extended by typical breakthrough curves for the other subsystems (infiltration, epikarst) and compared to the transfer functions for a whole aquifer as described by DOERFLIGER (1996).

- Much interesting work remains to do on the deposition model for suspended particles. The actual test site at Noiraigue spring has always a large population of chemically interesting particles, but unfortunately hydraulic parameters cannot be mesured with sufficient accuracy at this site.

A test site where deposition rates may be measured at known flow conditions might reveal new results. Such a test site may also be found in a surface river bed.

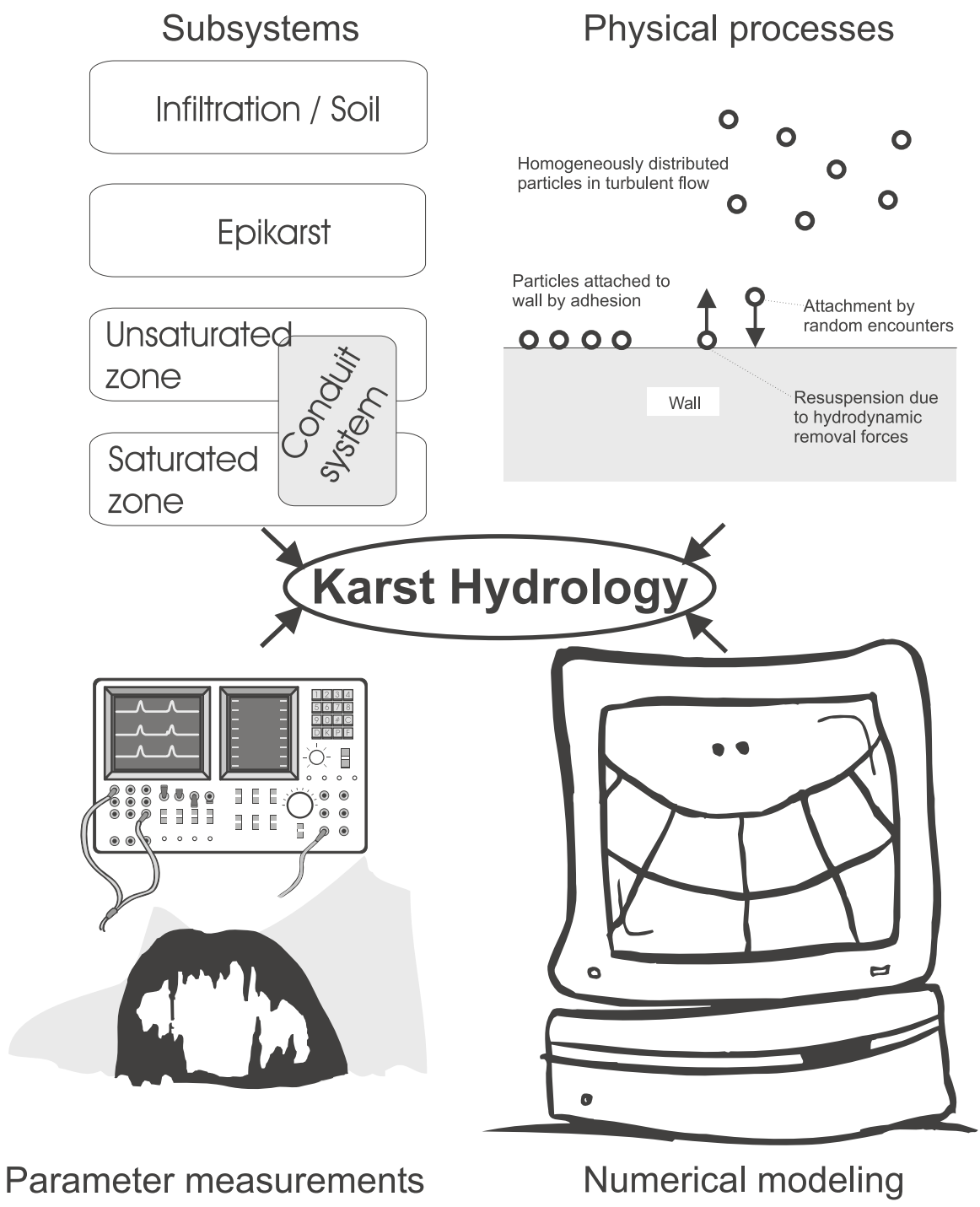

Fig. 9.1 **Definition of subsystems, conceptual models of underlying physical processes, field parameter measurements and appropriate numerical modeling methods are needed to describe Karst Hydrology**

Notation

A*	scaled deposition area	-
B	channel width	m
β	coupling constant between τ_0 and d	$m^{7/3}s^2/kg$
C	tracer concentration	$1/m^3$
C_μ	turbulence closure constant	-
C_E	encounter probability	-
C_W	weir constant	$m^{1/2}/s$
D, D_t	(turbulent) dispersion coefficient	m^2/s
D*	dispersion scaled by length	m/s
d	particle diameter	m
ε	dispersion rate of turbulent kinetic energy	m^2/s^2
F_B	body force on a fluid in the Navier-Stokes Equation	N/m^3
F, I, O	transfer function, input and output signal	-
g	gravity acceleration	m/s^2
H	water height over weir crest	m
i, j, k	grid cell indices	-
K	turbulent kinetic energy	m^2/s^2
L	distance between injection and sampling point	m
l	characteristic length	m
M	injected tracer mass	kg
N	particle size distribution	-
P	deposition probability	-
p	pressure	N/m^2
Ψ	scalar species mass fraction	$1/m^3$
Q	discharge	m^3/s
R	tailing	%
ρ, ρ_A	water (air) density	kg/m^3
ρ_p	particle density	$1/m^3$
S	deposition probability of PSD	-
s	speed	m/s
T_k	Kolmogorov time scale	s

T_p	particle response time in turbulent flow	s
t	time	s
τ_0	wall shear stress	N/m^2
U	characteristic velocity	m/s
$\underline{u}$	flow velocity vector	m/s
u_{in}	inflow velocity	m/s
u	peak velocity of BTC	m/s
x, y, z	cartesian coordinate system	m
	convention: x is distance in flow direction	
Ξ	any hydrodynamic scalar or vector field	-

References

Allen, J. R. L. (1995): The origin of cave flutes and scallops by enlargement of inhomogeneities. Rassegna speleologica Italiana, 14/1, 3-20.

Atkinson, T. C. (1977): Diffuse Flow and Conduit Flow in Limestone Terrain in the Mendip Hills, Somerset (UK). J. Hydrol. 70, 309-327.

Atteia, O. (1999): Evolution of size distributions of natural particles during aggregation: modelling vs. field results. Colloids and Surfaces A.

Atteia, O. & Kozel, R. (1997): Particle size distributions in waters from a karstic aquifer: from particles to colloids. Journal of Hydrology 201, 102-119.

Beyer-Portner, N. A. et al. (1998): Erosion and sedimentation in mountainous environment - physical and numerical modelling. Proceedings of the International Conference on Hydrology and Water Resources of Humid Tropics'98, Panhor Island, Perak, Malaysia, 24-26 November 1998.

Bhattacharya, S. & Mittal, K. L. (1978): Mechanics of removing glass particles from a solid surface. Surface Techn. 7, 413-425.

Blumberg, P. N. & Curl, R. L. (1974): Experimental and theoretical studies of dissolution roughness. J. Fluid Mech. 65, 735-751.

Bogardi, J. (1974): Sediment transport in alluvial streams. Akademiaai Kiado, Budapest.

Bonacci, O. (1987): Karst Hydrology. Springer. Heidelberg, New York, Berlin.

Bonnet, P. (1976): Hydrodynamique et pollution en estuaire. PhD Thesis, Université de Paris.

Braaten, D. A. (1988): Particle resuspension and associated coherent structures in a turbulent boundary layer. Draft, UC Davis, CA, USA.

Brockmann, J. E. (1984): Range of possible resuspension and reentrainment of fission products during contaminant depressurization. Draft, Sandia National Lab. 84-0410.

CFDS (1996): CFX 4.1 Flow Solver User Guide Computational Fluid Dynamics Services. Harwell, Oxfordshire, UK.

Cleaver, J. W. & Yates, B. (1973): Mechanism of detachment of colloidal particles from a flat substrate in turbulent flow. J. Coll. Interf. Sci. 44, 464-474.

Corn, M. (1966): Adhesion of particles in aerosol science. Academic Press, London.

Curl, R. L. (1974): Deducing flow velocity in cave conduits from scallops. Nat. Speleol. Soc. Bull. 36, 1-5.

Curl, R. L. (1986): Fractal dimensions and geometries of caves. Mathematical Geol. 18, 765-783.

Daugherty, R. L., Franzini, J. B. & Finnemore, E. J. (1985): Fluid mechanics with engineering applications. McGraw-Hill, New York, 8th ed.

Demuren, A. O. & Rodi, W. (1986): Calculation of flow and pollutant dispersion in meandering channels. J. Fluid. Mech., 172(1).

Derjaguin, B. V. & Landau, L. (1941): Acta Physicochim. URSS, 14, 633.

Doerfliger, N. (1996): Advances in karst groundwater protection strategy using artificial tracer tests analysis and multiattribute vulnerability mapping (EPIK method). PhD Thesis Université de Neuchâtel, Switzerland.

Dreybrodt, W. (1988): Physical Processes in Karst Systems. Springer. Heidelberg, New York, Berlin.

Fromentin, A. (1989): Particle resuspension from a multi-layer deposit by turbulent flow. Paul Scherrer Institut, Würenlingen, Switzerland.

Fuchs, N. A. (1964): The Mechanics of Aerosol. Pergamon Press, Oxford, UK.

Gale, S. J. (1981): The paleohydraulics of karst drainage systems: fluvial cave-sediment studies. Proc. Int. Congr. Speleol., 8: 213-216.

Gale, S. J. (1984): The hydraulics of conduit flow in carbonate aquifers. Journal of Hydrol. 35, 93-110.

Garde, R. J. (1985): Mechanics of sediment transportation and alluvial stream problems. Akademiaai Kiado, Budapest.

Gessler, J. (1965): Der Geschiebebetriebbeginn bei Mischungen untersucht an natürlichen Abflästerungserscheinungen in Kanälen. Mitteil. VAW 69, ETH Zürich.

Goodchild, M. F. & Ford, D. C. (1971): Analysis of scallop patterns by simulation under controlled conditions. Jour. Geology 79, 52-62.

Graf, W. H (1971): Hydraulics of sediment transport. Water Resources Publications.

Gutterman, B. (1959): Dust properties in relation to dust collection. Pennsylvania State University, PA, USA.

Gvozdetskii, N. A. (1967): Occurence of karst phenomena on the globe and problems of their typology. Earth Res. 7, 98-127.

Hauns, M. & Jeannin, P.-Y. (2001): Dispersion, retardation and scale effect in tracer breakthrough curves in karst conduits. J. of Hydrology 241 (2001) 177-193.

Hauns, M., Atteia, O. & Hermann, F. (1997): Application of a computational fluid dynamics model to cave river hydrodynamics. Proc. of the 12th Intern. Congress of Speleology, La Chaux-de-Fonds, Switzerland, Vol. 2, 141-145.

Hermann F. (1990): Experimente zur Dynamik von Staublawinen in der Auslaufzone. PhD Thesis ETH Zürich.

Hermann, F. et al. (1996): Die Strömung an ausgewählten LHG-Pegeln bei extremen Hochwassern, untersucht mit numerischen 2- und 3-dimensionalen Modellen. Hydrologische Mitteilungen 24, 141-151.

Hermann, F. (1996): Numerische Simulation des VAW-Nachklärbeckens in der ARA Werdhölzli. Verband Schweizer Abwasser- und Gewässerfachleute, 511, 37-47.

Hobbel, E. F. (1988): Cohesion and interparticle forces. Delft Technical University.

Honerkamp, J. & Römer, H. (1986): Einführung in die theoretische Physik. Springer. Heidelberg, New York, Berlin.

Hubbe, M. A. (1984): Theory of detachment of colloidal particles from flat surfaces exposed to flow. Colloids and Surfaces, 12, 151-178.

Hubbe, M. A. (1987): Colloids Surfaces 25, 311.

Jeannin, P.-Y. (1996): Structure et comportement hydraulique des aquiferes karstiques. PhD Thesis, Université de Neuchâtel.

Kinzelbach, W. (1992): Numerische Methoden zur Modellierung des Transports von Schadstoffen im Grundwasser. R. Oldenbourg-Verlag. München, Wien.

Kiraly, L. (1979): Remarques sur la simulation des failles et du réseau karstique par éléments finis dans les modèles d'écoulement. Bulletin du Centre d'Hydrogéologie No 3, 155-168.

Kiraly, L. (1988): Large scale 3-D groundwater flow modelling in highly heterogeneous geologic medium. In: Groundwater Flow and Quality Modelling, 761-775. Reidel Publishing Company.

Kobus, H. (1989): Hydraulic Modelling. Verlag Paul Parey. Hamburg, Berlin.

Krupp, H. & Sperling, G. (1965): Z. Angew. Phys. 19, 259.

Krupp, H., Walter, G., Kling, W. & Lange, H. (1968): J. Colloid Interface Sci., 28, 170.

Larsen, R. I. (1958): Amer. Ind. Hyg. Ass. J. 19.

Lastenet, R. & Mudry, J. (1995): Impact d'un événement pluvieux exceptionnel sur le fonctionnement d'un système karstique. Géosciences de surface (Hydrologie + Hydrogéologie), C.R. Acad. Sci. Paris, t. 320, Série IIa, 953-959.

Leismann, H. M. (1987): Berechnung von Ausbreitungsvorgängen im Grundwasser mit der Methode der finiten Elemente. Universität Fridericiana zu Karlsruhe.

Mangin, A. (1976): Contribution à l'étude hydrodynamique des aquifères karstiques. PhD Thesis, Université de Dijon.

Maréchal, J. C. (1994): Etude et modélisation de l'hydraulique et du transport dans les drains karstiques. Masters thesis, CHYN, Université de Neuchâtel.

Maxey, M. R., Patel, B. K., Chang, E. J. & Wang, L.-P. (1997): Simulations of dispersed turbulent multiphase flow. Fluid Dyn. Res. 20, 143-156.

McCarthy, J. & Zachara, J. M. (1989): Subsurface transport of contaminants. Environ. Sci. Technol. 23.

Meiman, J. (1991): The effects of recharge basin land-use practices on water quality at Mammoth Cave National Park, Kentucky. Conference on National Ground Water Assoc. practices on Hydrogeology, Ecology, Monitoring and Management of Ground Water in Karst Terranes. Nashville, TN. Proceedings of the Third Conference National Park, Kentucky, 697-713.

Meselhe, E. A., Sotiropoulos, F. & Patel, V. C. (1995): Three-dimensional numerical model for open channels. Proc. Int. Conf. on Hydropower, Hydropower 1995, ASCE, 2100-2120.

Mohammadi, B. & Pironneau, O. (1993): Analysis of the K-Epsilon Turbulence Model. Wiley, Chichester, UK.

Morlok, U. (1996): Parameter-Identifikation in Doppel-Kontinuum-Modellen am Beispiel von Karstaquiferen. PhD Thesis, Tüb. Geowiss. Arbeiten, Universität Tübingen.

Nino, Y. & Garcia, M. H. (1996): Experiments on particle-turbulence interactions in the near-wall region of an open-channel flow: implications for sediment transport. J. of Fluid Mech. 326, 285-320.

Palmer, A. N. (1975): The origin of maze caves. The NSS Bulletin, (37)3, 56-76.

Palmer, A. N. (1991): Origin and morphology of limestone caves. Geological Society of America Bulletin, 103, 1-21.

Phillips, M. (1980): A force balance model for particle entrainment into a fluid stream. J. Phys. D. 13, 221-233.

Rastogi, A. & Rodi, W. (1978): Predictions of heat and mass transfer in open channels. J. Hydr. Engrg., ASCE, 104 (3).

Raudkivi, A. J. (1982): Grundlagen des Sedimenttransports. Springer. Heidelberg, New York, Berlin.

Raudkivi, A. J. (1993): Sedimentation: exclusion and removal of sediment from diverted water. A. A. Balkema, Rotterdam.

Raudkivi, A. J. (1990): Loose Boundary Hydraulics. Pergamon Press, Oxford.

Rodi, W. (1993): Turbulence models and their application in hydraulics: a state-of-the art review. A. A. Balkema, Rotterdam.

Rossier, Y. & Kiraly, L. (1992): Effet de la dilution sur la détermination expérimentale des dispersivités dans les aquifères karstiques. Bulletin du Centre d'Hydrogéologie No 11, 1-16.

Ryan, J. N. & Elimelech, M. (1996): Colloid mobilization and transport in groundwater. Colloids and surfaces A, 107, 1-56.

Sanglard, H. (1999): http://www-iiia.unine.ch/ZoomIn/.

Sauter, M. (1992): Quantification and forecasting of groundwater flow and transport in a karst aquifer. PhD Thesis, Tüb. Geowiss. Arbeiten, Universität Tübingen.

Schnegg, P. & Doerfliger, N. (1997): An inexpansive flow-through field fluorimeter. Proceeedings of the 12th International Congress of Speleology, La Chaux-de-Fonds, Switzerland.

Simon, A. L. (1992): Practical Hydraulics. Wiley. New York.

Simons, D. B. & Sentuerk, F. (1982): Sediment transport technology. Water resources publications. Fort Collins, Colorado.

Sinha, S. K., Sotiropoulos, F. & Odgaard, A. J. (1998): Three-dimensional numerical model for flow through natural rivers. J. of Hydraulic Engineering, 13-27.

Slabe, T. (1995): Cave rocky relief and its speleological significance. Ljubljana, Znanstvenoraziskovalni center SAZU (Zbirka ZRC; 10).

Smith, C. D. & Yu, J. N. G. (1966): Use of baffles in open channel expansions. J. of the Hydraulics Division, ASCE, March 1966.

Taylor, G. I. (1954): The dispersion of matter in turbulent flow through a pipe. Proc. R. Soc. London 233A, 446-468.

Teutsch, G. (1988): Grundwassermodelle im Karst: praktische Ansätze am Beispiel zweier Einzugsgebiete im tiefen und seichten Malmkarst der Schwäbischen Alb. PhD Thesis, Tüb. Geowiss. Arbeiten, Universität Tübingen.

Verwey, E. J. W. & Overbeek, J. Th. G. (1948): Theory of the stability of lyophobic colloids. Elsevier, Amsterdam.

Vischer, D. & Huber, A. (1984): Wasserbau. Springer. Berlin, Heidelberg, New York.

Visser, J. (1976): Surface and Colloid Science. Wiley, New York.

White, W. B. (1988): Geomorphology and hydrology of karst terrains. Oxford University Press.

White, W. B. & Deike, G. H. (1976): Hydraulic geometry of solution conduits. Proc. 1976 Nat. Speleol. Soc. Convention, 57-60.

White, W. B. & Deike, G. H. (1989): Hydraulic geometry of cave passages. In: Karst Hydrology – Concepts from the Mammoth Cave Area, 223-258. Van Nostrand Reinhold, New York.

White, W. B. & White, E. L. (1970): Channel hydraulics of free surface streams in caves. Caves and Karst 12, 41-48.

White, W. B. & White, E. L. (1989): Fracture controls on conduit development. In: Karst Hydrology – Concepts from the Mammoth Cave Area, 259-293. Van Nostrand Reinhold, New York.

Yalin, M. S. (1972): Mechanics of sediment transport. Pergamon Press. Oxford, UK.

Zimon, A. D. (1982): Adhesion of dust and powder. Consultants Bureau, New York.

Zwahlen, F. & Doerfliger, N. (1994): Interprétation des essais de traçage en milieu karstique, modèle de type boîte noire. Nouvelles du Service hydrologique et géologique national, 94/1, 37-38.

Acknowledgements

Many persons contributed in different ways to realization and succes of the present work.

First of all I would like to thank my advisors Prof. Francois Zwahlen and Prof. Olivier Atteia who guided and supervised my thesis work at CHYN. They provided an encouraging academic environment with all possible freedom, and they were was always ready for enthousiastic discussions.

Dr. Felix Hermann at the VAW, ETH Zürich, gave me initial help how to install LINUX, an introduction into the use of CFX-FLOW3D, showed me how to apply it to modelize a natural aquatic environment, and was later my personal 'hotline' always ready to answer many, many questions on the phone.

Dr. Pierre-Yves Jeannin, Francois Burret and Jean-Christophe Marechal provided cave topography and microtracing data. Thanks also all the members of the Speleo Club Jura who dug the tunnels and pits that make scientific work at Milandre possible.

Herve Sanglard from the Institute of Informatics not only provided the versatile visualization platform ZoomIn, but also lots of help as administrator of the workstations I was using.

At the beginning of the project, Dr. Eduard Zuur was there for many discussions on numerical modeling of natural flows.

Prof. Pierre Perrochet accepted to be a member of the Jury and found the time for helpful discussions on the numerical modeling aspects.

Dr. Pierre Schnegg offered access to his fluorometers, including special program modifications and hotline.

I also wish to thank Prof. W. B. White and his wife Dr. E. White. Several chapters of this thesis were written during my visit at Penn State University in Winter 1999. Also, Prof. White accepted to be a member of the Jury.

The editors Prof. Ch. Leibundgut and Prof. S. Demuth kindly accepted the manuscript for publication.

All the staff of the Institute of Geology and the Hydrogeology Center at Neuchatel provided a good working athmosphere and lots of fun during three years: Prof. Martin Burkhard, Prof. Bernard Kübler, Prof. L. Kiraly, Prof. I. Müller, Dr. F.-D. Vuataz, Dr. R. Kozel, E. Kuster, Michele Jaquet, Cyril, Caspar, Darko, Frank, Marc, Ray, Vincent and everybody else.

Thanks to Myriam for lots of patience during the redaction of the manuscript.

I am indebted to my family and all my friends who supported me during my time in Switzerland.

The project was financed by the Swiss National Foundation for Scientific Research.